Analysis of Hydrodynamic Instabilities and Combustion Dynamics in Turbulent Reacting Flows

by

Yee Chee See

A dissertation submitted in partial fulfillment
of the requirements for the degree of
Doctor of Philosophy
(Aerospace Engineering)
in the University of Michigan
2014

Doctoral Committee:

Assistant Professor Matthias Ihme, Stanford University, Co-Chair
Professor James F. Driscoll, Co-Chair
Professor Luis P. Bernal
Professor David R. Dowling
Lennart S. Hultgren, NASA GRC

2014

Acknowledgments

Professor Ihme, my Ph.D. advisor, has been instrumental in helping me to complete this dissertation. So, I wish to take this opportunity to extend my utmost gratitude for his unending research and technical guidances. Despite my flaws, he has stayed with me throughout my doctoral studies and tolerated my sloppiness. I am sure that there are countless spelling mistakes and grammatical errors in this acknowledgements piece, which is not edited by him. Yes, I have at least used Ispell here.

I also would like to thank Professor Driscoll, Professor Bernal, Professor Dowling, and Dr. Hultgren for taking time out of their busy schedule to serve on my dissertation committee. Since my advisor has moved to Stanford, Professor Driscoll has been filling in for him in matters relating to paperwork for my graduation process. Also, I am especially grateful for Dr. Hultgren who made two long drives from NASA GRC to University of Michigan, and one of which was done in snowy road conditions.

The comradeship in FXB room 2211 has been invaluable to me and may be the sole source of social interactions that I had when I was knee-deep in my post-graduate studies. Therefore, I wish to express my thanks not only to current residents of room 2211 but also to former officemates who have moved on. The usual lunch time discussions with Brad and Kentaro have been intellectually stimulating, and my knowledge on numerical schemes and plasma physics has increased as a result. In addition, I am very thankful of the thesis editing work done by Wai Lee and Brandon. Despite originating from a rival country, Wai Lee has offered me tremendous help in getting around Ann Arbor. Also Yun Tao, thank you for constantly reminding that I need to buckle up and finish the tasks at hand. The constant bantering with Yu may not be intellectually useful but I am grateful for the fun times.

The discussions with students of Professor Driscoll have also been fruitful and thought provoking. Specifically, Dr. Allison and Dr. Temme have provided useful information

regarding the properties of different measurement technique. It gives me a whole new appreciation of experimental data and the steps needed to obtain accurate measurements.

Finally, I wish to exercise filial piety by thanking my parents for all the hardship that they have endured in raising me. Words are not sufficient to describe how much they sacrificed for me. When times are tough, they are always there to provide me with words of encouragement. I am very thankful for their moral supports which help me to soldier on.

TABLE OF CONTENTS

LIST OF FIGURES

LIST OF TABLES

LIST OF SYMBOLS

α	wavenumber
$\boldsymbol{g}$	body force vector
$\boldsymbol{q}$	heat flux vector
$\boldsymbol{u}$	velocity vector
$\boldsymbol{V}$	species diffusion velocity vector
$\boldsymbol{V}_c$	correction velocity
χ	scalar dissipation rate
Δ	filter width
$\mathcal{D}$	binary diffusion matrix
$\dot{\omega}$	source term
$\dot{m}$	mass flow rate
$\dot{Q}$	heat source
$\underline{\underline{\tau}}$	viscous stress tensor
$\underline{\underline{S}}$	rate-of-strain tensor
Γ	gamma function
Λ	reaction progress parameter
μ	dynamic viscosity
μ_b	bulk viscosity
ν	kinematic viscosity
ω	angular frequency
ϕ	generic variable

ψ	generic variable
ρ	density
τ	time scale
υ	heat diffusivity
A	area
C	progress variable
C_p	constant pressure heat capacity
D	characteristic diameter
E	total energy
G	Green function, LES filter kernel
H	total enthalpy
p	pressure
r	radial position
R_u	universal gas constant
t	time
U	characteristic velocity
W	atomic weight
X	mole fraction
Y	mass fraction

CHAPTER 1

Introduction

1.1 Motivation

In the foreseeable future, fossil fuel is likely to remain the dominant source of energy. This can be seen in the reference case of the world energy consumption forecast by the United State Energy Information Administration (EIA, 2013). The consumption of world energy from 1980 to 2010 and the subsequent projection up to 2040, sorted by sources, are shown in Fig. 1.1. This general projection of energy consumption is an extrapolation of the current economic outlook, energy consumption and policies. However, possible new legislation that may change the energy usage is not accounted for in this forecast. As one of the main energy sources, natural gas, is of particular interest to the energy security of the United States owning to its role in achieving foreign energy independence. Specifically, the recent increase in U.S. domestic shale gas production through the fast adoption of hydraulic fracking technique has reduced the net U.S. import of natural gas (EIA, 2013).

In a forecast by the International Energy Agency (IEA, 2012), a comprehensive outlook for the world energy consumption has been considered under the impact of several different sets of possible new energy policies. Some policies that are anticipated in this report, such as carbon tax, are new efforts to reduce the carbon emission. Despite that, fossil fuel is predicted to see no dramatic drop in its usage, and it is anticipated to account for 75% of the total energy consumption in 2035, a slight decrease from current share of 81%. In fact,

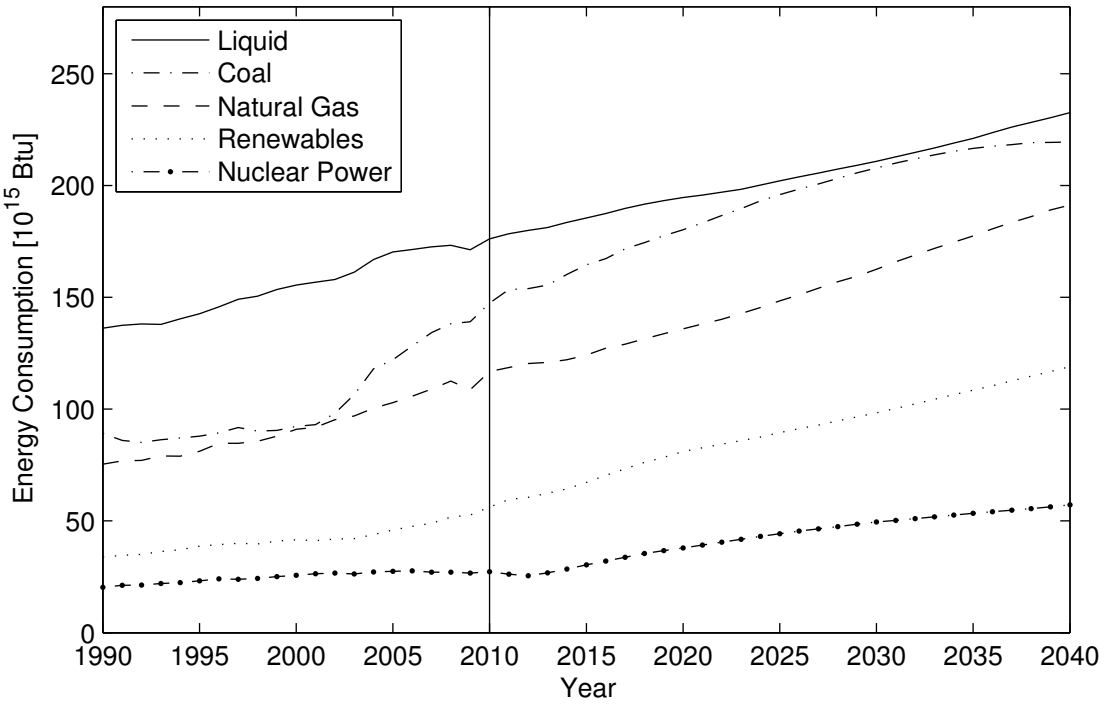

Figure 1.1: World energy consumption (in 10^{15} Btu) from 1990 to 2040 organized by energy source. The vertical line at 2010 separates historical values from forecast. (EIA, 2013)

the forecasted abatement of carbon emissions in this scenario is mostly due to the higher efficiency in the fossil energy utilization.

It is apparent that higher energy efficiencies are important in maintaining the future energy balance. Even now, increasing fuel prices have significantly boosted the demand for more efficient aircraft (Boeing, 2013). The aviation industry is especially sensitive to fuel price fluctuations since the cost of fuel is usually the main operating expenditure of most airline companies (Epstein, 2012). In the development of more fuel-efficient aircraft, the aircraft engine has been identified as an important component for improvement. The gas turbine engine, which is the power-plant of most commercial aircraft, is responsible for the conversion of the chemical-bond energy into propulsive force. If this conversion process can be made more efficient, it holds the potential to contribute to the overall efficiency of the next generation of aircraft.

The combustor is the engine component where the chemical energy of aviation fuel is liberated. Due to space constraints, fuel has to be mixed and burnt rapidly in the combustion chamber (Lefebvre *et al.*, 2010). To this end, modern combustors usually use swirling flows to enhance the mixing of fuel and air, as well as for flame stabilization (Gupta *et al.*, 1984). A swirling flow introduces strong shear, which can enhance the turbulence level in the combustor, thus improving the mixing of fuel and air. More importantly, high degree of swirl can induce recirculation zones, which are crucial for flame stabilization.

Besides more rapid combustion, reduced pollutant emission is another driving factor in combustor design. Over the years, the regulation on the emissions of oxides of nitrogen (NOx) for gas turbines have become increasingly stringent because NOx is known to be responsible for the formation of smog and acid rain (Upham *et al.*, 2012; Lefebvre *et al.*, 2010). In gas turbine combustors, lean premixed prevaporized (LPP) injection systems are promising technologies that can potentially achieve NOx reduction (Correa, 1993) . In addition, the rich-burn, quick-quench and lean-burn approach (RQL) is another NOx mitigation strategy applicable to aircraft engines (Lefebvre *et al.*, 2010).

Among the two NOx reduction technologies described above, the LPP technology is scheduled to be utilized in the next generation of combustors in aerospace applications (Foust *et al.*, 2012). The new design, so-called twin annular premixing swirler (TAPS) combustor, imparts significant amount of swirl to the flow in order to premix the fuel and air. Moreover, the twin annular design of the combustor features an inner non-premixed flame, which serves as the pilot to stabilize the outer lean premixed flame. A fully lean premixed combustor for aviation purposes may require further developments of this technology due to its susceptibility to thermo-acoustics instabilities (Lieuwen & McManus, 2003). Thermo-acoustic instabilities occur when energy liberated from heat release is converted to acoustic oscillations at resonance frequencies of the combustion device. These thermo-acoustic instabilities are usually of substantial amplitude, which can have a detrimental effect on the structural integrity of gas turbine engines.

In addition to thermo-acoustics instabilities, the combustion process itself can also be highly unstable. Specifically, local extinction of turbulent flames can occur when turbulent eddies are able to penetrate the reaction zone (Boxx *et al.*, 2013; Sutton & Driscoll, 2007; Ihme *et al.*, 2005). Subsequently, the extinguished flame may re-ignite later when the local condition becomes favorable to combustion again. Furthermore, flames can be blown out if the combustion process is overwhelmed by convection effect (Driscoll & Rasmussen, 2005). Nevertheless, the blow-off limit is generally avoided during the operation of engines but local extinction and re-ignition can still occur due to turbulence fluctuations.

Hydrodynamic instability is another type of unsteady dynamics that is commonly found in gas turbine combustors. In non-premixed combustion, the injection of fuel can introduce shear layers, which can support Kelvin Helmholtz instabilities (Coats, 1996). This type of hydrodynamic instability usually manifests as periodic roll-up of the shear layer, thereby inducing unsteady flame oscillations. In addition, large-scale helical instabilities can also be observed in swirling flames (Syred, 2006). These helical structures rotate, resulting in an asymmetric heat release mode. Due to the potential of these two types of hydrodynamic

instabilities in modulating the flame dynamics, the coupling with the thermo-acoustic mode of the combustor is a possibility.

Unsteady dynamics in a gas turbine combustors are not only observed in experiments, but they can also be captured in numerical simulations (Selle *et al.*, 2004). Numerical simulations are considered to be predictive methods as they allow for the characterization of a combustor without physically testing the actual device. In order to accurately model these unsteady effects within a combustor, high fidelity predictive methods are necessary (Gicquel *et al.*, 2012). However, the application of this class of predictive tools usually requires significant amount of computational resources. Although the advancement of computational capabilities has rendered high fidelity simulations more accessible, these methods are still not suitable for real-time assessments of engine designs in routine applications. For this reason, reduced-order models are the appropriate approaches. In contrast to detailed simulations, low-order models can quickly be evaluated but these models are mostly tailored to only capture a subset of the physics of a combustor. Nevertheless, both high fidelity combustor simulations and low-order models are useful predictive tools.

1.2 Large Eddy Simulation

Large Eddy Simulation (LES) is a high-fidelity numerical method that can be utilized for the prediction of combustion processes in gas turbine engines. This numerical procedure only resolves large scale turbulent structures while modeling the smaller scales. This is in contrast to the Reynolds Averaged Navier-Stokes (RANS) simulation in which all turbulent scales are modeled (Pitsch, 2006; Poinsot & Veynante, 2005). As a result, RANS simulations may be more sensitive to the choice of turbulent models than LES. However, LES is computationally more expensive than RANS due to increased resolution requirements.

Gicquel *et al.* (2012) recently reviewed the development of LES for modeling real combustors. In this review article, the swirler has been identified as a suitable target for LES

simulations. Due to the complex flow passages in most swirlers, it may produce highly complex flow field structure in the combustor even without reaction. With this issue in mind, Wang *et al.* (2007) have performed LES to study the non-reacting flow in complex swirlers. In this study, the LES results are validated against statistics of the experimentally measured velocities at selected downstream locations. Given sufficient mesh resolution, the aforementioned simulation results generally show reasonable agreement with experiments.

Unlike non-reacting simulations, LES of reacting flows requires additional closure models for the turbulence chemistry interaction. Over the years, several combustion models have been developed for LES (Peters, 2000; Poinsot & Veynante, 2005) and they are briefly summarized in the following. Overall, combustion models of LES can be classified into two categories. The first class of model is combustion regime agnostic and includes eddy dissipation model/eddy break up model (Spalding, 1971; Magnussen, 1981), linear eddy model (Kerstein, 1992) and the filtered probability density function method (Pope, 1991; Haworth, 2010). These models generally require the direct evaluation of the reaction chemistry but detailed descriptions of chemistry usually consist of large number of elementary chemical reactions. Therefore, reduced chemical kinetics or chemistry simplification techniques such as intrinsic low-dimensional manifolds (ILDM) (Maas & Pope, 1992) are usually employed in conjunction with these combustion models.

Other modeling approaches utilize certain assumptions of the flame structure to describe the turbulent chemistry interaction. In general, these models are designed to capture the dynamics of either premixed flames or non-premixed flames. There are distinct models for these two types of flames because the physical phenomena that control the chemical reaction are different for these two scenarios. Premixed flames are characterized by flame propagation (Kuo, 2005). Since turbulence is shown to be able to affect the speed at which the flame can propagate (Clavin & Williams, 1979), it is necessary for premixed flame models to account for the effects of turbulence on premixed flame. Examples of turbulent premixed flame models are the Thickened Flame model (Colin *et al.*, 2000), Flamelet Pro-

longation of ILDM (Gicquel *et al.*, 2000) or Flamelet Generated Manifolds (Oijen & Goey, 2000) , and G-equation model (Peters, 1999). On the other side, non-premixed flames are controlled by the mixing of fuel and oxidizer (Bilger, 1976) and the reaction zone is restricted to locations in which the reactants are well-mixed. Therefore, turbulent non-premixed flame models need to accurately capture the advection and diffusion of reactants. Conditional Moment Closure (Klimenko & Bilger, 1999; Bilger, 1993) and non-premixed flamelet models (Peters, 1984; Ihme, 2007; Pierce & Moin, 2004) are some examples of turbulent non-premixed flame models used in LES.

Combustion processes in most gas turbine combustor are usually not purely premixed or non-premixed. In a lean premixed model combustor based on a Turbomeca industrial burner (Meier *et al.*, 2007), Raman measurements showed considerably variation of mixedness of fuel and oxidizer. A subsequent numerical study by Franzelli *et al.* (2012) has shown that the mixing of fuel and oxidizer needs to be considered for the accurate prediction of flame structures in this combustor. Although regime-dependent models are developed for ideal conditions, Pitsch & Steiner (2000), Ihme *et al.* (2005) and Vreman *et al.* (2009) have successfully applied these types of models in LES of partially premixed Methane/air flames (Barlow & Frank, 1998; Barlow, 1996). Generally, the results of these simulations are in good agreement with measurements.

1.3 Low Order Models

Although lean premixed/prevaporized combustion has been shown to reduce pollutant emission, this combustion mode is susceptible to flame instabilities (Lieuwen & McManus, 2003). Moreover, the combustor is tightly coupled with the rest of the gas turbine engine so that upstream conditions may destabilize the flame. Therefore, the combustor has to be tested for a wide range of operating conditions in order to ensure the system stability. High-fidelity simulations can assist in the prediction of flame instability but its high compu-

tational cost precludes its application from routine calculations of each possible operation scenario. In this regard, low-order predictive methods are better suited for such applications due to the reduced computational cost, but these methods are usually less accurate than the high-fidelity approaches. With the increasing availability of high fidelity simulations, it is possible now to complement low-order methods with results of high fidelity simulations to increase the accuracy of the former.

Thermo-acoustics instabilities, if present in the gas turbine engine combustors, pose significant risk to the safety of the engine. In addition, such instabilities are commonly observed in lean premixed/prevaporized combustion systems (Lieuwen & McManus, 2003). Therefore, low-order models have been developed to predict the acoustics response of the combustor as well as the entire engine. One of the method is the network model in which the acoustic dynamic of an engine is reproduced with a series of connected acoustic elements (Poinsot & Veynante, 2005). Linear acoustics transfer functions are prescribed to each of these acoustic elements and the resulting linear system can be solved in frequency space. Since a flame is present in the combustor during operation, its response to acoustic perturbations can be represented by a flame transfer function (Crocco & Cheng, 1956) .

The flame transfer function, under the thin flame assumption, can be approximated as a heat release term with gain and time-lag components. Finding the correct values for these two parameters becomes a very important task, since the accuracy of the low-order model is highly dependent on these two parameters. Past research has shown that the model parameters of realistic combustors can be dependent on excitation frequency, fluctuations of equivalent ratio, and velocity (Lieuwen & McManus, 2003). Therefore, the gain and time-lag of the model can be highly dependent on the operating condition and the combustor configuration. These parameters are usually obtained from experimental investigations but researchers have begun to use LES to computationally determine these parameters (Chong *et al.*, 2010) .

In addition to acoustics modes, hydrodynamic instabilities are another important pro-

cess that can modify the flame response. As mentioned earlier, the swirling flow inside a realistic injector can usually induce regions of strong shear that may support hydrodynamic instabilities (Wang *et al.*, 2005). In non-premixed flames and to some extent for partially premixed flames, vortices induced by this type of instability can enhance or impede the mixing of reactants, thus altering the time lag and combustion intensities of the flame. In addition, there can be absolute hydrodynamic instabilities in swirl combustors where these instabilities are sustained even without continuous external forcing. The precessing vortex core (PVC) is an example of such instabilities in a swirl combustor and commonly observed in industrial scale burners (Syred, 2006). Moreover, the hydrodynamic instability can also couple with acoustics fluctuations and generate different vortical structures that are driven by the frequency of the external perturbation (Ho & Huerre, 1984).

Linear stability analysis has been extensively used to investigate hydrodynamic instabilities (Schmid & Henningson, 2001). In the early utilization of this analysis method, simple flows have been considered because the governing equations need to be linearized around a base flow and analytical solutions to simple problems were only available. Due to this limitation, this method was exclusively employed for the theoretical characterization of instabilities in planar reacting mixing layers (Shin & Ferziger, 1991; Trouve *et al.*, 1988). Following the development of numerical methods, the linear equations can now be discretized and solved numerically. This opens up new applications of the linear analysis and more complex configurations can be solved numerically. As a result, linear methods have been applied to flow behind involving shocks (Mack *et al.*, 2008), low pressure turbine blades (Sharma *et al.*, 2011), and iso-thermal gas turbine injectors (Juniper, 2012). Despite that, its application to reacting flow is still limited to canonical jets or planar flames in which simple one-step chemistry models are usually employed.

Both acoustics network method and linear stability analysis are linear methods. However, the flow dynamics can be largely non-linear at large amplitude of oscillation and the linear methods may not be accurate. This is especially true in reacting flows as the chem-

ical source term is very stiff and highly sensitive to thermodynamic variations. To some extent, these effects can be captured with the model parameters of the acoustics analysis but the determination of these parameters under all possible variations of combustion environment is not feasible. A novel approach to low-order modeling is to restrict the unsteady flow solutions to a set of pre-computed empirical modes (Noack *et al.*, 2005; Noack *et al.*, 2008; Bergmann *et al.*, 2009). This new class of methods has shown some promises but is still in the early stages of research and development.

1.4 Roadmap and Scope

The overall objective of this thesis is to develop modeling capability that enables the investigation of gas turbine combustors. Specifically, low-order models such as parallel flow instability analysis will be utilized to assess the response of the combustor to a wide range of perturbations. The role of detailed simulation capabilities that are being developed will be to predict the full dynamics of combustors. By utilizing both low-order capability and high-fidelity methods, it is expected that the resulting approach can be applicable for a wider range of combustion dynamics.

However, combustion models that are common in linear stability analysis are not consistent with high-fidelity simulations. The incompatibility of thermo-chemical descriptions needs to be reconciled before the two methods can be integrated into a useful framework. Moreover, the utilization of high fidelity simulations for reacting flow predictions in complex combustion environments is currently limited to research settings. The main reason for its limited adoption is the extensive computational cost of such simulations. In particular, chemical kinetics evaluation can consume significant amount of computational resources. Therefore, regime dependent flamelet models are commonly used in simulations such as LES since they allow for the computationally efficient evaluation of the reaction chemistry through tabulation.

The scope of this thesis is to extend linear stability analysis to incorporate flamelet models that are utilized in LES. With this addition, linear stability analysis is used in conjunction with detailed simulations to elucidate the hydrodynamic instabilities of a buoyant non-premixed jet flame. Besides that, a gas turbine model combustor is also investigated in this work. For this more complex configuration, comprehensive LES calculations are performed.

1.4.1 Linear Stability Analysis of a Buoyant Jet Diffusion Flame

Instabilities in laminar non-premixed flames have been investigated experimentally, theoretically, and computationally. Early experiments on the subject are primarily concerned with the flame flickering due to buoyancy induced instabilities. In particular, Chen *et al.* (1989) used Mie-scattering to characterize vortical structures in the inner and outer regions of non-premixed flames. These vortical structures are attributed to hydrodynamic instabilities, and the periodical roll-up of vortex inside jet flame is the result of an inner instability mode. Further outward from the jet flame, the outer instability mode is responsible for the slowly bulging and necking of the flame. In fact, this investigation was partially motivated by the linear stability analysis of Buckmaster & Peters (1988). Buckmaster & Peters (1988), through theoretical analysis of an infinite candle flame, have identified a modified Kelvin-Helmholtz mode, exhibiting the most unstable mode of a frequency of 17Hz. This result is in agreement with the experiment by Chen *et al.* (1989) , which is remarkable considering that the analysis was performed at arbitrary downstream location while neglecting viscous and buoyancy effects.

Katta & Roquemore (1993) performed several numerical simulations of a buoyant propane jet diffusion flame to reproduce the experiment of Roquemore *et al.* (1989). By using an infinitely fast chemistry model, detailed simulations of Katta & Roquemore (1993) are able predict experimentally measured temperature to a reasonable agreement. Two instabilities mode were also present in their simulations and the frequency of the outer mode

oscillation agrees with experimental measurements. However, the outer mode is no longer present when buoyancy is neglected in the simulations. Based on this outcome, the outer instability is likely be driven by buoyancy effects. In addition, Katta & Roquemore (1993) also reported that the inner instability mode is significantly dampened when buoyancy effects are neglected.

Because of its geometric simplicity, the planar reacting shear-layer is also considered for investigation of hydrodynamic instabilities in non-premixed flames. In an early work on reacting shear layers, Shin & Ferziger (1991) identified three distinct instability modes, namely a central mode in the middle of the shear layer, two inner and outer modes that originate from both fuel and oxidizer streams. Through inviscid linear analysis, Shin & Ferziger (1991) found that heat release suppresses the central hydrodynamic mode in a shear layer and amplifies the two outer modes. This work is complemented by Day *et al.* (1998) who performed a comprehensive parametric study to elucidate effects of compressibility, density ratio, velocity ratio and heat release on the three instability modes. Compressibility, heat release, and fuel/oxidizer density ratio was found to have stronger effects on the flow structure compared to equivalence ratio and the velocity difference between both streams.

Since the review of Huerre & Monkewitz (1990) on the concept of absolutely and convectively unstable flows, more recent investigations on buoyant non-premixed flames (Lingens *et al.*, 1996; Maxworthy, 1999; Juniper *et al.*, 2009) are mostly related to the absolute instability in flames. In an experiment complimented by linear analysis, Lingens *et al.* (1996) concluded that the buoyant non-premixed flame is absolutely unstable. Although buoyancy effects are neglected in their analysis, Lingens *et al.* (1996) discovered the transition of the instability from convective to marginally absolute at one nozzle diameter downstream of the nozzle exit. An experimental investigation on flame sensitivity to modifications of the configurations also confirmed that the buoyant jet diffusion flames are absolutely unstable (Maxworthy, 1999). Similarly, Juniper *et al.* (2009) introduced external perturbations to a buoyant methane-air flame and found that the natural frequency of

the flame is resilient to external disturbances. This property is attributed to a large absolute unstable region in the flame.

In most linear stability analysis of chemically reacting flows, model-approximations for velocity field, thermo-viscous-diffusive transport and reaction chemistry are commonly employed to make the analysis more tractable. For instance, analytical profiles are usually used as the base-flow in analysis so that the shear layer thickness can be specified as a parameter (Michalke, 1984). The effect of viscosity is also neglected in most investigations. However, the temperature change induced by reaction is significant and can lead to substantial variations in viscosity. To capture these effects, more detailed linear analysis methods assume that the viscosity is linearly dependent on temperature. This is referred to as Chapman approximation. Moreover, the reaction chemistry is usually limited to one-step chemistry, which only provides an incomplete description of the flame structure in non-premixed flames.

In Chap. 3, linear stability analysis is combined with a flamelet model so that the method utilizes a combustion model that is consistent with that of the high fidelity methods. This extended analysis method is utilized to study the effect of several model approximations on the results of the flow instability. More specifically, we are considering several choices of base-flow profiles, different gas laws, transport models of varying fidelity and two representations of reaction chemistry. The non-premixed jet flame studied by Füri (2001) is here employed as the basis for this investigation. In addition, we also characterize two instability modes that are generally present in a buoyant non-premixed jet flame.

1.4.2 Large Eddy Simulation of a Gas Turbine Model Combustor

LES is a high fidelity simulation approach that can be utilized to predict the characteristics of gas turbine combustors. Apte *et al.* (2003), Boudier *et al.* (2007) and Ihme & Pitsch (2008) have applied this simulation method to realistic gas turbine combustors. However, it is difficult to assess the accuracy of the LES results since comparisons with experimental

measurements are mostly limited to conditions at the combustion exit. Even in the best cases, only intrusive measurement techniques are likely be employed to obtain the flow field information within combustors. This is due to the lack of optical access in real combustors which is required to deploy non-intrusive diagnostics techniques such as Raman spectroscopy and Planar Laser Induced Fluorescence (PLIF).

Gas turbine model combustors are better suited as platforms for assessing the accuracy of LES methodologies. Model combustors are laboratory scale burners that contain parts of actual combustors. However, the combustor chamber is usually modified to include optical access so that non-intrusive diagnostics can be used to obtain quantitative measurements within the combustor. For example, the Preccinsta model combustor (Meier *et al.*, 2007) employs a swirler that is derived from a Turbomeca combustor but features a largely transparent combustor chamber which is not found in actual combustors. For this burner, Meier *et al.* (2007) have utilized Laser Doppler Velocimetry (LDV) and Raman spectroscopy to quantitatively characterize the flow field inside the burner. These quantitative data are not only useful for the validation of numerical codes, but are essential in the investigation of the thermo-acoustics feedback mechanisms.

LES calculations of the Preccinsta burner have been performed by Roux *et al.* (2005), Galpin *et al.* (2008), Fiorina *et al.* (2010), Moureau *et al.* (2011), and Franzelli *et al.* (2012). Since the injection of gaseous fuel occurs before the swirler, the combustion mode of this burner corresponds to that of a premixed flame. Therefore, premixed flame models have been utilized in all of these LES studies. Overall, these validation efforts showed that LES results are in reasonable agreement with experimental measurements. In addition to LES calculations, Moureau *et al.* (2011) also considered a simulation case in which turbulent models were not employed for a mesh of 2.6 billion elements. Based on the analysis of these results, the presumed-PDF models are shown to be reasonable for modeling of the filtered source term. In the experiment by Meier *et al.* (2007), the imperfect mixing of fuel and air is shown to be a possible cause for thermo-acoustics instabilities for one of the

operating conditions. With the exception of the work by Franzelli *et al.* (2012), most LES studies of this burner do not account for the unmixedness of the reactants. By including this effect, Franzelli *et al.* (2012) were able to accurately predict thermo-acoustic instabilities.

Prior to the aforementioned combined numerical and experiment investigations on a gas turbine model combustor, the TECFLAM burner (Landenfeld *et al.*, 1998) is another configuration in which similar validation efforts were carried out. This burner consists of a movable block swirl nozzle and a central bluff body. Unlike the Preccinsta combustor, this burner is unconfined. Instead of being connected to a chamber, the swirler and nozzle assembly is placed inside a coflow of air. The burner also operates in a premixed combustion mode as the fuel and air are premixed prior entrance to the swirler. Early applications of detailed simulations (Landenfeld *et al.*, 1998) yield mean velocities that agree reasonably well with experimental results. However, the temperature is overall under-predicted by 200K. More recent LES calculations with flamelet models by Kuenne *et al.* (2011), Ketelheun *et al.* (2013) and Schmitt *et al.* (2013) showed better agreement with newer experimental measurements (Gregor *et al.*, 2009; Schneider *et al.*, 2005) for velocities, temperature and major species. The swirler assembly was included in the computational domain of these LES studies while the early simulation efforts (Landenfeld *et al.*, 1998) only consider the flow after the nozzle exit. In addition, Jones *et al.* (2012) have performed an LES calculation of this configuration a transported PDF approach.

The two model combustor configurations described above operate in the premixed combustion regime. However, combustors in aircraft engines tend to operate at non-premixed and partially premixed conditions. To address this issue, Janus *et al.* (2007) experimentally characterized a model combustor (MOLECULES) in which fuel and air are not premixed before entering the swirlers. Moreover, the air is preheat and the operating pressure is elevated to mimic conditions of an aircraft engine. Wegner *et al.* (2007), Staufer & Janicka (2009) and Auzillon *et al.* (2012) have performed LES calculations of this burner and the results agree with experiments. However, comparisons with experimental measurements

are only limited to velocities. A more quantitative assessment of LES combustion models is not possible in this combustor configuration without comparisons with measurements of temperature and species.

Overall, favorable comparisons of LES results with experimental measurements in model combustors illustrate the capability of this method in predicting the characteristics of realistic combustors. In particular, a significant body of work has been established to validate this numerical approach in premixed burners. However, this is not available for partially premixed model combustors. Partially premixing can introduces additional challenges for turbulent combustion models as most of the validation studies of premixed burner employed regime dependent combustion model. In partially-premixed combustors, it is not possible to categorize if the flame is premixed or non-premixed.

One objective of this work is to extend the validation effort of the LES methodology for model combustors. Specifically, our focus is on a gas turbine model combustor (GTMC) which operates in a partially premixed mode (Weigand *et al.*, 2006; Meier *et al.*, 2006). The fuel injection ports of this model combustor are recessed so that the flame is considered partially premixed. Moreover, this combustor also features dual swirlers, representing a more complex configuration than that of previous numerical simulations. The additional swirler introduces more flow dynamics that needs to be accurately resolved in LES.

1.5 Accomplishments

The significant and novel contributions of this work are summarize in the following:

- Introduced non-premixed flamelet model to linear stability analysis of diffusion flames. By using a non-premixed flamelet model in the analysis, more complex chemistry effect can be accounted for in the analysis without rendering the solution strategy intractable. In addition, the flamelet model is widely used in high-fidelity simulation so the linear analysis is consistent with data obtained from these simulations. This

makes the low-order method an ideal complement to high fidelity simulations.

- Through linear stability analysis and simulations, the effect of transport and reaction chemistry on the instability is elucidated for a buoyant diffusion jet flame. Several fluid and combustion models are considered and the use of simpler models was found to generally lead to lower predictions for the growth rate of the Kelvin-Helmholtz instabilities in flames.

- The Flamelet/Progress Variable model is extended for simulation of the flame A condition of the GTMC. To model the extinction and re-ignition of flame that are in this operating condition, the unresolved fluctuation of progress variable is considered in the PDF model. Since the flame is partially premixed, premixed combustion models are also tested here to investigate the limitation of regime-dependent flamelet model.

- A core-noise model has been developed to study the generation, transmission, propagation and radiation of noise in the flow path of a gas turbine. Downstream entropy perturbations of the GTMC are used as input to study indirect combustion noise. Computational Aero-Acoustic (CAA) simulations of a converging nozzle reveal that higher-frequency entropy fluctuations produce noise with a preferred angle of diffraction.

CHAPTER 2

Mathematical Model

2.1 Transport Equations

For gaseous reacting flows within the continuum limit, the general form of governing equation is

$$\frac{\partial \rho}{\partial t} + \nabla \cdot (\rho \boldsymbol{u}) = 0 \ , \tag{2.1a}$$

$$\frac{\partial \rho \boldsymbol{u}}{\partial t} + \nabla \cdot (\rho \boldsymbol{u} \otimes \boldsymbol{u}) = -\nabla p + \nabla \cdot \underline{\underline{\tau}} + \rho \sum_i Y_i \boldsymbol{g}_i \ , \tag{2.1b}$$

$$\frac{\partial \rho E}{\partial t} + \nabla \cdot (\rho \boldsymbol{u} H) = \nabla \left(\underline{\underline{\tau}} \cdot \boldsymbol{u} \right) - \nabla \cdot \boldsymbol{q} + \dot{Q} - \rho \sum_i Y_i \boldsymbol{g}_i \cdot \boldsymbol{V}_i \ , \tag{2.1c}$$

$$\frac{\partial \rho Y_i}{\partial t} + \nabla \cdot (\rho \boldsymbol{u} Y_i) = -\nabla \cdot (\rho \boldsymbol{V}_i Y_i) + \rho \dot{\omega}_i. \tag{2.1d}$$

The viscous stress tensor is

$$\underline{\underline{\tau}} = \mu \left[\nabla \boldsymbol{u} + (\nabla \boldsymbol{u})^T \right] - \mu_b \nabla \boldsymbol{u} \cdot \underline{\underline{I}}. \tag{2.2}$$

The heat flux vector can be separated into three components as

$$\begin{aligned}\boldsymbol{q} &= \boldsymbol{q}_{\text{conduction}} + \boldsymbol{q}_{\text{interdiffusion}} + \boldsymbol{q}_{\text{Dufour}} \\ &= -\lambda \nabla T + \rho \sum_{i=1}^{N_s} h_i Y_i \boldsymbol{V}_i + R_u T \sum_{i=1}^{N_s} \sum_{j=1}^{N_s} \left(\frac{X_j \alpha_i}{W_i \mathcal{D}_{ij}} \right) (\boldsymbol{V}_i - \boldsymbol{V}_j) \,. \end{aligned} \tag{2.3}$$

The conduction term, $\boldsymbol{q}_{\text{conduction}}$, is obtained using Fourier's law whereas the second component represents the inter-diffusion of different chemical species. The Dufour heat flux is produced by mass diffusion of chemical species and is typically small in most applications (Kuo, 2005).

The diffusion velocities $\boldsymbol{V}_i$ appearing in the above equations can be obtained using kinetic theory and the resulting implicit equation is

$$\begin{aligned}\sum_{j=1}^{N_s} \frac{X_i X_j}{\mathcal{D}_{ij}} (\boldsymbol{V}_j - \boldsymbol{V}_i) =& \nabla X_i + (X_i - Y_i) \frac{\nabla p}{p} \\ &+ \frac{\rho}{p} \sum_{j=1}^{N_s} Y_i Y_j (\boldsymbol{g}_j - \boldsymbol{g}_i) + \sum_{j=1}^{N_s} \frac{X_i X_j}{\rho \mathcal{D}_{ij}} \left(\frac{\alpha_j}{Y_i} - \frac{\alpha_i}{Y_j} \right) \frac{\nabla T}{T}. \end{aligned} \tag{2.4}$$

The right-hand side terms of Eq. (2.4) represent, respectively, the diffusion of species due to concentration gradients, pressure-gradient, body forces and the Soret effect. The Soret effect, which is the reciprocal to the Dufour effect, is the diffusion of species due to temperature gradients. If the last three terms are neglected, Eq. (2.4) reduces to the Stefan-Maxwell model.

Note that

$$\sum_i Y_i = 1 \,, \tag{2.5}$$

by the definition of mass fraction. This constraint requires that

$$\sum_i \dot{\omega}_i = 0 \quad \text{and} \quad \sum_i Y_i \boldsymbol{V}_i = 0 \,. \tag{2.6}$$

to ensure the total mass conservation of the system.

2.1.1 Auxiliary Equations and Simplifying Assumptions

The expressions for fluxes and diffusion velocity listed in Eqs. (2.2)–(2.4) are not sufficient to close the governing equations. To achieve closure, transport properties, chemical source terms and thermodynamics properties need to be calculated using additional relations that are valid under certain assumptions. These relations and the associated assumptions are listed below:

1. Ideal gas law: The ideal gas law for multi-component gas is

$$p = \rho R_u \sum_{i=1}^{N_s} \frac{Y_i}{W_i} T. \tag{2.7}$$

   This equation can be derived from kinetic theory after neglecting intermolecular forces and utilizing Dalton's law of partial pressures. These assumptions are justified in most combustion applications as they occur mostly in low densities environment. In such conditions, the distances between molecules are large enough such that the intermolecular forces can be neglected (Vincenti & Kruger, 1975).

2. Mixture of thermally perfect gas: The total energy and total enthalpy, appearing in Eq. (2.1c), each consists of a sensible component, the total heat of formation and the kinetic energy. Under thermally perfect gas assumptions, the sensible enthalpy of the chemical species i can be evaluated as

$$h_{sensible,i} = \int C_{p,i}(T) dT \ . \tag{2.8}$$

   This assumption is reasonable as pressure variations in gas turbine engine combustors are usually not large enough to cause significant change in the specific heat capacities. In fact, most analyses of thermodynamic cycle for the gas turbine engine usually

assume constant pressure combustion in the combustors.

3. Body forces: The only body force relevant to this study is the gravity and it is equally exerted on all chemical species, *i.e.*

$$\boldsymbol{g}_i = \boldsymbol{g} \quad \forall\, i\ . \tag{2.9}$$

4. Mixture-averaged properties: The transport properties such as μ, λ and $\boldsymbol{V}_i$ are evaluated through the CHEMKIN library. Nevertheless, the procedures employed by the software library (Kee *et al.*, 1986) are reiterated briefly here for completeness. In a multiple species mixture, the μ and λ of each chemical species are computed using models based on kinetic theory (Hirschfelder *et al.*, 1954) and then averaged to provide an overall transport description of the mixture.

   To account for the diffusion of species, Fick's law is utilized in this work instead of the full multi-component expression in Eq. (2.4) By defining an effective binary diffusion $\mathcal{D}_{im}$ (Kuo, 2005) for the species i in a mixture, the Stefan-Maxwell equation can be approximated to

$$\boldsymbol{V}_i = -\mathcal{D}_{im}\frac{\nabla X_i}{X_i} + \boldsymbol{V}_c. \tag{2.10}$$

   The correction velocity $\boldsymbol{V}_c$ is introduced to account for the discrepancy between the bulk velocity and the molar-averaged velocity.

   In most combustion applications, Poinsot & Veynante (2005) have shown that Fick's law is sufficiently accurate to capture the species diffusion process. In fact, the species mass diffusion term in Eq. (2.1d) is commonly simplified in combustion processes to

$$\begin{aligned}\rho\left(\mathcal{D}_{im}\frac{Y_i}{X_i}\nabla X_i + \boldsymbol{V}_c Y_i\right) &= \rho\left[\mathcal{D}_{im}\nabla Y_i + \mathcal{D}_{im}Y_i\nabla ln(W) + \boldsymbol{V}_c Y_i\right] \\ &\approx \rho\mathcal{D}_{im}\nabla Y_i. \end{aligned}\tag{2.11}$$

Smooke (1991) has employed this model for methane-air flames and obtained reasonable results for both premixed and non-premixed flames.

5. Equal diffusivities: In the present work, all species are assumed to have the same mass diffusivity. This is a reasonable approximation for methane-air combustion since the major chemical species of this combustion system share very similar mass diffusivities. In turbulent non-premixed flames, the error resulted from this simplification can be smaller if the reaction-diffusion layer is very thin. Outside the thin layer, turbulence is mainly responsible for large scale diffusion of species and heat. As turbulence mixing affects all species indiscriminately, the effect of differential mass diffusivity is relatively small (Pitsch, 2000).

   The Lewis number for the species i, is defined as

$$Le_i = \frac{\lambda}{\rho C_p \mathcal{D}_{im}}. \tag{2.12}$$

   Since equal mass diffusivities are assumed here, there is only one Lewis number. Furthermore, the Lewis number is assumed to be unity in this study as the Lewis numbers of air and methane are close to 1.

6. Stokes' hypothesis: Stokes' hypothesis for a Newtonian fluid is that the bulk viscosity can be related to the molecular viscosity

$$\mu_b = -\frac{2}{3}\mu \ . \tag{2.13}$$

7. Low Mach number approximation: The energy balance equation can be simplified using the so-called "low Mach number approximation" (Pierce, 2001) where $O(M) < 0.3$. In this approximation, effects of acoustics and viscous heating are neglected. the neglected effects can be important even in a low Mach number environment.

In most turbulent reacting flows, the increase of the sensible enthalpy due to reaction is usually much larger than that of viscous dissipation. This is because the viscous heating term is inversely related to Reynolds number and Eckert number, and turbulent combustion usually occurs at conditions of high Reynolds number and Eckert number. Hence, neglecting viscous dissipation is a reasonable approximation for the turbulent combustion scenarios studied here.

Caution has to be exercised when excluding acoustics contributions in a combustion system as thermo-acoustic instabilities may be present in a confined combustor. If it can be proved via other means that this phenomenon does not occur in a specific case, acoustics propagation of pressure can be ignored. Under this simplifying assumption, thermo-chemical variables such as density, temperature and the chemical composition are no longer dependent on the small variations in pressure,

$$\boldsymbol{\phi}\left(H, \boldsymbol{Y}, p_0 + \delta p\right) \approx \boldsymbol{\phi}\left(H, \boldsymbol{Y}, p_0\right) \tag{2.14}$$

An interesting implication that emerges from this treatment is the infinite speed of sound. This introduces an additional elliptical constraint to the governing equations. Furthermore, the pressure contribution, contained in the enthalpy equation, can also be ignored in open combustion systems as it is usually assumed that p_0 of these systems is uniform and constant.

2.2 Combustion Models

2.2.1 Non-Premixed Flamelet Model

In non-premixed flames, the fuel and oxidizer streams are separated initially and the mixing of reactants usually occurs during the combustion stage. In most non-premixed jet flames, there exists a mathematically defined surface where the mixture attains the stoichiometric

ratio of fuel and oxidizer. Since the stoichiometric ratio is where the complete consumption of the reactants is possible, most of the exothermic reactions are likely to be confined to a layer near the stoichiometric surface. In this reaction zone, the production of heat and combustion products are balanced by the diffusion of heat and products. Furthermore, chemical reactions usually occur faster than the convection and diffusion processes so the diffusion of reactants is likely be the rate limiting factor to the combustion processes in steady non-premixed flames. Therefore, non-premixed flames are also referred to as diffusion flames.

2.2.1.1 Mixture Fraction

As mentioned earlier, non-premixed flames are mostly characterized by the mixing of fuel with oxidizer prior to combustion. Therefore, it is convenient to define a conserved scalar or mixture fraction that can represent the ratio of chemical species originating from fuel and oxidizer streams. There are several definitions of the mixture fraction but most of them are based on the stoichiometric condition described by the global reaction equation, *i.e.*

$$\sum_i \nu_i' \mathcal{M}_i \rightarrow P \ , \tag{2.15}$$

One of the general definitions of the mixture fraction is constructed using a linear combination of the element mass fractions (Bilger, 1976). The element mass fractions Z_j can be obtained from the species mass fractions as

$$Z_j = \sum_i \frac{n_{ij} W_j}{W_i} Y_i \ , \tag{2.16}$$

where W_j is the atomic mass of the element j, n_{ij} is the number of element j in a molecule of the species i. In principle, any Z_j is also a conserved scalar but the value of Z_j at the stoichiometric condition is not the same. The classical definition of a coupling function by Burke & Schumann (1928) can be obtained through a linear combination of Z_j. For

example, the coupling function for the methane-air combustion can be expressed as

$$\xi = \frac{Z_C}{W_C} + \frac{Z_H}{4W_H} - \frac{Z_O}{2W_O} \ . \tag{2.17}$$

ξ is zero at stoichiometric mixture and the ratio ξ_F/ξ_O is consistent with the coupling function defined by Burke & Schumann (1928). Furthermore, the mixture fraction, by convention, is defined to be unity for the fuel stream and zero at the oxidizer stream. This constraint is achieved by normalizing ξ with

$$Z = \frac{\xi - \xi_O}{\xi_F - \xi_O} \ . \tag{2.18}$$

Since Z is a linear combination of Z_j, its transport equation is

$$\frac{\partial \rho Z}{\partial t} + \nabla \cdot (\rho \boldsymbol{u} Z) = \nabla \cdot (\rho D_Z \nabla Z) \ . \tag{2.19}$$

Unless all chemical species have equal diffusivity, the determination of D_Z is ambiguous. Peters (2000) mentioned that the enthalpy transport equation also shares the same form under certain assumptions, hence D_Z is assumed to be the thermal diffusivity υ here.

2.2.1.2 Stationary Laminar Flamelet Model

In the laminar flamelet model, a turbulent flame is assumed to be an ensemble of 1D laminar flames. These 1D flames are so-called flamelets and are assumed to be able to capture the flame structures in the reaction zones. The laminar flamelet model is shown to be valid if there is a scale separation between the convection-diffusion processes and chemical reactions. In the context of turbulent flames, turbulent eddies must not penetrate the reaction zones in the flamelet regime. Instead, turbulence is only allowed to deform and stretch the thin flame sheet in this model. These assumptions may seem overly restrictive at first but Seshadri & Peters (1988) have shown that the non-premixed flamelet concept to be valid

below Karlovitz number of 190 where Karlovitz number, Ka, is the ratio of chemical time scale to the turbulent time scale. This is a relatively large upper bound considering that Lentini (1994) reported that the Karlovitz number of a $Re = 40000$ jet diffusion flame is lower than 10.

The non-premixed flamelet equation can be formulated by defining a flame-local coordinate system that is attached to the stoichiometric surface of a non-premixed flame. In this coordinate system, the mixture fraction gradient is utilized to define the first coordinate and the remaining two directions can be arbitrary as only dynamics along the first coordinate are accounted for in the flamelet model. The resulting Crocco-type transformation is

$$(t, x_1, x_2, x_3) \rightarrow (\tau, Z(t, \boldsymbol{x}, Z_2, Z_3)) \,. \tag{2.20}$$

Applying Eq. (2.20) to the temporal and spatial derivatives yields

$$\frac{\partial}{\partial t} \rightarrow \frac{\partial}{\partial \tau} + \frac{\partial Z}{\partial t}\frac{\partial}{\partial Z}, \tag{2.21a}$$

$$\nabla \rightarrow \nabla Z \frac{\partial}{\partial Z} + \nabla_\perp \,, \tag{2.21b}$$

where the subscript $\perp$ denotes spatial effects that are perpendicular to the gradient of Z. Using these transformed operators, Eqs. (2.1d and 2.1c) can be expressed as

$$\rho\frac{\partial \boldsymbol{\psi}}{\partial t} - \frac{1}{2}\rho\chi_Z\frac{\partial^2 \boldsymbol{\psi}}{\partial Z^2} - \dot{\boldsymbol{m}} = RHS_\perp, \tag{2.22}$$

where $\boldsymbol{\psi} = \left(\boldsymbol{Y}^T, H\right)^T$, $\dot{\boldsymbol{m}} = \left(\rho\dot{\boldsymbol{\omega}}^T, -\dot{Q}\right)^T$, and right side terms that are orthogonal to ∇Z are contain in $RHS_\perp$. Using asymptotic analysis, Peters (2000) has shown that the term $RHS_\perp$ is of higher order and can be neglected in the instance of thin reaction zones.

After ignoring the unsteady and higher order terms found in Eq. (2.22), the stationary laminar flamelet model (SFLM) is obtained. This procedure yields the steady state equa-

tion:

$$-\frac{1}{2}\chi_Z\frac{\partial^2\boldsymbol{\psi}}{\partial Z^2}=\frac{\dot{\boldsymbol{m}}}{\rho}. \tag{2.23}$$

The scalar dissipation rate $\chi_Z = 2D_Z|\nabla Z|^2$ appears to be a parameter that needs to be specified as a function of Z. Ideally, one would like to use $\chi_Z(Z)$ tailored to a specific flame configuration but this approach is impractical. Typically, the prescribed profiles of $\chi_Z(Z)$ are based on the analytical solution of a 1D mixing layer problem (Peters, 2000). The scalar dissipation rate for this problem is

$$\chi_Z\left(Z\right)=\chi_{Z,st}\exp\left\{2\left[\mathrm{erfc}^{-1}\left(2\mathrm{Z_{st}}\right)\right]^2-2\left[\mathrm{erfc}^{-1}\left(2\mathrm{Z}\right)\right]^2\right\}, \tag{2.24}$$

where Z_{st} is the mixture fraction evaluated at stoichiometric condition and $\chi_{Z,st}$ is $\chi_Z(Z_{st})$ With this expansion, the solutions to Eq. (2.23) are dependent on the parameter $\chi_{Z,st}$. By varying $\chi_{Z,st}$ while keeping the boundary conditions at $Z = 0$ and $Z = 1$ fixed, the solutions to Eq. (2.23) can be collapsed unto a so-called "S-shaped curve". An example of this curve of solutions is shown in Fig. 2.23 where different solution branches can exist. The lower and upper solution branches correspond to the non-reacting states and the stable burning states, respectively. The middle solution branch represents the unstable states so it may not be realizable in a steady state condition. However, this solution branch can be applicable in transient scenarios such as an igniting flame.

If the boundary conditions of Eq. (2.23) are imposed with the properties of fuel and oxidizer of a steady jet flame, the solutions to this equation are assumed to be the flamelets for this jet flame. Moreover, the thermo-chemical properties $\boldsymbol{\psi}$ of the flamelets can be represented by a 2D manifold of the form:

$$\boldsymbol{\psi}=\mathcal{G}_{SLFM,\boldsymbol{\psi}}\left(Z,\chi_{Z,st}\right). \tag{2.25}$$

Using this parameterization, the steady flamelet profiles are usually assembled into a library

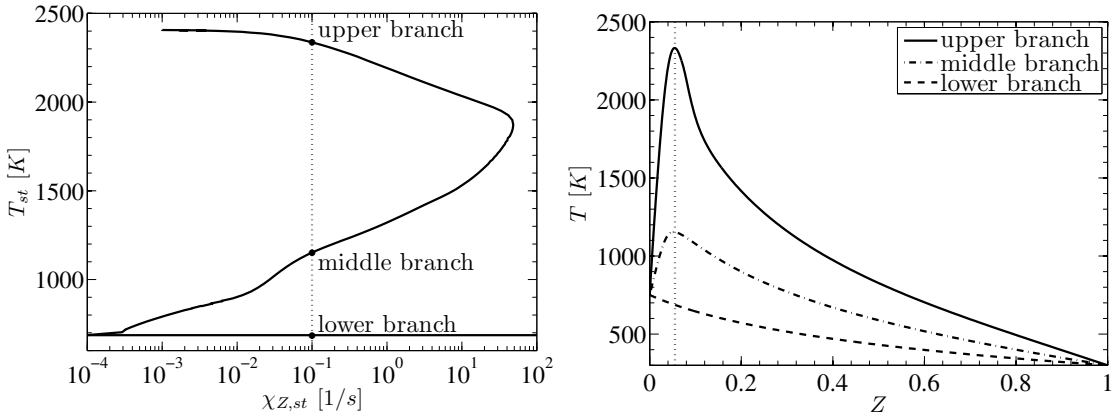

(a) S-shaped curve.

(b) Temperature profiles of flamelets at $\chi = 0.1/s$.

Figure 2.1: left: The S-shaped curve of steady flamelet solutions to a methane-air combustion system ($T_F = 300K$, $T_O = 750K$, $p = 1$bar). The flamelet solutions are multi-valued for a certain range of $\chi_{Z,st}$, and this is shown at $\chi_{Z,st} = 0.1$ where there are three branches of solutions. right: the temperature profiles of the upper branch, middle branch and lower branch solutions at $\chi_{Z,st} = 0.1$ are shown for the comparison of the flame structures.

to account for complex chemistry effects in numerical simulations (Peters, 2000).

2.2.1.3 Flamelet/Progress Variable Model

The mapping of thermo-chemical properties (shown in Eq. (2.25)) is the core of the SLFM model. However, Fig. 2.1a shows that this mapping can be multi-valued, making a unique parameterization of the flamelet solutions with $\chi_{Z,st}$ impossible. Nevertheless, the SLFM is used in practice by only accounting for the stable burning branch of the S-shaped curve. This is a consistent formulation if it is used in a steady state calculation of a fully ignited flame. However, this assumption is no longer valid in unsteady descriptions of non-premixed flames as there can be transient states. In order to extend the SLFM to include all three solution branches on the S-shaped curve, Pierce & Moin (2004) have proposed the Flamelet/Progress Variable (FPV) model. In this model, a reaction progress parameter Λ is introduced to replace $\chi_{Z,st}$ so that every single flamelet solutions along the S-shaped curve can uniquely be parameterized. This model also requires the reaction progress parameter

to be statistically independent of the mixture fraction in the context of turbulent reacting flow. This additional constraint allows for model simplification in turbulent combustion.

The reaction progress parameter is usually the evaluation of a reaction progress variable C at the stoichiometric mixture fraction, i.e.

$$\Lambda = C|Z_{st}. \tag{2.26}$$

The reaction progress variable C needs to represent the progress of combustion. Thus, the temperature or a linear combination of the mass fractions of major reaction products are possible candidates of C. With this condition, the thermo-chemical structure of a flamelet can be written in the form of

$$\boldsymbol{\psi} = \mathcal{F}_{FPV,\boldsymbol{\psi}}\left(Z,\Lambda\right). \tag{2.27}$$

Despite the similarity with SLFM, this mapping differs from Eq. (2.25) by encompassing all solutions of the steady state flamelet equations. Since C can be a linear combination of the thermo-chemical variables (Ihme *et al.*, 2012), it can also be described using Eq. (2.27), *i.e.*

$$C = \mathcal{F}_{FPV,C}\left(Z,\Lambda\right). \tag{2.28}$$

In order to employ the mapping in Eq. (2.27), Λ needs to be evaluated in calculations. However, this is not done in practice because the transport equation of Λ can present additional modeling challenges (Ihme, 2007). Instead, the common approach is to use C to parameterize the flamelet library. In this method, the state relation is written as

$$\boldsymbol{\psi} = \mathcal{G}_{FPV,\boldsymbol{\psi}}\left(Z,C\right), \tag{2.29}$$

where $\mathcal{G}_{FPV,\boldsymbol{\psi}}\left(Z,C\right) = \mathcal{F}_{FPV,\boldsymbol{\psi}}\left(Z,\mathcal{F}_{C}^{-1}\left(Z,C\right)\right)$. This formulation is consistent with Eq. (2.27) if $\mathcal{F}_{FPV,C}$ is a bijective mapping of Λ to C.

Although the FPV model is based on the steady flamelet solution, Pierce (2001) at-

tempted to analyze the model behavior in an unsteady framework. To end this, Pierce (2001) has assumed that flamelets utilized in the FPV model and in the unsteady flamelets share the same flame structure at the same Λ. Since the FPV model is not explicitly dependent on the scalar dissipation rate, an effective scalar dissipation rate was defined in Pierce's analysis. Under these assumptions, this anlysis shows the relaxation of the FPV model to the steady flamelet solutions. In this manner, the FPV model is similar to the equivalent strain rate formulation developed by Cuenot *et al.* (2000).

In a later work by Ihme (2007), the interpretation of the FPV model is reexamined without the equal flame structure assumption. This assumption is relaxed because an comparisons of the unsteady flamelet solutions with the steady flamelet solutions revealed that they do not have the same flame structure at the same Λ. Due to this discrepancy, the FPV model was decomposed into as small deviation from the steady flamelet solution. Using this description of the FPV model in an asymptotic analysis, Ihme (2007) was able to recover the relaxation terms suggested by Pierce (2001). However, additional terms were also found in this analysis.

When the FPV model was first introduced, the choice of the reaction progress variable C was somewhat arbitrary as there can be numerous possible variables that satisfy the criteria for C. For the methane-air combustion, Pierce (2001) has suggested $C = Y_{CO_2} + Y_{H_2O} + Y_{CO} + Y_{H_2}$ which can provide a unique mapping of states over the whole mixture fraction space. To alleviate the ambiguity of reaction progress variable, Ihme *et al.* (2012) has formulated the selection of C as an optimization problem. By using the monotonicity C on the Λ space as the cost function, Ihme *et al.* (2012) found a more optimal choice C for methane-air chemistry. However, the improvement over the reaction progress variable suggested by Pierce (2001) is marginal. Therefore, $C = Y_{CO_2} + Y_{H_2O} + Y_{CO} + Y_{H_2}$ is used throughout this study.

2.2.2 Premixed Flamelet Model

Unlike non-premixed flames, premixed flames burn in homogeneous mixtures of fuel and oxidizer. In this configuration, flames can propagate through the flammable mixture leaving burnt products in the wake. The speed by which a premixed flame can propagate in a quiescent environment is referred to as the laminar flame speed, S_L. The theoretical analysis on premixed flames by Mallard & Le Chatelier (1883) has shown that the laminar flame speed is proportional to thermal diffusivity and reaction rates. For a more accurate determination of the flame speed, numerical codes can be employed to solve for the detailed flame structure of a 1D freely propagating premixed flame. The burning velocity of this 1D premixed flame is simply the mass flow rate of the reactant divided its density. In addition, the thermal thickness of this 1D flame can be defined as

$$\Delta l_f = \frac{T_{max} - T_{min}}{\left(\frac{\partial T}{\partial x}\right)_{max}}. \tag{2.30}$$

The 1D freely propagating premixed flame is also used as the basis of several premixed flamelet models. The Flamelet-Generated Manifold (FGM) (Oijen & Goey, 2000) and Flamelet Prolongation ILDM (FPI) (Gicquel *et al.*, 2000) models are two similar premixed flamelet models that utilize this modeling approach. In essence, both of these methods employ manifold representations of the 1D premixed flamelets. Since there is no variation of the mixture fraction in a premixed flamelet so the premixed flamelet manifold is parameterized in terms of the progress variable i.e.

$$\boldsymbol{\psi} = \mathcal{G}_{FGM,\boldsymbol{\psi}}\left(C\right), \tag{2.31}$$

The FPI model utilizes combustion products as the progress variable whereas the FGM model utilizes the enthalpy as an indication of reaction progress. Both models are shown to be able to reduce the stiffness of chemistry while retaining the flame structure spanned

by complex chemistry. This property can be observed when applying the FGM model back to simulations of 1D freely propagating premixed flames (Oijen & Goey, 2000).

The FGM/FPI model has been extended to simulations of partially premixed flames. This is achieved by introducing the mixture fraction as another independent parameterization in the manifold. The mixture fraction dimension can be populated with 1D premixed flame solutions at different equivalence ratios. For the mixture fraction values outside of the flammability limit of premixed flames, thermo-chemical properties are usually linearly interpolated using the premixed flamelet solution at the flammability limit and the unburnt mixture properties at $Z = 0$ or $Z = 1$. After the extension of the premixed flamelet manifold, the mapping of thermo-chemical variables becomes

$$\boldsymbol{\psi} = \mathcal{G}_{FGM,\boldsymbol{\psi}}\left(Z, C\right), \tag{2.32}$$

which shares the same form as the FPV model in Eq. (2.29). This extension of the FGM and FPI models has been utilized by Bongers *et al.* (2005) and Fiorina *et al.* (2005) in partially premixed and non-premixed counter-flow flames. In application to partially premixed counter-flow flames, the FGM/FPI method is shown to be able to reproduce detailed chemistry results with reasonable accuracy for a large range of strain rates. However, these models show considerable discrepancies in highly strained diffusion counter-flow flames.

2.3 Working Equations

After employing the flamelet models and the simplifications highlighted in Sec. (2.1.1), the transport equations can be written as

$$\frac{\partial \rho}{\partial t} + \nabla \cdot (\rho \boldsymbol{u}) = 0 \tag{2.33a}$$

$$\frac{\partial (\rho \boldsymbol{u})}{\partial t} + \nabla \cdot (\rho \boldsymbol{u} \otimes \boldsymbol{u}) = -\nabla p + \nabla \cdot \left[\mu \left(\nabla \boldsymbol{u} + (\nabla \boldsymbol{u})^T \right) + \frac{2}{3} \mu \nabla \boldsymbol{u} \cdot \underline{\underline{I}} \right] + \rho \boldsymbol{g} \tag{2.33b}$$

$$\frac{\partial (\rho Z)}{\partial t} + \nabla \cdot (\rho \boldsymbol{u} Z) = \nabla \cdot (\rho \upsilon \nabla Z) \tag{2.33c}$$

$$\frac{\partial (\rho C)}{\partial t} + \nabla \cdot (\rho \boldsymbol{u} C) = \nabla \cdot (\rho \upsilon \nabla (C)) + \dot{\omega}_C \tag{2.33d}$$

$$\boldsymbol{\phi_c} = \mathcal{G}_{\boldsymbol{\phi_c}} (Z, C) . \tag{2.33e}$$

where $\boldsymbol{\phi_c}$ is $\left[\rho, \mu, \upsilon, T, \boldsymbol{Y}^T\right]^T$. $\mathcal{G}_{\boldsymbol{\phi_c}} (Z, C)$ is constructed in the same manner as $\mathcal{G}_{\boldsymbol{\psi}} (Z, C)$ but with different set of output variables. Note that the transport equation of energy is excluded here due to the "low Mach number approximation" and hence only the hydrodynamic pressure can be solved for using Eq. (2.33).

2.4 Decomposition of Variables

In both the linear stability analysis and LES, the state variable $\boldsymbol{\phi}$ is decomposed into

$$\boldsymbol{\phi}(t, \boldsymbol{x}) = \overline{\boldsymbol{\phi}}(t, \boldsymbol{x}) + \boldsymbol{\phi}'(t, \boldsymbol{x}), \tag{2.34}$$

where $\boldsymbol{\phi}'(t, \boldsymbol{x})$ is the residual component. The actual definition of $\overline{\boldsymbol{\phi}}$ depends on the methods in which this decomposition is applied to. Nevertheless, $\overline{\boldsymbol{\phi}}$ can generally be expressed as

$$\overline{\boldsymbol{\phi}(t, \boldsymbol{x})} = \int_{t_0}^{t_1} \int J(\tau, t, \boldsymbol{y}, \boldsymbol{x}) \boldsymbol{\phi}(\tau, \boldsymbol{y}) d\boldsymbol{y} d\tau, \tag{2.35}$$

where J is a general function that is dependent on the context of the application.

In linear stability analysis, $\overline{\phi}$ represents the base flow solutions while ϕ' represents perturbations from the base flow. The base flow solution, by definition, is the steady state solution to Eq. (2.33) but it may not be attainable for most flow conditions. In these scenarios, the temporal mean of the unsteady solution is usually used as the base flow instead. In an analysis of the flows behind a cylinder, Sipp & Lebedev (2007) have found that analyses based on the mean flow show better agreement with experimental results. Following the form of Eq. (2.35), $J(t, \boldsymbol{y})$ for the temporal mean can be defined as

$$J(\tau, t, \boldsymbol{y}, \boldsymbol{x}) = \delta(\boldsymbol{x} - \boldsymbol{y}) \frac{1}{t_1 - t_0}. \tag{2.36}$$

The principle of LES is to only resolve the large scale turbulence and model the unresolved scales. To this end, the governing equations (2.33) are spatially filtered at a certain filter width Δ. In non-reacting flow, the filtering procedure on the state variable $\boldsymbol{\phi}$ is

$$\overline{\boldsymbol{\phi}}\,(t, \boldsymbol{x}) = \int_{t_0}^{t_1} \int \boldsymbol{\phi}\,(t, \boldsymbol{y})\, G\,(\boldsymbol{y}, \boldsymbol{x}; \Delta)\, \delta(t - \tau) d\boldsymbol{y} d\tau \ , \tag{2.37}$$

where G needs to be normalized such that

$$\int G\,(\boldsymbol{y}, \boldsymbol{x}; \Delta)\, d\boldsymbol{y} = 1 \quad \forall\ \boldsymbol{x} \ . \tag{2.38}$$

Therefore, $J(t, \boldsymbol{y})$ in the LES filtering procedure is

$$J(\tau, t, \boldsymbol{y}, \boldsymbol{x}) = G\,(\boldsymbol{y}, \boldsymbol{x}; \Delta)\, \delta(t - \tau) \ . \tag{2.39}$$

Although the linear stability analysis and LES approaches share the similar form of variable decomposition, the property of the residual variable is not the same. For example, operation of Eq. (2.35) applied to temporal fluctuations yield zeros while the filtering procedure applied to the residuals of filtered variables does not always lead to zero values.

Due to the variation of density in reacting flows, it is more convenient to employ the decomposition through density weighting, i.e.

$$\overline{\boldsymbol{\phi}(t,\boldsymbol{x})} = \int_{t_0}^{t_1} \int \overline{\rho}(t,\boldsymbol{y}) J(t,\boldsymbol{y}) \boldsymbol{\phi}(t,\boldsymbol{y}) d\boldsymbol{y} d\tau. \tag{2.40}$$

Nevertheless, the unweighted decomposition (Reynolds decomposition) is still applied to volume specific variables such as ρ and p in the reacting flow. This Favre weighted procedure is related to Reynolds decomposition as

$$\widetilde{\boldsymbol{\phi}} = \frac{\widetilde{\rho\boldsymbol{\phi}}}{\overline{\rho}}. \tag{2.41}$$

After the Favre decomposition, variable $\boldsymbol{\phi}$ is expressed as

$$\boldsymbol{\phi} = \widetilde{\boldsymbol{\phi}} + \boldsymbol{\phi}'', \tag{2.42}$$

where $\boldsymbol{\phi}''$ is residual component of $\boldsymbol{\phi}$.

2.4.1 Linearized Equations

In order to obtain the linearized equations, the flamelet mapping in Eq. (2.33e) is linearized as

$$\mathcal{G}_{\boldsymbol{\phi_c}}(Z,C) \approx \mathcal{G}_{\boldsymbol{\phi_c}}\left(\widetilde{Z},\widetilde{C}\right) + \partial_Z \mathcal{G}_{\boldsymbol{\phi_c}}|_{\boldsymbol{Z},\boldsymbol{C}}\, Z'' + \partial_C \mathcal{G}_{\boldsymbol{\phi_c}}|_{\boldsymbol{Z},\boldsymbol{C}}\, C'' \tag{2.43}$$

Since a buoyant diffusion flame is considered in the application of linear analysis analysis in this work, the non-premixed flamelet manifold $\mathcal{G}_{FPV}$ is implied in the following discussion of linear stability analysis within Chap 3.

Substituting Eqs. (2.35), (2.43) into Eq. (2.33) and neglecting higher order terms, yields

$$\frac{\partial \rho''}{\partial t} + \nabla \cdot (\rho'' \widetilde{\boldsymbol{u}}) + \nabla \cdot (\widetilde{\rho} \boldsymbol{u}'') = 0 \ , \tag{2.44a}$$

$$\frac{\partial \left(\widetilde{\rho} \boldsymbol{u}'' + \rho'' \widetilde{\boldsymbol{u}}\right)}{\partial t} + \nabla \left(\widetilde{\rho} \widetilde{\boldsymbol{u}} \otimes \boldsymbol{u}'' + \left[\widetilde{\rho} \boldsymbol{u}'' + \rho'' \widetilde{\boldsymbol{u}}\right] \otimes \widetilde{\boldsymbol{u}}\right) = -\nabla p'' + \nabla \cdot \underline{\underline{\tau}}'' + \rho'' \ , \tag{2.44b}$$

$$\frac{\partial \left(\widetilde{\rho} Z'' + \rho'' \widetilde{Z}\right)}{\partial t} + \nabla \left(\widetilde{\rho} \widetilde{\boldsymbol{u}} Z'' + \left[\widetilde{\rho} \boldsymbol{u}'' + \rho'' \widetilde{\boldsymbol{u}}\right] \widetilde{Z}\right) = \nabla \cdot \left(\widetilde{\upsilon} \nabla Z'' + \upsilon'' \widetilde{Z}\right) \ , \tag{2.44c}$$

$$\frac{\partial \left(\widetilde{\rho} C'' + \rho'' \widetilde{C}\right)}{\partial t} + \nabla \left(\widetilde{\rho} \widetilde{\boldsymbol{u}} C'' + \left[\widetilde{\rho} \boldsymbol{u}'' + \rho'' \widetilde{\boldsymbol{u}}\right] \widetilde{C}\right) = \nabla \cdot \left(\widetilde{\upsilon} \nabla C'' + \upsilon'' \widetilde{C}\right) + \dot{\omega}_C'' \ , \tag{2.44d}$$

with:

$$\underline{\underline{\tau}}'' = \mu'' \left(\nabla \widetilde{\boldsymbol{u}} + (\nabla \widetilde{\boldsymbol{u}})^T + \frac{2}{3} \nabla \widetilde{\boldsymbol{u}} \cdot \underline{\underline{I}}\right) + \widetilde{\mu} \left(\nabla \boldsymbol{u}'' + (\nabla \boldsymbol{u}'')^T + \frac{2}{3} \nabla \boldsymbol{u}'' \cdot \underline{\underline{I}}\right) \ , \tag{2.44e}$$

$$\boldsymbol{\phi}_c'' = \partial_Z \mathcal{G}_{\boldsymbol{\phi_c}} \left(\widetilde{Z}, \widetilde{C}\right) Z'' + \partial_C \mathcal{G}_{\boldsymbol{\phi_c}} \left(\widetilde{Z}, \widetilde{C}\right) C'' \ . \tag{2.44f}$$

2.4.2 Filtered Equations

Assuming that G is selected such that the filtering procedure commutes with respect to spatial derivatives, the filtering of Eq. (2.33) yields

$$\frac{\partial \bar{\rho}}{\partial t} + \nabla \cdot (\bar{\rho} \widetilde{\boldsymbol{u}}) = 0 \tag{2.45a}$$

$$\frac{\partial \left(\bar{\rho} \widetilde{\boldsymbol{u}}\right)}{\partial t} + \nabla \cdot \left(\bar{\rho} \widetilde{\boldsymbol{u}} \otimes \widetilde{\boldsymbol{u}}\right) = -\nabla \bar{p} + \nabla \cdot \left[\widetilde{\mu} \left(\nabla \widetilde{\boldsymbol{u}} + (\nabla \widetilde{\boldsymbol{u}})^T\right) + \frac{2}{3} \widetilde{\mu} \nabla \widetilde{\boldsymbol{u}} \cdot \underline{\underline{I}}\right] + \nabla \cdot \overline{\underline{\underline{\sigma}}}^{res} + \bar{\rho} \boldsymbol{g} \tag{2.45b}$$

$$\frac{\partial \left(\bar{\rho} \widetilde{Z}\right)}{\partial t} + \nabla \cdot \left(\bar{\rho} \widetilde{\boldsymbol{u}} \widetilde{Z}\right) = \nabla \cdot \left(\bar{\rho} \widetilde{\upsilon} \nabla \widetilde{Z}\right) + \nabla \cdot \overline{\boldsymbol{\tau}}_Z^{res} \tag{2.45c}$$

$$\frac{\partial \left(\bar{\rho} \widetilde{C}\right)}{\partial t} + \nabla \cdot \left(\bar{\rho} \widetilde{\boldsymbol{u}} \widetilde{C}\right) = \nabla \cdot \left(\bar{\rho} \widetilde{\upsilon} \nabla \widetilde{C}\right) + \nabla \cdot \overline{\boldsymbol{\tau}}_C^{res} + \widetilde{\dot{\omega}_C} \tag{2.45d}$$

where

$$\overline{\underline{\underline{\sigma}}}^{res} = \bar{\rho}\widetilde{\boldsymbol{u}}\widetilde{\boldsymbol{u}} - \bar{\rho}\widetilde{\boldsymbol{u}\boldsymbol{u}}, \tag{2.46}$$

$$\overline{\boldsymbol{\tau}}_{\phi}^{res} = \bar{\rho}\widetilde{\boldsymbol{u}}\tilde{\phi} - \bar{\rho}\widetilde{\boldsymbol{u}\phi}. \tag{2.47}$$

The flamelet model is not explicitly shown in Eq. (2.45) as it may require higher order statistical moments of $\widetilde{Z}$ and $\widetilde{C}$ and this is discussed in Sec. 4.1.2. Besides that, the unresolved stresses $\overline{\underline{\underline{\sigma}}}^{res}$ and the scalar fluxes $\overline{\boldsymbol{\tau}}_{\phi}^{res}$ are also unclosed terms that need to be modeled.

Although the filtering procedure is essential in uncovering the sub-grid scale terms, this filtering procedure is usually not performed explicitly in most applications of the LES method. Since most LES computations employ grids of finite resolutions, the discretization schemes applied on a grid can implicitly filter out any turbulent structures smaller than the mesh size. This LES approach is more common due to its simplicity but it introduces grid-dependent properties to the turbulence models. Explicitly filtering the LES solution can alleviate this issue of grid dependence (Ghosal & Moin, 1995) but it is usually not done in practice.

CHAPTER 3

Low Order Method and Linear Stability Analysis

Linear stability analysis is a lower order method that is usually employed in investigations of the hydrodynamic instability. In this chapter, the methodology of utilizing linear stability analysis in reacting flow is discussed. Specifically, detailed chemistry effects are introduced to this methodology through the utilization of flamelet model. This analysis approach is applied a buoyant diffusion jet flame and this chapter finishes discussion of the results.

3.1 Methodology

3.1.1 Local Parallel Flow Assumption

The linearized equations, shown in Sec.2.4.1, need to be solved in order to describe the hydrodynamics of a flow. Without further algebraic treatment, an initial condition is required for the solution of Eq. (2.44). However, solving Eq. (2.44) for arbitrary initial conditions is generally inefficient as an exhaustive search for unstable modes can be very expensive. To make linear stability analysis more tractable, the flow symmetry and scale separation may be used to simplify the equations.

In this work , we will consider a jet flame. For this configuration, the locally parallel flow assumption (Schmid & Henningson, 2001) is invoked here. In this assumption, the

radial velocity of the base flow is neglected. Due to the restriction imposed by the continuity equation, the mean axial velocity then becomes independent of axial location. This is a reasonable assumption as long as any spatially evolving instabilities are faster than the slow spreading of a jet flame over axial distance.

In addition to the parallel flow assumption, the jet flame is assumed to be axisymmetric. Under this assumption, the flow is invariant under rotation along the center axis so that the base flow is not dependent on the tangential direction. Although asymmetric instability may be present in the jet flame, the base flow is expected to be largely axisymmetric as there is no persistent swirl being imparted to the jet flame.

3.1.2 Modal Expansion

In linear stability analysis, a small perturbation $\boldsymbol{\phi}''$ is usually solved in the frequency space as

$$\boldsymbol{\phi}''(\boldsymbol{x}, t) = \breve{\boldsymbol{\phi}}(\boldsymbol{x}) \exp(i\omega t), \tag{3.1}$$

where ω is the complex frequency. If this form of perturbation is directly substituted into Eq. (2.44) and solved for, this method is referred to as the global instability analysis (Theofilis, 2011). Due to improvements in numerical algorithms and computer hardware, this method sees increasing applications in complex flow configurations that are not accessible to the parallel flow assumption. However, this approach is not attempted here because of the simplicity of jet flame.

For the slowly varying and symmetric spatial directions, Fourier transform is employed to achieve a modal decomposition of $\boldsymbol{\phi}''$. After applying the spatial and temporal transformations, the fluctuating component of the state variables is

$$\boldsymbol{\phi}''(\boldsymbol{x}, t) = \hat{\boldsymbol{\phi}}(r) \exp(i\alpha x + im\theta - i\omega t), \tag{3.2}$$

for a specific instability mode. While α can be complex, m is always an integer due to the

axisymmetric nature of a jet flow.

3.1.3 Equations in Cylindrical Coordinate System

To solve the linearized equations in Sec. 2.4.1, a coordinate system has to be first defined. Since a jet flame is considered here, the cylindrical coordinate system appears to be a natural choice for the following analysis. After the parallel flow assumption and modal expansion, the equations in cylindrical coordinates are

$$-i\omega\hat{\rho} + i\alpha\left(\rho\hat{u} + \tilde{u}\hat{\rho}\right) + \frac{1}{r}\frac{d}{dr}\left(r\bar{\rho}\hat{v}\right) + \frac{im\bar{\rho}}{r}\hat{w} = 0, \tag{3.3a}$$

$$\begin{aligned} -i\omega\bar{\rho}\hat{u} + i\alpha\tilde{\rho}\tilde{u}\hat{u} + \bar{\rho}\frac{d\tilde{u}}{dr}\hat{v} + i\alpha\hat{p} - \hat{\rho}g = \frac{1}{r}\frac{d}{dr}\left(\tilde{\mu}r\frac{d\hat{u}}{dr} + \hat{\mu}r\frac{d\tilde{u}}{dr}\right) \\ +\tilde{\mu}\left(\frac{4i\alpha}{3}\hat{u} - \frac{m}{3r}\alpha\hat{w} - \frac{m^2}{r^2}\hat{u}\right) + \frac{1}{3}\frac{i\alpha}{r}\frac{d}{dr}\left(\tilde{u}r\hat{v}\right), \end{aligned} \tag{3.3b}$$

$$\begin{aligned} -i\omega\bar{\rho}\hat{v} + i\alpha\bar{\rho}\tilde{u}\hat{v} + \frac{d\hat{p}}{dr} = \frac{i\alpha}{3}\left(\tilde{\mu}\frac{d\hat{u}}{dr} - 2\frac{d\tilde{\mu}}{dr}\hat{u}\right) - \left(\frac{m^2\tilde{\mu}}{r^2} + \frac{2}{3r}\frac{d\tilde{\mu}}{dr} + \tilde{\mu}\alpha^2\right)\hat{v} \\ -\frac{4}{3}\left[\frac{d}{dr}\left(\tilde{\mu}\frac{d\hat{v}}{dr}\right) - \frac{\tilde{\mu}}{r^2}\frac{dr\hat{v}}{dr}\right] - \frac{i2m}{3r}\left(\frac{d\tilde{\mu}}{dr} + \frac{\tilde{\mu}}{2}\left[\frac{7}{r} - \frac{d}{dr}\right]\right)\hat{w} + i\alpha\frac{d\tilde{u}}{dr}\hat{u}, \end{aligned} \tag{3.3c}$$

$$\begin{aligned} -i\omega\bar{\rho}\hat{w} + i\alpha\bar{\rho}\tilde{u}\hat{w} + i\frac{m}{r}p = -\frac{m\alpha\tilde{\mu}}{3r}\hat{u} + \frac{i\,m}{r}\left(\frac{\tilde{\mu}}{3r}\frac{d}{dr}\left(r\hat{v}\right) - \frac{d\mu}{dr}\hat{v}\right) \\ +\tilde{\mu}\left(\frac{1}{r}\frac{d}{dr}\left(r\frac{d\hat{w}}{dr}\right) - \frac{\hat{w}}{r^2} - \frac{4m^2}{3r^2}\hat{w} - \alpha^2\hat{w}\right) + \frac{d\tilde{\mu}}{dr}\left(\frac{d}{dr} - \frac{1}{r}\right)\hat{w}, \end{aligned} \tag{3.3d}$$

$$\begin{aligned} -i\omega\bar{\rho}\hat{Z} + i\alpha\bar{\rho}\tilde{u}\hat{Z} + \bar{\rho}\frac{d\tilde{Z}}{dr}\hat{u} =& \frac{d}{dr}\left(r\tilde{v}\frac{d\hat{Z}}{dr} + r\hat{v}\frac{d\tilde{Z}}{dr}\right) \\ &- \tilde{v}\left(\frac{m^2}{r^2} - \alpha^2\right)\hat{Z}, \end{aligned} \tag{3.3e}$$

$$\begin{aligned} -i\omega\bar{\rho}\hat{C} + i\alpha\bar{\rho}\tilde{u}\hat{C} + \bar{\rho}\frac{d\tilde{C}}{dr}\hat{u} =& \frac{d}{dr}\left(r\tilde{v}\frac{d\hat{C}}{dr} + r\hat{v}\frac{d\tilde{C}}{dr}\right) \\ &- \tilde{v}\left(\frac{m^2}{r^2} - \alpha^2\right)\hat{C} + \widehat{\dot{\omega}_C}. \end{aligned} \tag{3.3f}$$

At the boundary, Eq. (3.3) is subjected to the following boundary conditions for the $m = 0$ azimuthal mode:

$$r = 0: \quad \frac{d\widehat{u}}{dr} = 0\,, \quad \widehat{v} = 0\,, \quad \widehat{w} = 0\,, \quad \frac{d\widehat{p}}{dr} = 0\,, \quad \frac{d\widehat{Z}}{dr} = 0\,, \quad \frac{d\widehat{C}}{dr} = 0\,, \tag{3.4}$$

$$r \to \infty: \quad \widehat{u} \to 0\,, \quad \widehat{v} \to 0\,, \quad \widehat{w} \to 0\,, \quad \widehat{p} \to 0\,, \quad \widehat{Z} \to 0\,, \quad \widehat{C} \to 0 \tag{3.5}$$

3.1.4 Dispersion Relation

If Eq. (3.3) is solved as an eigenvalue problem, either ω or α has to be prescribed. Regardless of the choice of the independent variable, this implicit relation between ω and α is commonly referred to as the dispersion relation:

$$D\left(\alpha, \omega\right) = 0. \tag{3.6}$$

In a temporal linear stability analysis, ω is solved as a function of real wavenumber to examine the response of a flow to perturbations of a certain wavelength. In an open jet flow, it is more natural to consider flow instabilities that can be excited by an upstream perturbation of certain frequency. Therefore, spatial linear stability analysis is performed here for a buoyant non-premixed jet flame. To formulate Eq. (3.3) for spatial analysis, a real ω is prescribed and α becomes the eigenvalue that needs to be computed. In matrix form, the generalized eigenvalue problem of the spatial analysis is

$$\boldsymbol{A}_{\alpha}\left(\omega\right)\hat{\boldsymbol{\phi}} = \alpha \boldsymbol{B}_{\alpha}\left(\omega\right)\hat{\boldsymbol{\phi}}. \tag{3.7}$$

3.1.5 Absolute and Convective Instability

The spatial instability modes that are elucidated through linear stability analysis may not always be present in a flow. Some instabilities require persistent external excitations to their presence in the flow. However, there are instabilities that are self-sustaining and would

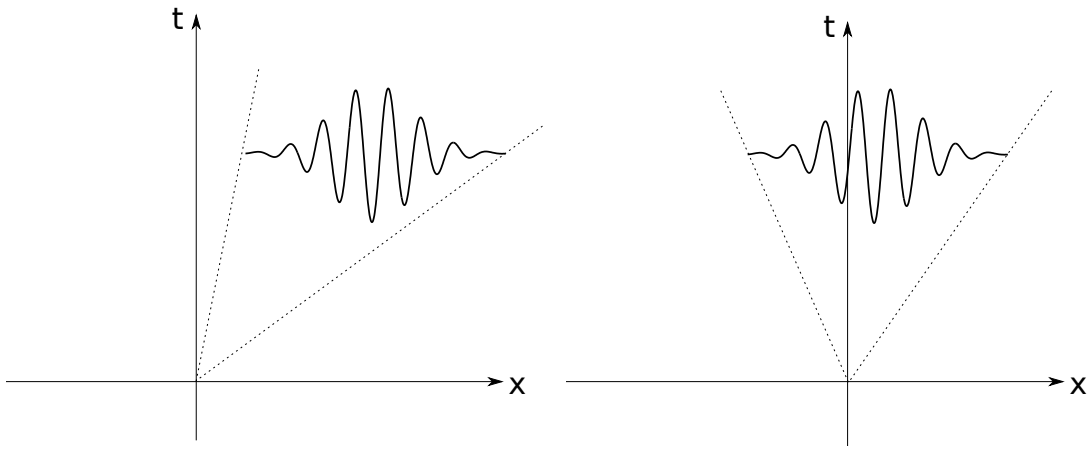

(a) Illustration of a convective instability on the $x-t$-plane.

(b) Illustration of an absolute instability on the $x-t$-plane.

Figure 3.1: Depiction of convective and absolute instability; (a) a convective instability propagates toward the downstream direction; (b) an absolute instability propagates toward both downstream and upstream directions (Adapted from Huerre & Monkewitz (1990)).

not be convected out of the flow region of interest (Huerre & Monkewitz, 1990). These characteristics of flow instabilities can be understood by considering the response of a flow to an impulse forcing. Suppose a steady base flow is initially forced with an impulse, flow disturbances will be generated as a response. If the generated perturbations grow while propagating both upstream and downstream of the impulse, the flow is categorized as absolutely unstable. On the other hand, the flow is considered convectively unstable if the amplified disturbances are only convected downstream. These two types of flow response to an impulse forcing are depicted in the $x-t$-plane in Fig. 3.1.

3.1.5.1 Mathematical Definitions

The response of the linearized flow to an impulse forcing is given by the Green's function $G(x,t)$ which satisfies:

$$D\left(-i\frac{\partial}{\partial x}, i\frac{\partial}{\partial t}\right) G(x,t) = \delta(x)\,\delta(t) \ , \tag{3.8}$$

where D is the dispersion relation in physical space. The base flow is linearly stable if

$$\lim_{t\to\infty} G(x,t) = 0 \quad \forall \quad \frac{x}{t} = \text{constant} \,. \tag{3.9}$$

Otherwise, the base flow is linearly unstable as

$$\exists \, \frac{x}{t} = \text{constant} \quad : \lim_{t\to\infty} G(x,t) \to \infty \,. \tag{3.10}$$

The linearly unstable flows can further be classified as convectively unstable if

$$\lim_{t\to\infty} G(x,t) = 0 \quad \text{for } \frac{x}{t} = 0 \,, \tag{3.11}$$

or absolutely unstable if

$$\lim_{t\to\infty} G(x,t) \to \infty \quad \text{for } \frac{x}{t} = 0 \,. \tag{3.12}$$

Briggs' method (Briggs, 1964) is commonly utilized to evaluate the time-asymptotic behavior of Green's function and this method is discussed next.

3.1.5.2 Briggs' Method

To solve for Green's function in Eq. (3.8), a spatial fourier transformation is applied to the equation and then followed by a temporal Laplace transformation. These steps yield a Green's function in the (α, ω) space and the physical description of Green's function can recovered by integrating it along inversion contours in α and ω spaces, respectively:

$$G(x,t) = \frac{1}{4\pi^2} \int_L \int_F \frac{\exp(i\alpha x - \omega t)}{D(\alpha,\omega)} d\alpha d\omega. \tag{3.13}$$

Note that L and F denote the inversion contour in Laplace-transformed space, ω and Fourier-transformed space, α, respectively. The Briggs' method can be employed to eval-

uate the time-asymptotic behavior of the Green function in the form of Eq. (3.13) so the base flow can be classified under the definitions in Sec. 3.1.5.1.

Briggs' method is based on finding a discrete singularity ω_0 in the ω space by slowly lowering the L-contour from a sufficiently large $\mathrm{Im}(\omega)$. This is done because the singularity can determine the time-asymptote of the Green function. If $\mathrm{Im}(\omega_0) < 0$ then the temporal inversion contour results in an integral that vanishes as $t \to \infty$, indicating a convectively unstable flow. Otherwise, a careful examination of the spatial inversion contour in the α-plane is required to determine if the instability is absolute.

For the spatial inversion contour F, the real α axis is considered initially. By causality, the mapping of F through the dispersion relation $\omega(F)$ has to lie below the starting L-contour in the ω-plane. Conversely, the L-contour can also be mapped back to the α-plane as $\alpha(L)$. For an absolute instability, this mapping is usually multi-valued so there exists a singularity that can impede the lowering of the temporal inversion contour. Specifically, there needs to be two branches of mapping $\alpha^+(L)$ and $\alpha^-(L)$ which are located above and below real α-axis respectively. As a result, the $\alpha^+(L)$ solution branch governs the downstream dynamics while the $\alpha^-(L)$ solution branch corresponds to the upstream behavior. If these two branches approach the singularity when the L-contour is being lowered, the spatial inversion contour will eventually be pinched by the branches. This prevents any further lowering of the temporal inversion contour without crossing a branch point ω_0 in the ω space. Under these conditions, the asymptotic behavior of Eq. (3.13) is governed by the corresponding pinch point α_0 in the α space. This procedure of contour deformation is illustrated in Fig. 3.2.

Since the pinch point α_0 is a special case of a saddle point, it satisfies the relations

$$D\left(\alpha_0, \omega_0\right) = 0 \quad , \quad \frac{\partial D}{\partial \alpha}\left(\alpha_0, \omega_0\right) = 0 \quad , \quad \frac{\partial^2 D}{\partial \alpha^2}\left(\alpha_0, \omega_0\right) \neq 0. \tag{3.14}$$

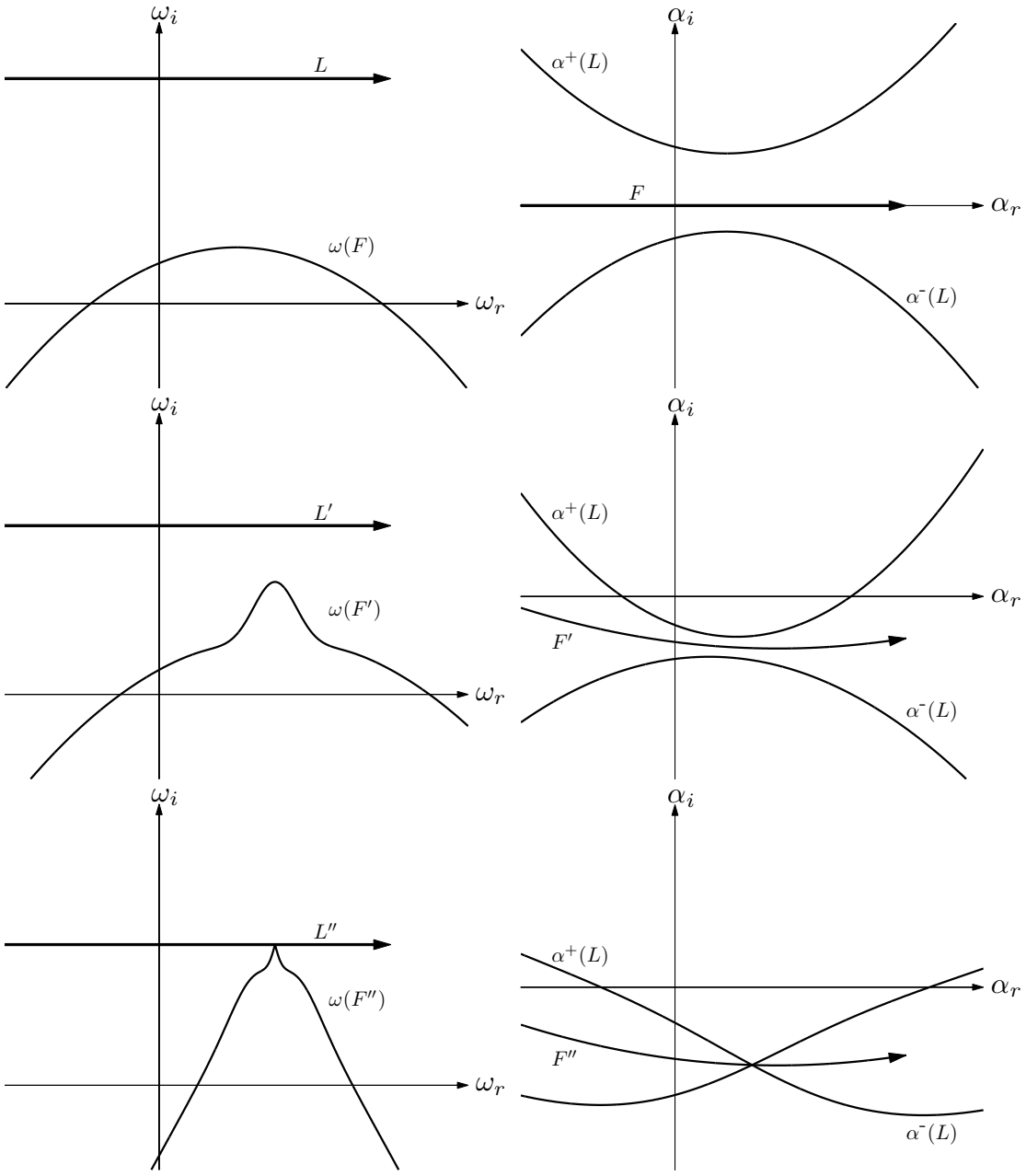

Figure 3.2: Depiction of contour deformation toward a saddle point singularity on the ω-plane (left) and the α-plane (right) (Adapted from Schmid & Henningson (2001)).

Assuming $\frac{\partial D}{\partial \omega}(\alpha_0, \omega_0) \neq 0$, then

$$C_g = \frac{\partial \omega}{\partial \alpha} = \frac{\partial D}{\partial \alpha} \Big/ \frac{\partial D}{\partial \omega} = 0, \tag{3.15}$$

thus satisfying the zero group velocity criterion of Eq. (3.12).

3.1.6 Solution Method

3.1.6.1 Spatial Analysis

For more realistic base flows, an analytical solution of Eq. (3.3) is generally intractable. Thus, numerical procedures are usually employed to solve the associated eigenvalue problem. One of the algorithms that is commonly used in linear stability analysis is the shooting method (Schmid & Henningson, 2001). This iterative solution method starts with an initial guess for the eigenvalue, then Eq. (3.3) is integrated along the radial direction to recover a corresponding solution vector. This initial guess solution is not likely to be close to the actual solution as the boundary conditions are usually not satisfied at this stage. To iteratively obtain a better approximation of the eigenvalue, a root-finding algorithm is employed to drive the error at the boundary to a allowable small tolerance. Owing to its simplicity, this approach can be both computationally efficient and easily implemented. However, the shooting method is a local method as it can only search for one eigenvalue at a time.

To consider the entire spectra, this work utilizes a global solution method. In most global methods, the non-modal space is directly discretized, resulting in a pair of matrices that are solvable with conventional numerical eigenvalue solvers. This work employs the method by Schmid & Henningson (2001) where the radial direction is discretized using Chebyshev polynomials on collocation points in a mapped computational space. To this end, the solution $\hat{\boldsymbol{\phi}}$ is represented as

$$\hat{\boldsymbol{\phi}}(r) = \sum_{i}^{N} \boldsymbol{a}_i T_i(\xi(r)); \quad \xi \in [-1, 1] \tag{3.16}$$

where T_i is the ith Chebyshev polynomial. The mapping of a semi-infinite domain to a finite domain,

$$r(\xi) = \frac{1+\xi}{1-\xi} \tag{3.17}$$

is used here for the radial direction. The collocation points are the Chebyshev-Gauss-Lobatto points, which are given as:

$$\xi_k = \cos\left(\frac{k\pi}{N}\right); \quad k = 0, 1..., N. \tag{3.18}$$

At these points, the Chebyshev polynomials and their derivatives are evaluated using recurrence relations so that $\boldsymbol{a}_i$ can be solved as unknowns to reconstruct $\widehat{\phi}$. Substituting this representation of $\hat{\phi}$ into Eq. (3.3) and collecting α yield the discrete variant of the eigenvalue problem. In addition, the boundary conditions described in Sec. 3.1.3 are enforced at the first and last collocation points.

In order to qualify the method as global, all the eigenvalues for the discrete matrices need to be computed. The QZ decomposition is a direct method for solving generalized eigenvalue problems and it used here. However, having all eigenvalues available may not be useful in this analysis because the majority of the eigenvalues are approximations to the continuous branches of the eigenvalues and may not contribute to flow instability. Furthermore, finding all eigenvalues is a computationally expensive task and spatial analysis requires solutions at different values of ω. If the analysis is concerned with a single instability, the benefit of a global method over a local method generally does not outweigh the substantial increase in computation cost.

Since both local and global method have their own strengths and weaknesses, they are used in tandem here to complement each other. In this work, the global method is used first to identify certain instability modes. This is then followed by the local method to track the evolution of the mode under different flow conditions. The shooting method may be the obvious choice for the local method but it can be inconsistent with the global method

due to differences in the discretization. Instead, the eigenvalue solver in the global method is replaced by the Arnoldi iteration (Arnoldi, 1951) to convert the method to a local one. The Arnoldi iteration, by design, searches for Ritz eigenvalues in the neighborhood of a prescribed point in the α space. Note that the Ritz eigenvalues are not necessarily the eigenvalues but typically show convergence near the prescribed point. Most importantly, the Arnoldi iteration is computationally much cheaper than the direct algorithm because it can be terminated by a convergence criterion imposed on the eigenvalues of interest.

3.1.6.2 Implementation of Briggs' Method

In Sec. 3.1.6, ω is restricted to a real frequency. Through analytic continuation, the same equations can be solved on a 2D mesh in the complex ω-plane using the same solution method. The mapping of this mesh onto the α-plane can be visualized to reveal any possible saddle points. As mentioned in Sec. 3.1.5.2, not all saddle points are pinch points that can prevent the lowering of the temporal inversion contour. Therefore, each saddle point structure has to be carefully verified to confirm that it is formed by two solution branches originating from opposite halves of the α-plane. Finally, the branch points on the ω-plane that correspond to these pinch points are examined to determine if any of these branch points lies above the real ω-axis. The branch point with the largest imaginary part will determine the time-asymptotic behavior of the flow.

The above procedure only reveals the approximate locations of the pinch points because the mesh on the complex ω-space can only have finite resolution. Using a very fine mesh may lead to a more accurate estimate of the pinch point location but it is computationally expensive due to the iterative nature of the method. To alleviate this issue, the saddle points are identified using the method proposed by Lesshafft & Marquet (2010). This method requires the solution with the temporal linear stability problem and its adjoint. To this end,

Eq. (3.6) is cast into a temporal eigenvalue problem of the form:

$$\boldsymbol{A}_\omega \hat{\boldsymbol{\phi}} = \omega \boldsymbol{B}_\omega \hat{\boldsymbol{\phi}} \ , \tag{3.19}$$

where $\hat{\boldsymbol{\phi}}$ is the eigenfunction vector. The corresponding discrete adjoint problem is

$$\boldsymbol{A}_\omega^* \hat{\boldsymbol{\phi}}^+ = \overline{\omega} \boldsymbol{B}_\omega^* \hat{\boldsymbol{\phi}}^+ \ , \tag{3.20}$$

where the superscript "*" and the over-bar denote the conjugate transpose and complex conjugate, respectively. The adjoint eigenfunction vector $\hat{\boldsymbol{\phi}}^+$ is normalized so that $\hat{\boldsymbol{\phi}}^+ \boldsymbol{B}_\omega^* \hat{\boldsymbol{\phi}} = 1$. After both the direct and adjoint temporal eigenvalue problems have been solved using the Arnoldi method, the group velocity can be evaluated as:

$$\frac{\partial \omega}{\partial \alpha} = \hat{\boldsymbol{\phi}}^+ \frac{\partial \boldsymbol{A}_\omega}{\partial \alpha} \hat{\boldsymbol{\phi}} \ . \tag{3.21}$$

The secant method is used as the root-finding technique to search for solutions of zero group velocity. Subsequently, the branch structure around the saddle points is obtained to verify whether the solution branches did originate from opposite half-planes.

3.2 Setup and Configurations

3.2.1 Experimental Configuration and Computational Setup

The non-premixed jet flame that was experimentally investigated by Füri (2001) is used as the basis of this analysis. Füri (2001) investigated two fuel mixtures in their experiment but only 'Mix 1' is considered in this work. For this setup, methane fuel is issued into the flame from a contoured jet nozzle at an axial velocity of $u_j = 22$ m/s. The nozzle exit diameter is $D_j = 7.5$ mm and its rim thickness is $0.16 D_j$. The fuel stream is surrounded by a coflow of air, supplied through a porous sintered plate. This operating condition corresponds to a

global Reynolds number of $Re = 1770$ and a Froude number of $Fr = 14$.

In this configuration, a shear layer is present between the high velocity fuel stream and the coflow. This shear layer can support a Kelvin-Helmholtz type instability mode, which is primarily induced by the velocity gradient in the shear layer. This instability mode is referred to as the inner mode here. There is an additional instability mode that is centered at a more radially outward location and it is denoted as the outer mode. The outer mode instability may be attributed to the density gradient induced by the heat release of combustion.

To obtain the base flow fields for linear stability analysis, detailed simulations are performed with different models. Due to the axisymmetric nature of the jet flame, the simulations are performed by solving Eq. (2.33) in a cylindrical coordinate system. Since the FPV model is utilized in Eq. (2.33e), the flamelet libraries are generated prior to the simulations. The reaction chemistry that is used in the library generation is discussed in the Sec. 3.2.2. In the discretization of Eq. (2.33), the spatial and temporal derivatives are treated separately. Specifically, a central finite difference scheme is used for the spatial discretization and a fraction-step method is employed for the temporal discretization. The full details of the numerical schemes are discussed by Pierce (2001).

The 3D computational domain is $15\,D_j \times 10\,D_j \times 2\pi$ in axial, radial and azimuthal directions, respectively. The computational grid consists of $190 \times 110 \times 32$ grid points for the three respective directions. For the fuel nozzle inlet, the velocity boundary conditions are either prescribed as a uniform flow or obtained from a forced pipe flow simulation. A plug-flow profile with an axial velocity of $U_{co} = 0.05$ m/s is used to describe the coflow stream. Lastly, the convective outflow and slip wall conditions are imposed at the outlet and the radial boundaries, respectively.

3.2.2 Model Approximations

In the following sections, different combinations of model approximations are considered to systematically investigate the effects of different approximations on instability dynamics. Specifically, the reaction chemistry, transport properties, gas law, and buoyancy effect are considered here. Clearly, the reaction chemistry plays an important role in determining the flame dynamics of a reacting flow. Two chemistry representations are investigated, representing the two opposite extremes in terms of the model fidelity. The simplest chemistry model is a one-step global reaction for methane-air combustion. The reaction mechanism takes the form

$$\mathrm{CH_4} + 2\mathrm{O_2} \xrightarrow{\mathrm{k_g}} \mathrm{CO_2} + 2\mathrm{H_2O}\ , \tag{3.22}$$

and the global reaction rate is represented as :

$$k_{\mathrm{g}} = A[\mathrm{CH_4}]^p[\mathrm{O_2}]^q \exp\left(-\frac{T_a}{T}\right), \tag{3.23}$$

and the numerical constants are (Westbrook & Dryer, 1981):

$$A = 1.3 \times 10^8 s^{-1}, \quad T_a = 5773K, \quad p = -0.3, \quad q = 1.3. \tag{3.24}$$

The complex chemistry kinetics utilized in this study for the methane-air reaction is the GRI-MECH 2.11 (Bowman *et al.*, 1997). Unlike the simple chemistry model, the details of the chemistry mechanism is not discussed here because it contains 219 reactions among 49 species.

As with the reaction chemistry kinetics, the comparison of a simple model with a more detailed model is the approach employed throughout this investigation to assess to impact of different sub-models. This is no different in the context of the transport model; the simple model for viscous-diffusive transport is the Chapman approximation. In this model,

the dynamic viscosity and diffusivity are assumed to be dependent on temperature as

$$\mu = \mu_0 \left(\frac{T}{T_0} \right)^n \quad , \quad \upsilon = \upsilon \left(\frac{T}{T_0} \right)^n \quad , \tag{3.25}$$

where n is assumed to be unity. For a more complete description of viscous-diffusive properties, we employ the mixture-averaged transport discussed in Sec. 2.1.1.

In a reacting flow, the specific heat capacities of the gaseous mixture can change significantly due to the increase in temperature. The thermally perfect gas approximation can account for this phenomena by expressing C_p and C_v as a function of temperature. This approximation is the more detailed model in the comparison of gas laws, and the simpler model would neglect this variation of specific heat capacities with temperature. The assumption of constant specific heat capacities is commonly referred to as the calorically perfect gas law.

By systematically increasing the fidelity of physical sub-models, five combinations of the models are considered here and summarized in Tab. 3.1. Among these permutations, case C1 uses the simplest set of models for the flow properties while case C2 improves upon case C1 with the thermally perfect gas approximation. At the other end of the spectrum of model fidelity, case C4 employs detailed chemistry, mixture-averaged transport, the thermally perfect gas assumption. Compared to case C4, case C3 is the same except that the Chapman approximation is utilized instead of the more complex mixture-averaged transport model. In addition, buoyant effects are also added to case C4 (denoted as case C4b) so that the impact of buoyancy can be assessed.

Case	Chemistry	Transport model	Thermal properties	Fr
C1	One-step chemistry	Chapman approximation	Calorically perfect	∞
C2	One-step chemistry	Chapman approximation	Thermally perfect	∞
C3	Detailed chemistry	Chapman approximation	Thermally perfect	∞
C4	Detailed chemistry	Mixture-averaged transport	Thermally perfect	∞
C4b	Detailed chemistry	Mixture-averaged transport	Thermally perfect	14

Table 3.1: Summary of the combinations of models considered to assess the effects of different model approximations on the instability dynamics.

3.3 Results

3.3.1 Mean Flow Results

For each combination of model approximations in Tab. 3.1, its corresponding mean flow is computed using detailed simulations. With the exception of case C4b, all simulations predict steady flow solutions so the mean flows of case C1-C4 are also the corresponding base flows. The computed radial profiles for axial velocity at axial location $x/D_j = 0.13$ and $x/D_j = 1.0$ are shown in Fig. 3.3a and Fig. 3.4a, respectively. Based on the figures, it is clear that the mean flow results are sensitive to model approximations. In fact, the difference in the mean flow profile is already observable at $x/D_j = 0.13$, illustrating the strong influence for the model approximations. Despite the variation of axial velocity profiles, all results generally show a localized pocket of high velocity on the oxidizer side. This can be attributed to the heat release effects of the chemical reactions that occur in this region of the adiabatic jet flame. Moreover, the non-adiabatic simulation results ,discussed in Sec. 3.3.6, do not show this pocket of high velocity.

In the comparison of radial temperature profiles in Fig. 3.3b and Fig. 3.4b, cases C1-C4 show considerable differences in terms of flame structure. Among all cases, case C1 displays the highest peak temperature and the broadest flame. This is partly due to the simple description of the reaction in the global reaction model (Williams, 1991). In addition, the broader flame can also be partially attributed to the calorically perfect gas representation.

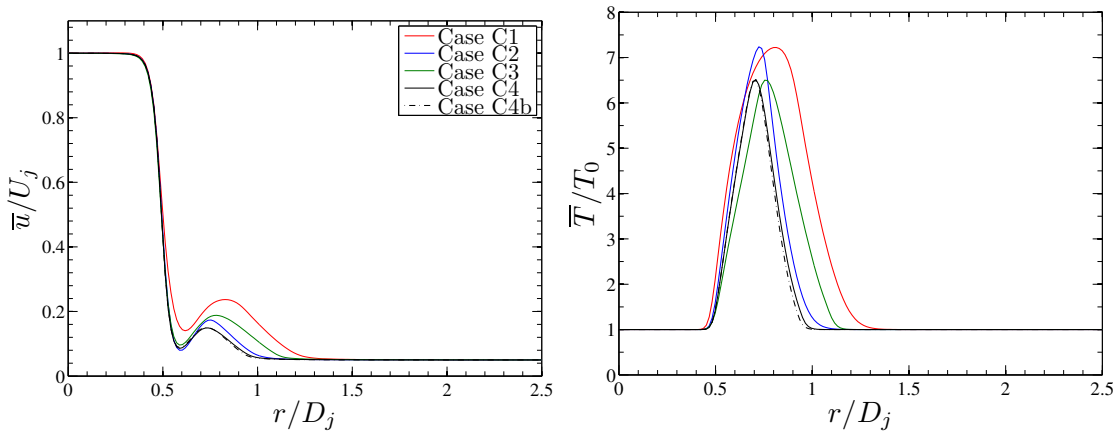

(a) Mean axial velocity.

(b) Mean temperature.

Figure 3.3: Radial profiles for (a) mean axial velocity and (b) mean temperature at $x/D_j = 0.13$.

This effect can be seen with case C2 in Fig. 3.3b where the relaxation of this thermodynamic description results in a thinner flame structure. Furthermore, this variation of flame structure is more readily observable in the mixture-fraction space. The comparisons of temperature profiles in the mixture-fraction space at $x/D_j = 0.13$ and $x/D_j = 1.0$ are shown in Fig. 3.5. The projection onto the Z-space reveals that the discrepancies due to model approximations are mostly restricted to the fuel-rich side of the flame. Compared to case C1, the flame of C2 shows a faster initial decrease in temperature for mixture fractions greater than stoichiometric.

Through the comparison of instantaneous temperature for cases C4 and C4b, the effect of gravity on the flow can be assessed. As mentioned earlier, the simulation results of case C4 are steady so the instantaneous temperature field for case C4 (shown in Fig. 3.6a) is also the mean field. However, the flow becomes unsteady when buoyancy effects are included in the simulation of the case C4b. The unsteadiness of case C4b is illustrated in Fig. 3.6b, where the instantaneous result in the left panel is clearly not the same as the time-averaged results in the right panel. A closer examination of Fig. 3.6b suggests that an absolute instability is present in the outer region of the jet which is responsible for the

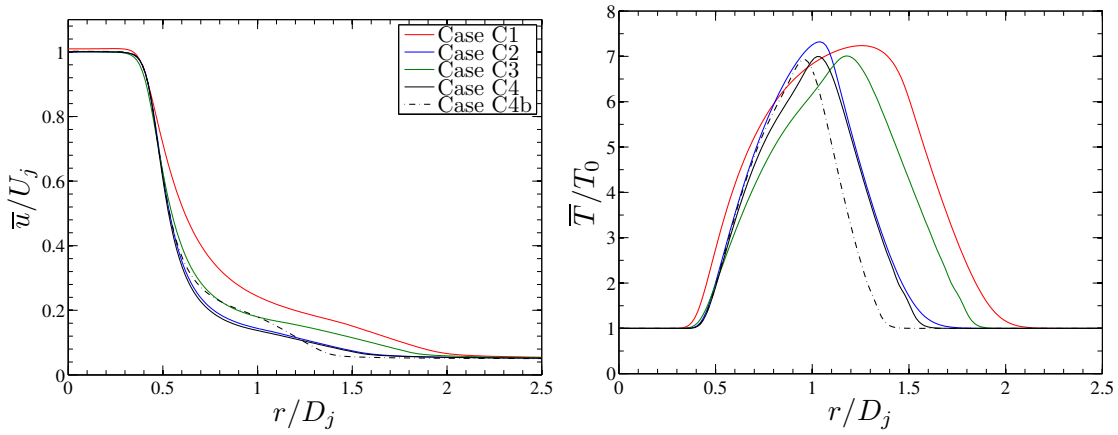

(a) Mean axial velocity.

(b) Mean temperature.

Figure 3.4: Radial profiles for (a) mean axial velocity and (b) mean temperature at $x/D_j = 1.0$.

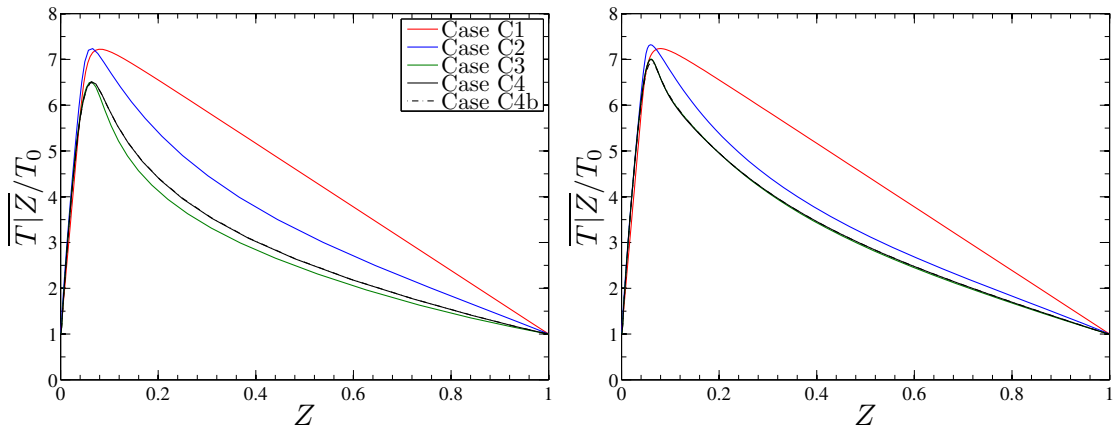

(a) Axial location: $x/D_j = 0.13$.

(b) Axial location: $x/D_j = 1.00$.

Figure 3.5: Comparison of mixture-fraction conditioned temperature profiles at (a) $x/D_j = 0.13$ and (b) $x/D_j = 1.0$.

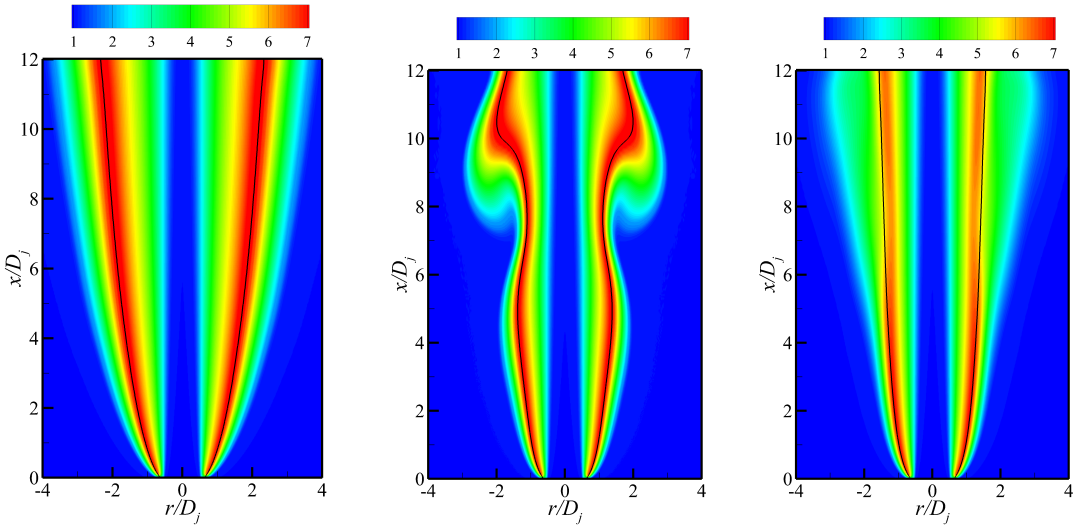

(a) Instantaneous temperature field for case C4.

(b) Instantaneous (left) and mean (right) temperature field for case C4b.

Figure 3.6: Mean temperature field for (a) case C4 at $Fr = \infty$ (without buoyancy). Instantaneous and mean field for (b) case C4b: the instantaneous result is shown in the left panel and the mean temperature is shown in the right panel.

temporal evolution of the flame.

Becker & Yamazaki (1978) and Mungal & coworkers (Muñiz & Mungal, 2001; Han & Mungal, 2001) have experimentally investigated the effect of buoyancy on the flow structure in laminar and turbulent non-premixed jet flames. By balancing buoyancy and inertial forces, Becker & Yamazaki (1978) derived a self-similarity coordinate in the form of:

$$\xi = x \left(\frac{\rho_O}{\rho_F} Fr^{-2} \right)^{1/3}. \tag{3.26}$$

where ρ_O/ρ_F is the density ratio between oxidizer and fuel. When $\xi < 1$, the effects of buoyancy on the flow are likely to be negligible. Applying this criterion to the non-premixed jet flame results suggests that buoyancy effects become relevant for $x/D_j > 4.8$. A qualitative comparison of the mean flow profiles between cases C4 and C4b agree reasonably well with this criterion. Since Eq. (3.26) is only derived by considering a force-balance, the contribution of buoyancy-driven instabilities is neglected in the application of

this criterion. A more complete criterion for buoyancy effects should augment ξ with the wave-number of the buoyancy-driven instability.

Fig. 3.6 also shows that the potential core of case C4b is qualitatively similar to case C4. This is because the inner momentum-driven shear is largely unaffected by gravitational forces and buoyancy effects are mostly confined to the outer region of the jet. Motivated by this finding, the instabilities associated with the inner and outer region of the jet flame are analyzed separately

3.3.2 Inner Mode Analysis

3.3.2.1 Growth Rate and Phase Speed

Using the mean flow results from the detailed simulations at x/D_j =0.13, spatial stability analyses for all cases in Tab. 3.1 are performed. The growth rate and phase speed of the inner Kelvin-Helmholtz mode as functions of the angular frequency $\omega_r D_j/U_j$ are illustrated in Fig. 3.7. Based on these results, all cases agree for $\omega_r D_j/U_j < 1$ but slowly diverge as the frequency is increased. Through comparison of cases C1 and C2, the impact of different perfect gas models can be assessed. Specifically, the analysis that employs the calorically perfect-gas approximation under-predicts growth rate with increasing frequency.

Similarly, the effect of reaction chemistry on the growth rate can be assessed by comparing the analysis results for cases C2 and C3. Figure 3.7a clearly shows that case C3 predicts growth rates higher than those of case C2 for the frequency range of $2 \leq \omega_r D_j/U_j \leq 8$. This can be attributed to the chemistry-induced shift of the mean flow profiles and a higher flame temperature seen in the mean flow of case C2. In particular, these two observations are probably due to the over-prediction of heat release in case C2, which is known to attenuate the growth of inviscid instabilities (Shin & Ferziger, 1991). In addition, the increase in viscosity due to the higher peak-temperature of case C2 may also play a role in impeding the growth of the inner instability mode.

The linear stability analysis of cases C3 and C4 are performed using the same chemical

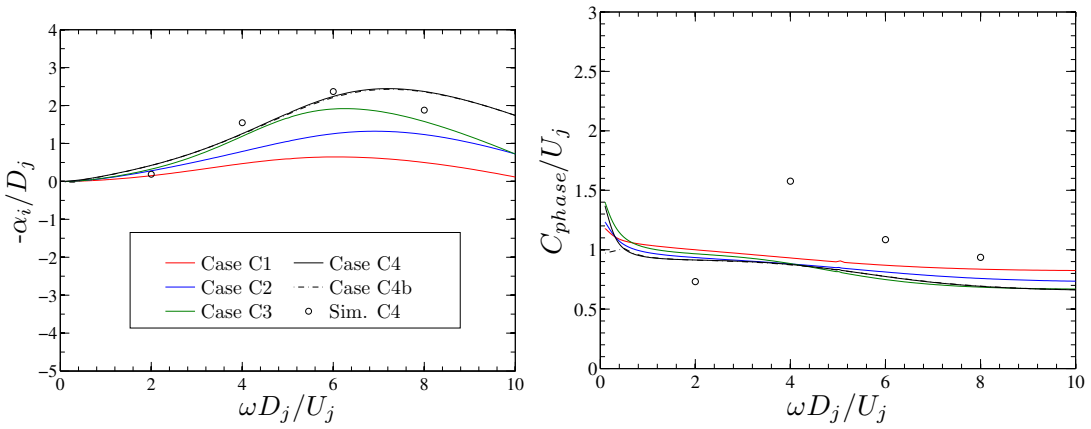

(a) Growth rate.

(b) Phase speed.

Figure 3.7: Comparison of results from linear stability analysis using different models for (a) growth rate and (b) phase speed of the jet flame at axial location $x/D_j = 0.13$; shown in symbols are growth rate and phase speed evaluated from simulation of case C4.

kinetics model but with different viscous-diffusivity models. Therefore, the higher growth rate of case C4 for $\omega_r D_j/U_j > 5$ can be the result of a different transport model. The Chapman approximation (used in case C3) overpredicts the viscosity, thus reducing the growth rate of the instability. It is also worth mentioning that the phase speed in case C4 is overall lower than that of the other cases. Nevertheless, the phase speeds of all cases are very close to unity, indicating the inner mode is propagating at the jet velocity. (see Fig. 3.7b)

Quantitative comparisons of linear stability results with detailed simulation results for case C4 are presented in Fig. 3.7. These results are obtained by performing additional computations, in which the axial inlet velocity is harmonically forced. Uniform perturbations of axial velocity at frequencies of $\omega_r D_j/U_j = 2$, 4, 6 and 8 are imposed at the jet inlet for five different simulations. These perturbations are limited to an amplitude of 5% of the bulk axial velocity. The growth rate and phase speed are evaluated using flow-field solutions for radial velocity and velocity magnitude, respectively. Comparisons of results from the stability analysis and detailed simulations for the specific case C4 show overall good agreement. The detailed computations predict a maximum growth rate around $\omega_r D_j/U_j$=

Saddle point	α_0/D_j	$\omega_0 D_j/U_j$
K1	$1.550 - 5.139i$	$4.607 - 2.877i$
K2	$4.796 - 8.689i$	$5.931 - 2.253i$
K3	$4.914 - 13.475i$	$5.539 - 2.795i$

Table 3.2: Saddle points for inner mode at $x = 0.13$ for case C4b.

5, and the inner mode remains unstable for higher perturbation frequencies. In this context, it is also noteworthy to mention that despite the underlying assumptions of the linear stability method, the results remain in good agreement with the detailed simulation results even for perturbation frequencies up to $\omega_r D_j/U_j$ = 8 (corresponding to a physical frequency of 645 Hz).

To investigate whether the inner mode is a shear layer instability and is not affected by buoyancy, the analysis results of case C4b are also shown in Fig. 3.7. Although buoyancy effects are included in the analysis of case C4b, the results are identical to case C4. Therefore, this comparison suggests that the inner mode is insensitive to buoyancy effects.

3.3.2.2 Pinch Point Analysis

To determine if the inner mode is a convective instability or an absolute instability, we apply Briggs' method (described in Sec. 3.1.5.2) at $x/D_j = 0.13$. The results of this investigation is illustrated in Fig. 3.8a, showing the mapping of contours of constant ω_i on the complex α-plane. In this figure, three different saddle points can be identified and the corresponding $(\alpha_0/D_j, \omega_0 D_j/U_j)$ coordinates are shown in Tab. 3.2, indicating that all three saddle points are located in the lower half of the ω-plane (i.e. $\omega_r < 0$). By Briggs' criterion, the inner mode is therefore a convective instability at location $x/D_j = 0.13$. In addition, the saddle points are also solved as a function of Froude number and the results are shown in Fig. 3.8b. The saddle points are invariant to Froude number variation, reaffirming our finding that the inner mode is insensitive to gravitational effects.

Figure 3.8b shows the presence of a turning point on the α-plane. Under the mapping

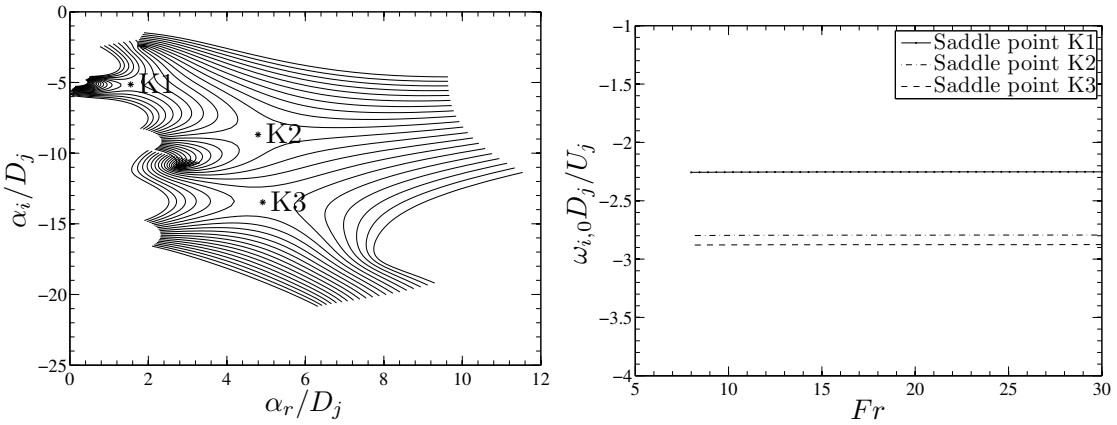

(a) Branch point structure.

(b) Effects of Froude-number on pinch point locations.

Figure 3.8: Pinch point analysis of inner mode: (a) shows the structure of dispersion relation near the pinch points at $x/D_j = 1.0$; (b) illustrates the temporal growth rate of the pinch points for a range of Froude-numbers.

of the dispersion relation, this turning point manifests as a saddle point in the ω-space. This behavior was also observed by Papas *et al.* (2003) and can be attributed to the quadratic ω term in the dispersion equation. To demonstrate this property, a simplified perturbation equation for $\hat{v}$ is obtained from Eq. (3.3) by neglecting contributions from $\widehat{Z}$ and $\hat{w}$ while omitting the viscous and gravitational effects. The simplified equation is written as:

$$(\omega - \alpha\widetilde{u})^2 V_1 \widehat{v} - (\omega - \alpha\widetilde{u}) V_2 \widehat{v} - V_3 \widehat{v} = (\omega - \alpha\widetilde{u}) P_1 \widehat{p} + P_2 \widehat{p}\,, \tag{3.27}$$

where the terms V_1-V_3, P_1, and P_2 are evaluated from base-flow properties and chemical

state:

$$V_1 = \bar{\rho}\left(\frac{1}{r} + \frac{d}{dr}\right) , \tag{3.28}$$

$$V_2 = i\frac{1}{\bar{\rho}}\frac{d\dot{\omega}_C}{dr}\partial_C\mathcal{G}_\rho - \alpha\bar{\rho}\frac{d\widetilde{u}}{dr} + \partial_C\mathcal{G}_{\dot{\omega}_C}\left(\frac{1}{r} + \frac{d}{dr}\right) , \tag{3.29}$$

$$V_3 = i\alpha\partial_C\mathcal{G}_{\dot{\omega}_C}\frac{d\widetilde{u}}{dr} , \tag{3.30}$$

$$P_1 = -i\alpha^2 , \tag{3.31}$$

$$P_2 = -\frac{\alpha^2}{\bar{\rho}}\partial_C\mathcal{G}_{\dot{\omega}_C} . \tag{3.32}$$

Equation (3.27) shows that the terms involving $\partial_C\mathcal{G}_{\dot{\omega}_C}$ can lead to a turning point in the α-space. This turning point vanishes when the equation becomes linear in ω under non-reacting conditions, *i.e.*, $\partial_C\mathcal{G}_{\dot{\omega}_C} = 0$. Although simplified, this simplified analysis shows that the chemical reaction is a possible source for a branch-cut in the α-space. A more detailed analysis is required to fully characterize the origin and implications of this branch point and it could be the subject of future work.

In a weakly non-parallel flow, the evolution of saddle points along the axial direction needs to be examined in order to fully determine whether the instability mode is convective or absolute. If the instability mode is found to be absolute for a sizable region of the flow, the flow is then considered absolutely unstable. Since the jet flame is weakly non-parallel, the saddle points of the inner mode are tracked along the axial directions. The temporal growth rates for the saddle points along x/D_j are shown in Fig. 3.9a. Based on Fig. 3.9a, it can be seen that the saddle points K1 and K3 still indicate that the inner mode is a convective instability. However, the saddle point K2 crosses from the lower half of the ω-plane to the upper half at $0.6 \leq x/D_j \leq 1.2$, suggesting that the inner instability mode may become absolute. To characterize the nature of the instability in that region, the saddle point structure of K2 at $x/D_j = 1.0$ is evaluated and shown in Fig. 3.9b. In addition to the solid lines which denote the contour mapping of constant ω_i, the spatial solution branches

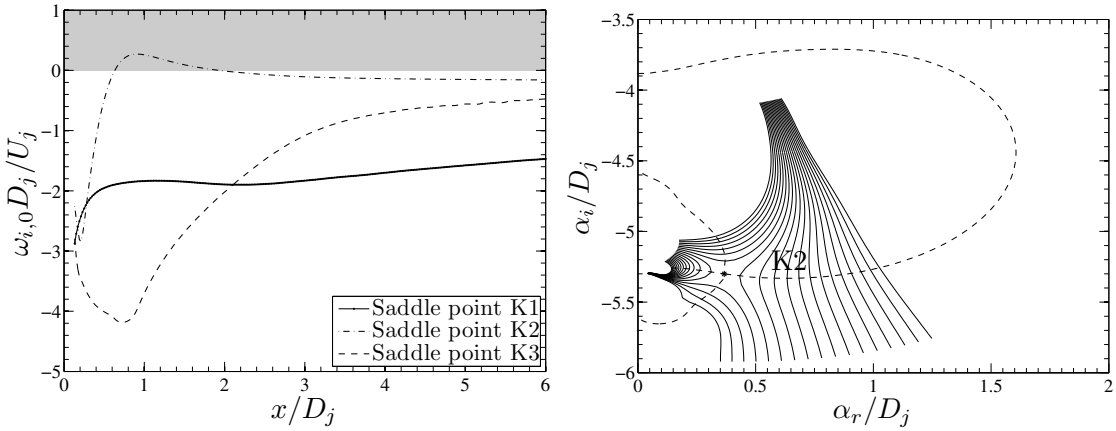

(a) Temporal growth rate of saddle points along axial direction.

(b) Branch point structure around saddle point K2 at $x/D_j = 1.0$.

Figure 3.9: Pinch point analysis for the inner mode: (a) showing the temporal growth rate of saddle points along axial distance x/D_j and the upper half plane is shaded to indicate the necessary criterion for absolute instability; (b) saddle point structure around K2 at $x/D_j = 1.0$; the solid lines denote curves of constant ω_i while the dashed lines are of $\omega_r = \omega_{r,0}$ with varying ω_i.

for a constant ω_r is also shown as dashed lines. By tracing the dashed lines, the two spatial branches that form the saddle point shown to originate from the same lower half plane. This property of saddle point fails Briggs' second criterion for an absolute instability. Therefore, the inner mode is conclusively a convective instability for the entire jet flame.

3.3.3 Mode Reconstruction

Although the linear stability analysis method developed here is local to an axial location, the analysis results can be extended to approximate the global mode. The procedure, proposed by Oberleithner *et al.* (2011), is employed here to approximate the global mode structure. The non-buoyant case C4 is used as the configuration for which this method is applied to. In this method, the solution of local linear stability analysis along x/D_j is

combined as:

$$\phi''(t,x,r,\theta) = \mathrm{Re}\left[\frac{\hat{\phi}(\mathrm{r};\mathrm{x})}{\left|\hat{\phi}(\mathrm{r};\mathrm{x})\right|}\exp\left\{\mathrm{i}\int_{\mathrm{x_0}}^{\mathrm{x}}\left[\alpha(\xi)\mathrm{d}\xi + \mathrm{m}\theta - \omega\mathrm{t} - \arg\left(\hat{\phi}(\mathrm{r_0};\mathrm{x})\right)\right]\mathrm{d}\xi\right\}\right] \tag{3.33}$$

where $\mathrm{Re}(\cdot)$ denotes the real part of an complex number, $\left|\hat{\phi}\right| = \hat{\phi}\overline{\hat{\phi}}$ is the modulus of $\hat{\phi}$. The exponential term of the global mode is introduced to phase-align the individual eigenfunctions at r_0. Note that this approximation of global mode does not capture the spatial growth of the local eigenfunctions, which can be accounted for by using a multi-scale expansion (Crighton & Gaster, 1976) but that is beyond the scope of this work.

Results from the mode reconstruction are compared against the inner instability mode from simulations at two excitation frequencies. Since the inner mode is convectively unstable, it is excited in the simulations by a harmonic forcing of the axial velocity at the inlet. The amplitude of this imposed fluctuation is limited to 5% of U_j in order to avoid the nonlinear response of the jet flame.

Two perturbation frequencies, namely $\omega_r D_j/U_j = 2$ and $\omega_r D_j/U_j = 5$, are considered in this investigation. Comparisons of global mode shapes between analyses and simulation at these two frequencies are shown in Fig. 3.10 and Fig. 3.11, respectively. Both comparisons indicate that the reconstructed mode is in reasonable agreement with the excited inner mode from the detailed simulations. Aside from the small shift in mode shape with increasing downstream distance, the wavelengths of the reconstructed inner instability modes are generally similar to the simulation results. This favorable agreement is expected because the inner mode is advected by the shear layer, which evolves slowly along the axial direction. In comparison of the mode shapes at the higher frequency, the discrepancies in the amplitude of the instability modes are more apparent for $x/D_j > 7$. After the initial growth of the inner mode at $\omega D_j/U_j = 5$, the simulation shows a mode that decays much faster than predicted by the locally linear analysis. There are many possible factors that may be responsible for this discrepancy but it is usually attributed to the non-linearity of the high

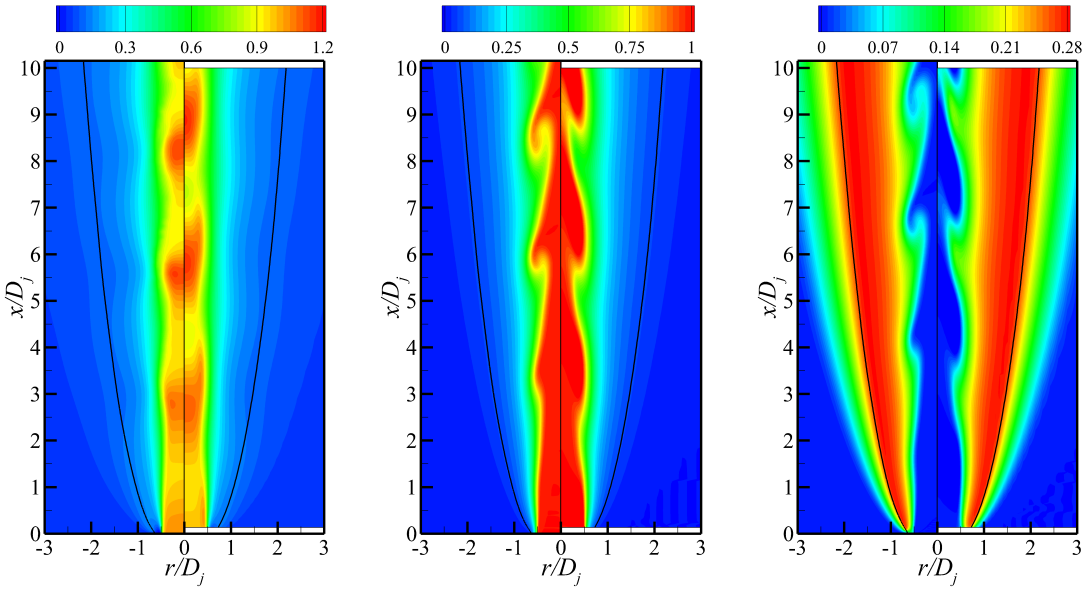

(a) Axial velocity, u/U_j. (b) Mixture fraction, Z. (c) Progress variable, C.

Figure 3.10: Comparison of instability modes from detailed simulation (left) and reconstruction from linear stability analysis (right mirror image) for (a) axial velocity, (b) mixture fraction, (c) progress variable of case C4 with forcing frequency $\omega_r D_j/U_j = 2$.

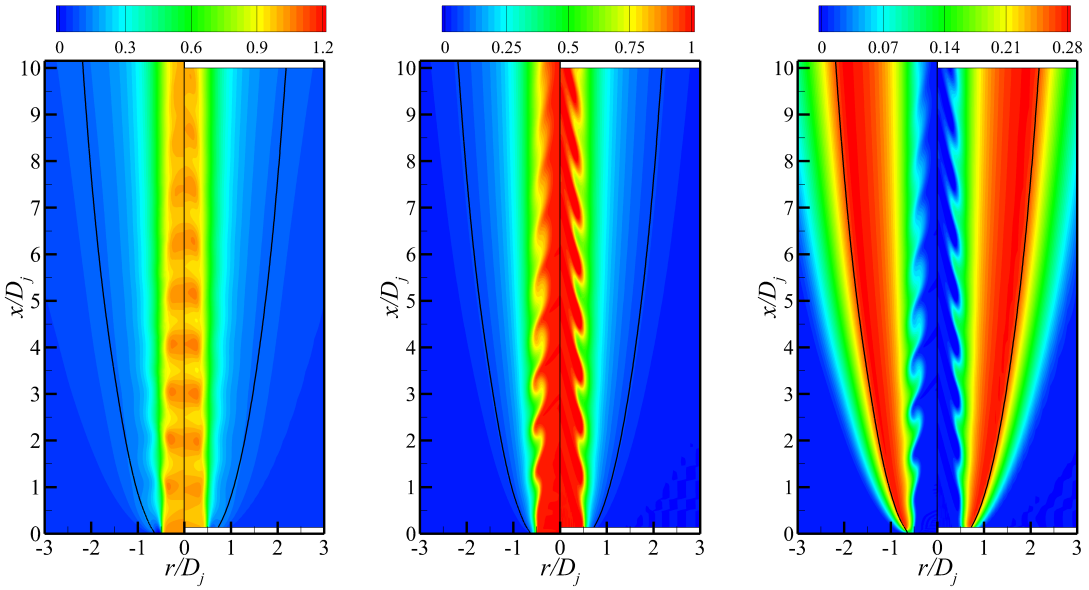

(a) Axial velocity, u. (b) Mixture fraction, Z. (c) Progress variable, C.

Figure 3.11: Comparison of instability modes from detailed simulation (left) and reconstruction from linear stability analysis (right mirror image) for (a) axial velocity, (b) mixture fraction, (c) progress variable; case C4 with forcing frequency $\omega_r D_j/U_j = 5$.

frequency excitation. Another contributing factor is that the combustion processes in reacting flows are highly non-linear. In addition, non-parallel effects, due to the spreading of the jet, may become more pronounced at locations further downstream.

3.3.4 Outer Mode Analysis

The detailed simulation of the buoyant jet flame of case C4b predicts an oscillatory outer mode that is not observed in the cases without buoyancy. Based on previous works, this outer mode is likely to be self-sustaining as it is to assumed be an absolute instability. To conclusively characterize this instability, local stability analysis is utilized to determine whether there exists a region wherein this instability is absolute.

Using the method discussed in Sec. 3.1.6.2, the saddle points are solved as a function of x/D_j. The imaginary part of the frequency for the two most unstable saddle points are shown in Fig. 3.12a for $0.133 < x/D_j < 3$. The upper half of the ω-plane of Fig. 3.12a is shaded grey to ease the identification of possible absolute instability. Results indicate that the saddle point O1 moves from the upper-half of the ω-plane to the lower-half at $x/D_j \approx 1.25$. This trajectory of the saddle point O1 suggests that the outer mode may undergo transition from absolute to convective near this axial location.

To confirm that the outer mode is indeed an absolute instability for $x/D_j < 1.25$, the branch structure of saddle point O1 is computed at $x/D_j = 1$ and presented in Fig. 3.12b. This figure illustrates that the pinch point O1 is formed by two solution branches originating from the lower and upper half planes of the α-space. This branch structure satisfies the second criterion of Briggs' method, indicating that the flame of case C4b is absolutely unstable. At the same axial location of $x/D_j = 1$, the saddle point O2 is also located on the upper-half of the ω-plane. However, this singularity is not an indicator of absolute instability as it is formed by branches originating form the same half-plane in the α-space.

However, the self-sustaining outer instability mode is absent in case C4 where gravity effects are ignored. This suggest that buoyancy effects can affect this instability mode by

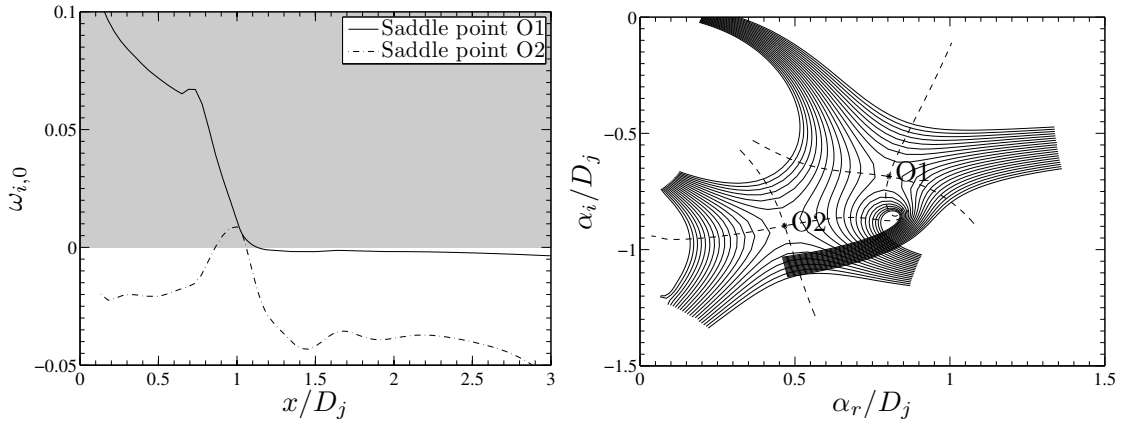

(a) Evolution of $\omega_{i,0}$ along x/D_j for outer mode.

(b) Branch point structure around saddle point O1 and O2 at $x/D_j = 1.0$.

Figure 3.12: Pinch point analysis for outer mode: (a) temporal growth rate of saddle points along x/D_j and upper plane is shaded to indicate necessary criterion for absolute instability; (b) branch point structure at $x/D_j = 1.0$; the solids lines denote curves of constant ω_i while the dashed lines are of $\omega_r = \omega_{0,r}$ with varying ω_i.

changing it into an absolute instability. To verify this claim, the complex frequencies of both saddle points are evaluated as a function of Froude-number. Results of this analysis at $x/D_j = 1$ are shown in Fig. 3.13. Unlike the inner mode, both saddle points exhibit significant dependency on the Froude-number. More specifically, the saddle points drift below the real ω axis with increasing Froude-number. This crossing between half-planes indicates that the outer mode becomes convectively unstable when the buoyancy effect is reduced, a finding consistent with the results of the simulations.

3.3.5 Nonlinear Instability Dynamics

In the experiment by Chen *et al.* (1989), both the inner Kelvin-Helmholtz mode and the buoyancy driven outer mode can be observed at the same time. Linear stability analysis is shown to be useful for the investigation of the two modes but it cannot account for non-linear coupling between the two modes when they are excited simultaneously. Therefore, detailed simulations are used as the primary tool to investigate the jet flame behavior when both instabilities are present. The simulation is similar to that of case C4b but the fuel

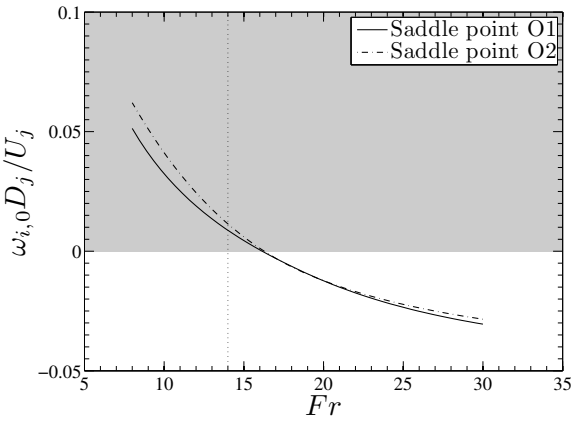

Figure 3.13: Evolution of saddle points of outer mode at $x/D_j = 1.0$ as a function of Froude-number. The shaded area is a necessary criterion for absolute instability.

inlet is forced with axial velocity oscillations at frequency $\omega D_j/U_j = 5$ and amplitude of 2.5% of U_j. Instantaneous results for axial velocity, mixture fraction and temperature are illustrated in Fig. 3.14. In this figure, the inner Kelvin-Helmholtz mode and the buoyancy-driven outer mode are clearly visible.

Point-wise history of the temperature is extracted from the simulation for spectral analysis. The data-collection locations, shown in Fig 3.14c, are distributed along the lines of $r/D_j = 0.5$, $r/D_j = 1$ and $x/D_j = 5$. The measurements along $r/D_j = 0.5$ are at the lip-line, and thus are associated with the shear layer. Locations along $r/D_j = 1$ are of interest because they mostly correspond to the stoichiometric reaction zone. Figure 3.15a shows the temperature signal at several point-wise locations along $x/D_j = 5$. At $r/D_j = 1$ of this axial location, the oscillation amplitude of the temperature reaches values in excess of 50% of the mean temperature. Since the flamelet model is used in this simulation, the temperature is mapped to the mixture fraction and progress variable. Therefore, the large fluctuation of temperature also corresponds to substantial variations of mixture fraction and progress variable. At the same axial location, the saturation of temperature fluctuation at $r/D_j = 2$ can also be seen in Fig. 3.15a. This phenomena is physical as the lower bound correspond to the inlet temperature which is the lowest possible value attainable in combustion. However, such non-linear effects are not easily accounted for in the linear stability

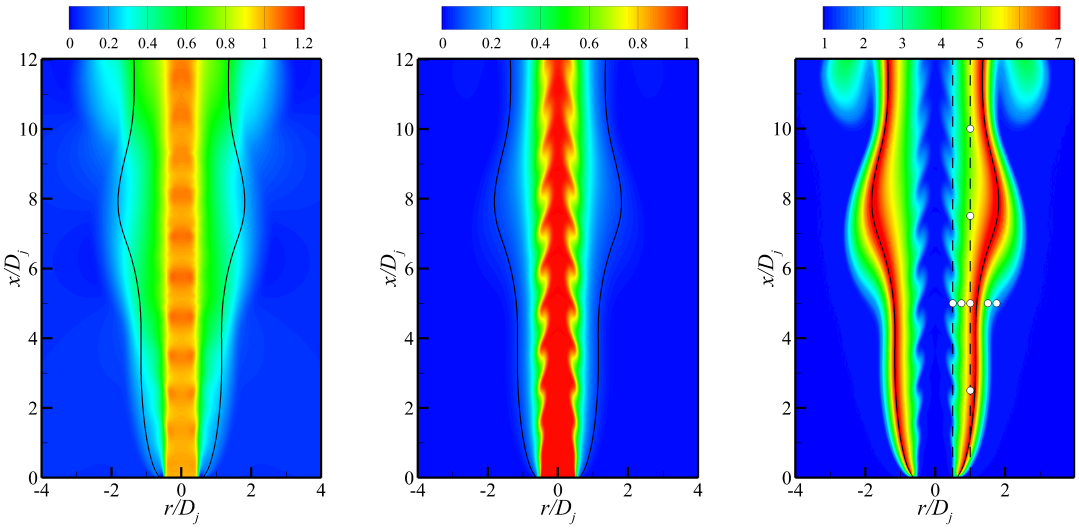

(a) Axial velocity, u/U_j. (b) Mixture fraction, Z. (c) Temperature, T/T_0.

Figure 3.14: Instantaneous results of harmonically forced simulation for case C4b, showing (a) axial velocity, (b) mixture fraction, and (c) temperature; solid lines denote isocontour of stoichiometric mixture fraction while dashed lines and symbols indicate locations where temporal history of temperature is extracted for spectral analysis.

analysis as a single temporal mode expansion is not able to capture this bounded oscillation of temperature.

For a more systematic investigation of the frequencies involved in the flow, a Fourier transformation is applied to the temperature signals. The spectrums of the temperature are presented in Fig. 3.16, showing $\log_{10}(|F(T)|)$ as function of angular frequency and axial distance. Along the jet lip line, Fig. 3.16a shows a visible peak at the fundamental forcing frequency of $\omega_r D_j/U_j = 5$ and the higher harmonics. With increasing downstream location, the frequency peak near the fundamental frequency broadens due to spectral transfer. At the same time, the higher harmonics see a rapid decay in amplitude beyond $x/D_j \leq 5$.

The spatial evolution of the frequency spectrum at $r/D_j = 1.0$ is shown in Fig. 3.16b. Unlike at $r/D_j = 0.5$, the spectral signature of the inner mode is much attenuated while the outer mode is prominent. This can be seen in Fig. 3.16b where there is higher spectral energy at lower frequency and the oscillation at $\omega D_j/U_j = 5$ is suppressed. The lower frequency peak at $\omega D_j/U_j = 0.19$ is considered to be the frequency of the outer mode.

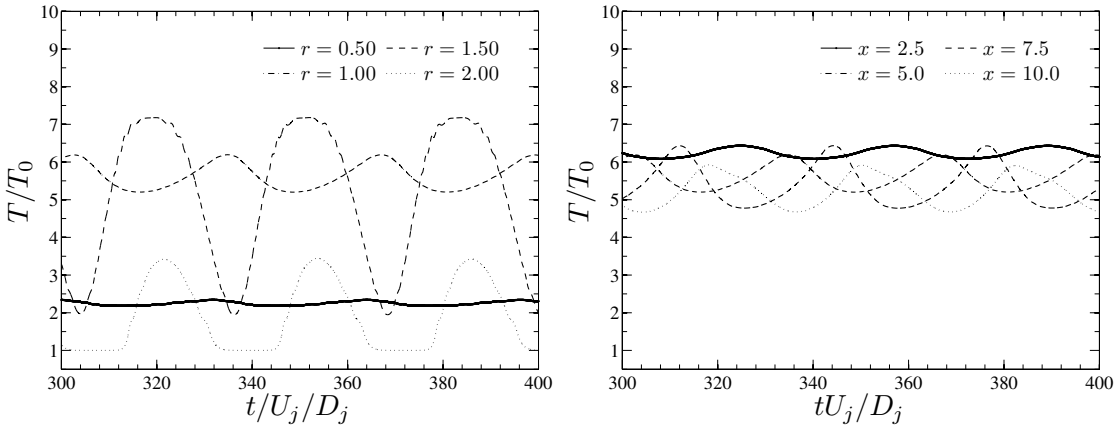

(a) Radial direction: $x/D_j = 5.0$. (b) Axial direction: $r/D_j = 1.0$.

Figure 3.15: Temporal evolution of temperature at different selected locations for case C4B with harmonic forcing.

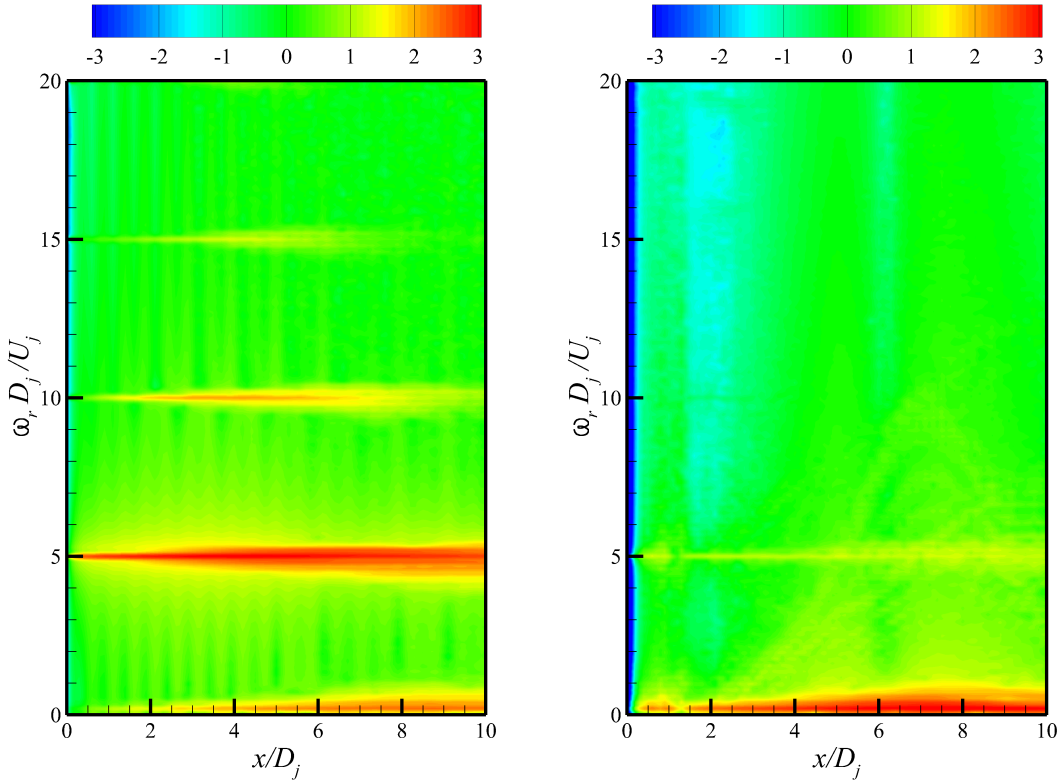

(a) Radial location: $r/D_j = 0.5$ (b) Radial location: $r/D_j = 1.0$

Figure 3.16: Frequency spectrum of temperature along axial distance for (a) $r/D_j = 0.5$ and (b) $r/D_j = 1.0$ (shown as dashed lines in Fig. 3.14c)

Moreover, Fig. 3.16b also shows the growth of this mode with increasing downstream locations.

Proper Orthogonal Decomposition (POD) is utilized here to investigate the coherent structure that is associated with the instabilities (Berkooz *et al.*, 1993). The POD method, also known as principal component analysis or Karhunen-Loève expansion, is frequently employed to construct optimal representations of the flow field dynamics. This is achieved by decomposing the sequence of data into a set of orthogonal empirical modes that minimize the squared error between the data and the POD representations. In the present case, the POD method is applied to the temperature field T using the following POD procedure:

$$\int\int \left\{ \left(T(t,\boldsymbol{x}) - \overline{T}(\boldsymbol{x})\right) - \sum_{i=1}^{N} a_i(t)\Theta_i(\boldsymbol{x}) \right\}^2 d\boldsymbol{x}dt \rightarrow \text{min.} \tag{3.34}$$

To construct the POD modes Θ_i, the snapshot method (Sirovich & Knight, 1985) is employed on 3000 realizations of the temperature field, obtained from the detailed simulation. The time increment $\Delta t U_j/D_j$ between each of these snapshots is 0.025, thus this series of snapshots spans approximately two periods of the outer mode. Such fine temporal resolution is used here in order to resolve the high frequency of inner mode. Since the POD method is optimal with respect to the L^2-norm as shown in Eq. (3.34), we can define a measure of the fluctuating energy content for each of the POD modes. It is important to note that the term "energy" is used loosely here as the temperature, in its primitive form, is not an accurate representation of energy. Nevertheless, this metric can be useful in the subsequent comparison of the inner and outer modes.

The normalized "energy" of the first 18 POD modes, sorted accordingly, are illustrated in Fig. 3.17a. In this figure, it can be seen that the first four POD modes account for more than 99% the energy. Moreover, the POD modes seem to come in pairs, which is the number of POD modes required to capture an advecting wave. This property is also shown in the phase plots of the time-coefficients of the first two modes. As seen in the top left

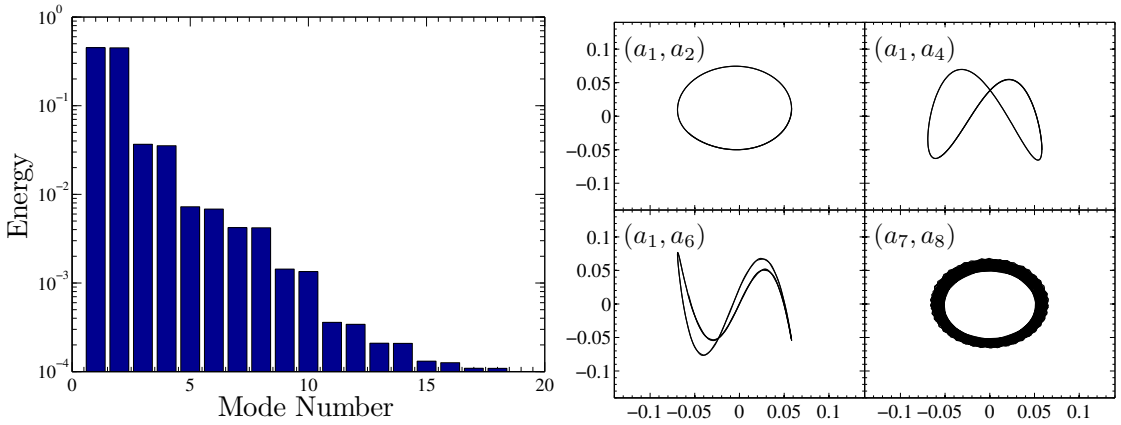

(a) POD energy spectrum. (b) Phase plot.

Figure 3.17: Results of POD mode analysis showing (a) the energy spectrum of first 18 POD modes and (b) time-coefficients for POD modes in the phase space

panel of Fig. 3.17b, the time coefficients a_1 and a_2 are phase shifted by $90°$, thus forming a circular trajectory in the phase plane. In addition, the phase plots of (a_1,a_4) and (a_1,a_6) are shown in Fig. 3.17b. From these phase plots, it can be seen that the fourth and sixth modes are higher harmonics of the first mode. Furthermore, the spatial structure of the fourth and sixth modes, illustrated in Fig. 3.18, qualitatively shows the doubling and tripling of the wavelength, respectively. Figure 3.18 also indicates that the first three pairs of POD modes are coherent structures mostly confined to the outside of the stoichiometric mixture fraction layer. Therefore, they are representative of the outer mode dynamics seen in the detailed simulations. It is noteworthy that the higher harmonics of the outer instability mode elucidated here are not entirely visible in the frequency spectrums in Fig. 3.16

The fundamental mode of the inner Kelvin-Helmholtz instability is contained in the 7th and 8th POD modes. This is illustrated in Fig. 3.18d where the 7th POD mode shows the characteristics of the inner Kelvin-Helmholtz instability. Like the outer mode, the advection of the inner mode is characterized by the $90°$ phase shift between a pair of POD modes. Again, this shift is evident from the circular orbit of corresponding time-coefficients shown in Fig. 3.17b

In application of POD to data, it is difficult to ignore the potential of POD modes to

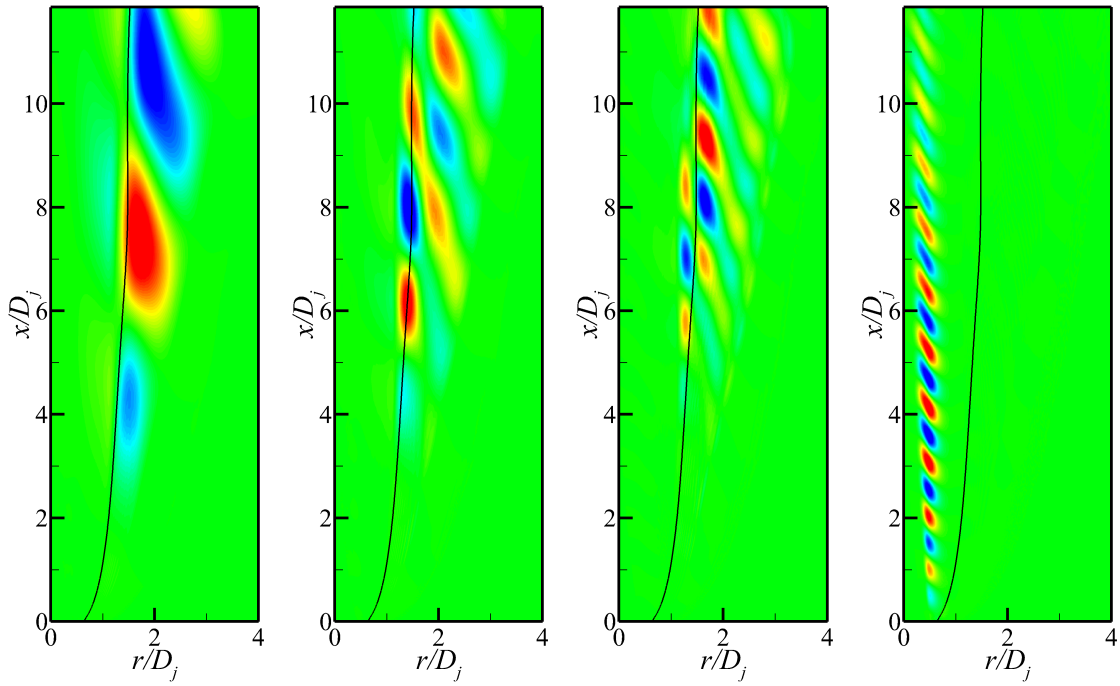

(a) 1st mode. (b) 3rd mode. (c) 5th mode. (d) 7th mode.

Figure 3.18: First four odd-number POD modes of the harmonically forced case C4b and the solid lines shown in the figures are the isocontours of mean stoichiometric mixture fraction. The coherent structures of the first three mode pairs are mostly restricted to the outside of the solid lines, and hence correspond to the outer buoyancy-driven instability. The fourth mode-pair (7th and 8th POD modes) shows fluctuations within the stoichiometric mixture fraction contour, thus are associated with the inner KH mode.

be used for lower-order control models (Bergmann *et al.*, 2009). To keep the lower-order model simple, the number of POD modes that can be included in the model is restricted to a small number. The cutoff threshold is usually based on the "energy" contained in the modes and the 99% limit is a common choice. However, external perturbations introduced by the control scheme may excite instability modes such as the inner Kelvin-Helmholtz instability, which may contribute less than 1% of the POD "energy".

3.3.6 Application to Incomplete Mean Flow

In Sec. 3.3.2.1, the linear stability analyses utilize the same model approximations as the corresponding simulations. With this formulation, all base-flow quantities needed for the analyses are readily available from the simulations. However, this may not be true in experiments where some of the essential thermo-chemical and flow quantities are not measured. Specifically, the point-wise mixture fraction and progress variable are usually not measured in a simple experiment. On the other hand, the temperature of a flame can be obtained from probe measurements. For example, Lingens *et al.* (1996) and Füri (2001) reconstructed the radial profiles of essential thermo-chemical variables so that linear stability analysis can be carried out on experimental flames measurements. The objective of this section is to show that our linear stability analysis framework can also be used on incompletely described mean flow data.

We have considered three cases of linear stability analysis on recovered mean flows. They are summarized in Tab. 3.3. Cases N1 and N2 are based on the semi-analytical approximation (Füri, 2001) to the time-averaged experimental measurements. In this approximation, the axial velocity is described as a hyperbolic tangent function. The mixture fraction follows the same analytic function but is corrected so that the stoichiometric mixture fraction matches the location of the peak temperature. The resulting axial velocity and mixture fraction profiles at $x/D_j = 0.13$ are shown in Fig. 3.19, along the experiment measurements. As expected, the profiles are very similar to the experimental data. Different

Case	Mean flow	Transport model
N1	Analytic	Chapman approximation
N2	Analytic	Mixture-averaged transport
N3	Simulation	Mixture-averaged transport

Table 3.3: Summary of the mean flows and transport models utilized in the linear stability analyses of the non-adiabatic jet flame.

transport models are used in cases N1 and N2, these models are not only used to evaluate the mean viscosity and diffusivity profiles but also in the linear stability analyses.

Unlike cases N1 and N2, the mean-profiles of a non-adiabatic simulation are used in case N3. In this simulation, the heat transfer to the nozzle rim is modeled using a non-adiabatic flamelet model (Lee *et al.*, 2011). However, this flamelet model utilizes a different progress variable formulation than that of the linear stability analysis, making the progress variables incompatible. Nevertheless, the definition of the mixture fraction is still consistent across the two models and its mean profile can be directly employed in the linear stability analysis. The mean results for this non-adiabatic case are shown in Fig. 3.19 for comparison with other cases and experimental measurements. Overall, the simulation results are in good agreement with the experimental results.

After obtaining the mean mixture fraction profiles, progress variable remains as the last quantity needed for a full description of the mean flow. Since the mean temperature profiles of cases N1-N3 are also available, a reverse lookup of the flamelet library for temperature is performed to reconstruct the mean progress variable profiles. This procedure ensures that the mean profiles of the mixture fraction and progress variable, under the flamelet model, map to a consistent temperature profile. In the cases where the mixture fraction profiles are also not available, a procedure similar to that of Lingens *et al.* (1996) can be employed to reconstruct the mean descriptions for Z and C. In this method, the radial profile of a jet flame is assumed to be described by a single flamelet solution so that the full thermo-chemical properties of the flame can be evaluated by matching the flamelet temperature to

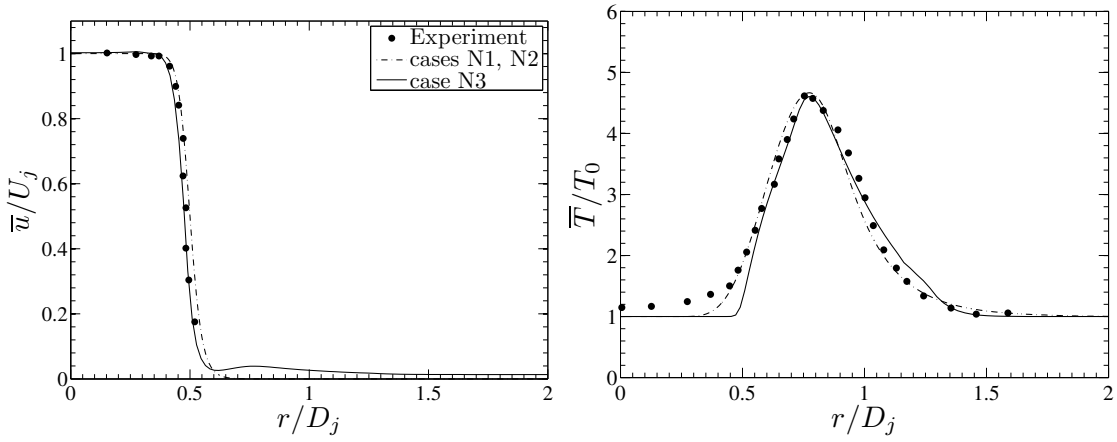

(a) Mean axial velocity profile at $x/D_j = 0.13$. (b) Mean temperature profile at $x/D_j = 0.13$.

Figure 3.19: The mean profiles of (a) axial velocity and (b) temperature at $x/D_j = 0.13$ for cases of non-adiabatic jet flames summarized in Tab 3.3.

the experimental measurements.

Using the reconstructed profiles of the progress variable and mixture fraction, density and viscosity for all three cases are evaluated with the flamelet library and are shown in Fig 3.20. Since cases N1 and N2 employ the same mean profiles of Z and C, the density profiles are the same. The differences in the transport properties can be seen in the mean viscosity profiles where the Chapman approximation of case N1 predicts a higher viscosity than the mixture-averaged transport model of case N2.

3.3.6.1 Growth Rate and Phase Speed

Linear stability analyses of cases N1-N3 are performed at $x/D_j = 0.13$ and the results are illustrated in Fig. 3.21. The experimental measurements and linear stability analysis results of Füri *et al.* (2002) are also shown in Fig. 3.21 for comparison. Overall, our analysis results for the cases N1-N2 are in good agreement with the linear analysis of Füri *et al.* (2002). More specifically, the previous work yields a growth rate curve that is slightly higher than the results of cases N1 and N2 (see Fig. 3.21a). Compared to experimental measurements, the growth rates obtained from the analyses are higher for $\omega D_j/U_j > 5$ due

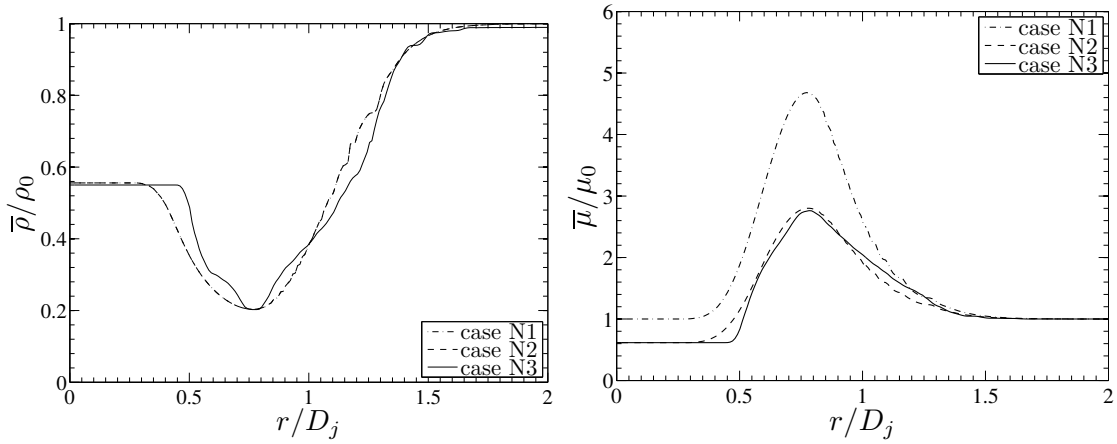

(a) Mean density profile at $x/D_j = 0.13$. (b) Mean viscosity profile at $x/D_j = 0.13$.

Figure 3.20: Recovered mean profiles of (a) density and (b) viscosity at $x/D_j = 0.13$ for cases of non-adiabatic jet flame configurations summarized in Tab 3.3.

to the non-linearity that is associated with the high frequency excitation in the experiment. Comparison between cases N1 and N2 also reveals that the higher viscosity of the case N1 dampens the growth rate of the instability. This finding is also consistent with the results shown in Sec. 3.3.2, wherein linear stability analyses are also performed with different transport models.

Even though the same transport model is being used in cases N2 and N3, the linear analysis results of case N3 show a higher growth rate for the frequencies range considered here. This increase in growth rates may be attributed to the shift in the temperature profile seen in Fig. 3.19b. Since the location of the temperature peak is further away from the inner mode for case N3, the dampening effect of heat release on the Kelvin-Helmholtz type instability is reduced. In spite of these differences in computed growth rates, the phase speed of all three cases, shown in Fig. 3.21b, are relatively similar. Again, this insensitivity of phase speeds to parameter changes is also observed and discussed in Sec. 3.3.2.

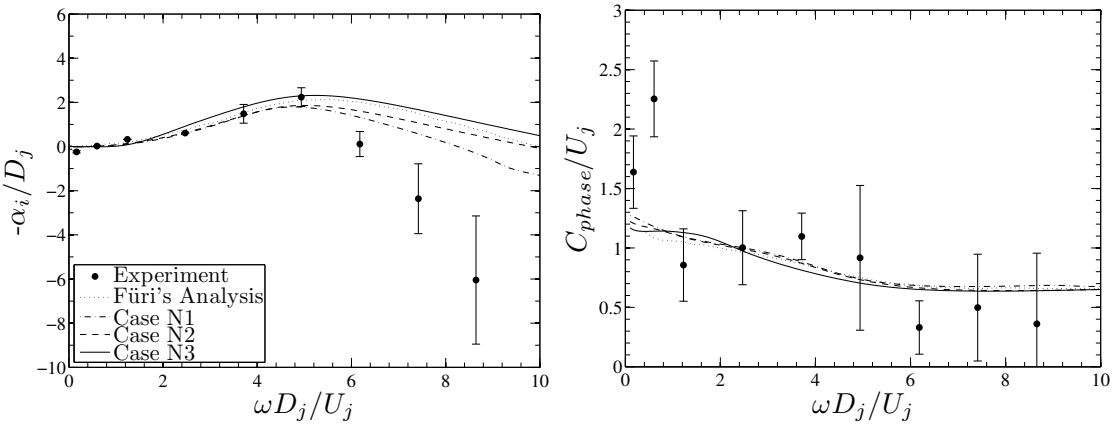

(a) Growth rate.

(b) Phase speed.

Figure 3.21: Comparison of (a) growth rates and (b) phase speeds obtained from linear stability analysis of experiments at axial location $x/D_j = 0.13$ for the non-adiabatic jet flame.

CHAPTER 4

High Fidelity Method and Large-Eddy Simulation

The large-eddy simulation (LES) method, as mentioned earlier, is a numerical turbulent simulation method which resolves the large scale turbulence while employing model for the small scale phenomena. This chapter opens with the discussion on the filtered governing equations and follows with the descriptions of the turbulence models used in this study. Since a solution is sought in a complex geometry, the numeric method associated with discretization of the filtered governing equations is also briefly mentioned here. Then, this chapter finishes with simulation results for the non-reacting and reacting cases.

4.1 Methodology

4.1.1 Turbulence Models for Sub-grid Stresses and Fluxes

The unclosed terms appearing in Eq. (2.45) are the sub-grid stress $\overline{\underline{\underline{\sigma}}}^{res}$ and the scalar fluxes $\overline{\boldsymbol{\tau}}_{\phi}^{res}$. One of the approaches to model these terms is based on the eddy viscosity assumption, which for $\overline{\underline{\underline{\sigma}}}^{res}$ is given by

$$\overline{\underline{\underline{\sigma}}}^{res} = \bar{\rho}\widetilde{\boldsymbol{u}}\widetilde{\boldsymbol{u}} - \bar{\rho}\widetilde{\boldsymbol{u}\boldsymbol{u}} = 2\bar{\rho}\nu_t\widetilde{\underline{\underline{S}}} - \frac{2}{3}\bar{\rho}\widetilde{k}\underline{\underline{I}}. \tag{4.1}$$

In most eddy viscosity models, the sub-grid kinetic energy is assumed to be small and thus is usually neglected (Pierce, 2001). With this assumption, this type of models is concerned with the approximation of the eddy viscosity, ν_t using only the filtered quantities. The classical eddy viscosity model for LES is attributed to Smagorinsky (1963) and is described by

$$\nu_t = C_\nu \frac{k^2}{\epsilon} = C_s \Delta^2 \left\| \widetilde{\underline{S}} \right\|, \tag{4.2}$$

where $\|\widetilde{\underline{S}}\| = (2\widetilde{\underline{S}} : \widetilde{\underline{S}})^{1/2}$. The standard value for C_s is approximately 0.18 but it can depend on the local flow topology. If a constant C_s is used in LES, the eddy viscosity near the walls can be over-predicted and may inhibit the flow separation behavior. This property is undesirable, so the constant coefficient Smagorinsky model is usually utilized together with wall damping of the eddy viscosity (Van Driest, 1956). A better solution is to dynamically determine the local C_s using the procedure proposed by Germano *et al.* (1991) with modification by Lilly (1992). This dynamic Smagorinsky model is shown to be reproduce vanishing viscosity near the walls (Meneveau & Katz, 2000). However, the dynamic procedure does not guarantee non-negative values for C_s, and negative viscosity can lead to numerical instability. In practice, spatial averaging in the homogeneous directions can be employed to mitigate this problem. In more complex configurations where there is no homogeneous direction, local averaging may be performed but it is generally insufficient to eliminate negative ν_t.

Recognizing this limitation of the dynamic Smagorinsky model, new eddy-viscosity models have been developed to account for the near wall decay of ν_t without dynamic coefficients. Two eddy-viscosity models are utilized in this work, and they share this property. The first model is the Wall-Adapting Local Eddy-viscosity (WALE) model proposed by Nicoud & Ducros (1999). In this model, the eddy viscosity is evaluated as

$$\nu_t = (C_w \Delta)^2 \frac{\left(S^d_{ij} S^d_{ij}\right)^{3/2}}{\left(S_{i,j} S_{i,j}\right)^{5/2} \left(S^d_{ij} S^d_{ij}\right)^{5/4}}, \tag{4.3}$$

where

$$S_{ij} = \frac{1}{2}\left(\alpha_{ij} + \alpha_{ji}\right) - \frac{1}{3}\delta_{ij}\alpha_{ij} \tag{4.4}$$

$$S^d_{ij} = \frac{1}{2}\left(\alpha_{ik}\alpha_{kj} + \alpha_{jk}\alpha_{ki}\right) - \frac{1}{3}\delta_{ij}\alpha_{kl}\alpha_{kl}, \tag{4.5}$$

$$\alpha_{ij} = \frac{\partial \widetilde{u}_j}{\partial x_i}. \tag{4.6}$$

This eddy viscosity model is built in such a way that the cubic decay of eddy viscosity near the walls can be reproduced in simulations. The constant coefficient, C_w is set to 0.5 and Δ is approximated with the cubic root of an element's volume.

The other eddy viscosity model used in this study is the model by Vreman *et al.* (2009). In the Vreman model, the eddy viscosity is given by

$$\nu_t = C_V \sqrt{\frac{B_\beta}{\alpha_{ij}\alpha_{ij}}}\ , \tag{4.7}$$

where

$$\beta_{ij} = \Delta^2 \alpha_{mi}\alpha_{mj}, \tag{4.8}$$

$$B_\beta = \beta_{11}\beta_{22} - \beta_{12}^2 + \beta_{11}\beta_{33} - \beta_{13}^2 + \beta_{22}\beta_{33} - \beta_{23}^2\ . \tag{4.9}$$

Eddy viscosity predicted by the Vreman model is designed to vanish for the thirteen types of laminar flows in which the theoretical sub-grid dissipation should be zero. Flow near a wall is one of these special cases so it is also suitable for a wall bounded flows. The model coefficient C_V is related to C_s by $C_V \approx 2.5C_s^2$ and a value of $C_V = 0.07$ is used here.

The eddy viscosity assumption is also employed for the closure of the sub-grid scalar fluxes, *i.e.*

$$\overline{\boldsymbol{\tau}}^{res}_{\phi} = \bar{\rho}\widetilde{\boldsymbol{u}}\widetilde{\phi} - \bar{\rho}\widetilde{\boldsymbol{u}\phi} = \bar{\rho}\alpha_t \nabla\widetilde{\phi}\ . \tag{4.10}$$

There are turbulence models that are tailored to the approximation of α_t but it is computed

here as

$$\alpha_t = \frac{\nu_t}{Sc_t} \, . \tag{4.11}$$

The turbulent Schmidt number Sc_t is assumed to be 0.9.

4.1.2 Turbulent Combustion Models for LES

Combustion in a turbulent environment introduces additional physical processes that must be considered in LES. More specifically, the interaction between turbulence and chemistry demands a careful modeling treatment in most numerical simulations of turbulent flames. For example, Clavin & Williams (1979) have shown that the turbulence can alter the flame speed of premixed flames by wrinkling the flame front. Non-premixed flames, on the other hand, are mixing controlled so the small scale turbulent mixing of fuel and oxidizer can affect the flame location. Moreover, a high level of turbulence can also induce the local extinction of flames in both non-premixed and premixed combustions.

4.1.2.1 Presumed PDF Closure

Clearly, small scale turbulence plays a greater role in turbulent reacting flows than in non-reacting flows. However, the sub-grid scale turbulence is not resolved in the LES approach and the models discussed in Sec. 4.1.1 do not consider turbulent chemistry interaction. Therefore, different models are needed to accurately predict turbulent combustion in LES. To this end, Pope (1991) introduces the concept of Filtered Density Function (FDF) to establish a formal framework to describe the sub-grid scale fluctuations needed for turbulent combustion modeling. The FDF of a scalar ϕ is defined as

$$\overline{F}\left(\psi, \boldsymbol{x}, t\right) = \int \delta\left(\psi - \phi\left(\boldsymbol{y}, t\right)\right) G\left(\boldsymbol{y}, \boldsymbol{x}; \Delta\right) d\boldsymbol{y}, \tag{4.12}$$

and the corresponding Filtered Mass Density Function (FMDF) for reacting flows is

$$\widetilde{F}\left(\psi,\boldsymbol{x},t\right)=\int\rho\left(\boldsymbol{y},t\right)\delta\left(\psi-\phi\left(\boldsymbol{y},t\right)\right)G\left(\boldsymbol{y},\boldsymbol{x};\Delta\right)d\boldsymbol{y}. \tag{4.13}$$

Solution strategies have been developed to solve for the FMDF equations in LES applications. However, these approaches are not pursued in this work due to the additional computational complexity introduced by these solution methods. Instead, the FMDF is approximated by a presumed PDF here by assuming that the sub-grid fluctuations of scalars are distributed like random variables.

In a presumed PDF closure for flamelet models, the flamelet library is convolved with a joint PDF of Z and Λ as:

$$\widetilde{\psi}=\int\int\mathcal{G}_{\psi}\left(Z,\Lambda\right)\widetilde{P}\left(Z,\Lambda\right)dZd\Lambda\ . \tag{4.14}$$

where $\widetilde{P}$ is the density-weighted PDF, *i.e.*

$$\widetilde{P}\left(Z,\Lambda\right)=\frac{\rho}{\overline{\rho}}P\left(Z,\Lambda\right)\ . \tag{4.15}$$

Using Bayes' theorem, the joint PDF of $\widetilde{P}\left(Z,\Lambda\right)$ is decomposed into a marginal PDF of Z and a conditional PDF of Λ on Z, *i.e.*

$$\widetilde{P}\left(Z,\Lambda\right)=\frac{\rho}{\overline{\rho}}P\left(Z\right)P\left(\Lambda|Z\right)=\frac{\overline{\rho}}{\rho}\widetilde{P}\left(Z\right)\widetilde{P}\left(\Lambda|Z\right)\ . \tag{4.16}$$

This joint PDF is further simplified by assuming $P\left(\Lambda|Z\right)$ is independent of Z so that it can be approximated with a marginal PDF. Through this assumption, Eq. (4.16) can be expressed as

$$\widetilde{P}\left(Z,\Lambda\right)=\frac{\overline{\rho}}{\rho}\widetilde{P}\left(Z\right)\widetilde{P}\left(\Lambda\right)\ . \tag{4.17}$$

In this form, different families of statistical distributions can be prescribed separately as

the presumed PDFs for Z and Λ. Some of the presumed PDFs utilized in this work may be dependent on higher order moments of the filtered scalar that need to be modeled in LES. The specific statistical distribution and modeling approach for higher order moments are presented in the following sections.

4.1.2.2 Sub-grid Scale Model for Mixture Fraction

The beta distribution (Gupta & Nadarajah, 2004) is often employed as the presumed PDF for the mixture fraction. Previous studies by Cook & Riley (1994), Jiménez *et al.* (1997) and Wall *et al.* (2000) have shown that the distribution of conserved scalars in most turbulent flows can reasonably be approximated by this PDF. However, this approximation, as seen in the experiment by Tong (2001), is less accurate in strongly sheared flows.

The beta distribution can be parameterized by two shape parameters denoted by a and b within the interval $[Z^-, Z^+]$ for a random variable Z as

$$P_\beta\left(Z;a,b\right)=\frac{\Gamma\left(a+b\right)}{\Gamma(a)\Gamma(b)}\left(Z-Z^-\right)^{a-1}\left(Z^+-Z\right)^{b-1}\left(Z^+-Z^-\right)^{1-a-b}\ , \tag{4.18}$$

where Γ is the gamma function. These two shape parameters can be computed using the mean and variance of Z, *i.e*

$$a=\frac{\widetilde{Z}-Z^-}{Z^+-Z^-}\gamma,\quad b=\frac{Z^+-\widetilde{Z}}{Z^+-Z^-}\gamma,\quad \gamma=\frac{\left(\widetilde{Z}-Z^-\right)\left(Z^+-\widetilde{Z}\right)}{\widetilde{Z''^2}}-1\ , \tag{4.19}$$

where the variance of mixture function is defined as

$$\widetilde{Z''^2}=\widetilde{Z^2}-\widetilde{Z}^2. \tag{4.20}$$

So, the solutions of $\widetilde{Z}$ and $\widetilde{Z''^2}$ are required to utilize this presumed PDF in LES. Since $\widetilde{Z}$ is already transported in Eq. (2.45c), only $\widetilde{Z''^2}$ demands additional modeling consideration.

The filtered transport equation of $\widetilde{Z''^2}$ is

$$\frac{\partial \bar{\rho}\widetilde{Z''^2}}{\partial t} + \nabla \cdot \left(\bar{\rho}\widetilde{\boldsymbol{u}}\widetilde{Z''^2}\right) = \nabla \cdot \left(\bar{\rho}\widetilde{\alpha}\nabla\widetilde{Z''^2}\right) + \nabla \cdot \overline{\boldsymbol{\tau}}^{res}_{Z''^2} - 2\bar{\rho}\widetilde{u''Z''} \cdot \nabla\widetilde{Z} - \bar{\rho}\widetilde{\chi}^{res}_{Z} \ , \quad (4.21)$$

where

$$\widetilde{\chi}^{res}_{Z} = 2\widetilde{\alpha}\widetilde{|\nabla Z''|^2}, \quad (4.22)$$

and $\overline{\boldsymbol{\tau}}^{res}_{Z''^2}$ is evaluated following Eq. (4.10). The turbulent scalar transport in form of $\widetilde{u''Z''}$ is modeled using the gradient transport assumption, *i.e.*

$$\widetilde{u''Z''} = -\alpha_t \nabla\widetilde{Z} \ . \quad (4.23)$$

There are alternative methods of estimating $\widetilde{Z''^2}$ in LES. For example, Pierce (2001) developed a model that is based on local equilibrium between production and dissipation of $\widetilde{Z''^2}$. This method is not considered in this work as it requires the determination of dynamic coefficients. Another method proposed Raman *et al.* (2005) and Pera *et al.* (2006), involves solving the transport equation for the square of Z:

$$\frac{\partial \bar{\rho}\widetilde{Z^2}}{\partial t} + \nabla \cdot \left(\bar{\rho}\widetilde{\boldsymbol{u}}\widetilde{Z^2}\right) = \nabla \cdot \left(\bar{\rho}\widetilde{\alpha}\nabla\widetilde{Z^2}\right) + \nabla \cdot \overline{\boldsymbol{\tau}}^{res}_{Z^2} - 2\bar{\rho}\widetilde{\alpha}\left|\nabla\widetilde{Z}\right|^2 - \bar{\rho}\widetilde{\chi}^{res}_{Z}. \quad (4.24)$$

Then, $\widetilde{Z''^2}$ can be obtained using Eq. (4.20) and is algebraically equivalent to Eq. (4.21) after employing gradient transport assumption. However, Kemenov *et al.* (2012) have shown that this equivalence no longer holds after discretization as the discretization errors are not the same for the two equations. The convergence rate for both methods are similar but the results obtained by solving Eq. (4.21) are more likely to satisfy the realizability of $\widetilde{Z''^2}$. Therefore, Eq. (4.21) is utilized here to compute $\widetilde{Z''^2}$ for the PDF closure of the sub-grid mixture fraction.

The sub-grid dissipation rate can be modeled as

$$\widetilde{\chi}_Z^{res} = \frac{C_{\chi z} C_\epsilon}{C_k S c_t} \frac{\alpha_t}{\Delta^2} \widetilde{Z''^2}, \tag{4.25}$$

where the constant $C_{\chi z}$ represents the ratio of the fluid time scale to the scalar time scale while C_ϵ and C_k are model coefficients of the sub-grid scale kinetic energy model developed by Yoshizawa & Horiuti (1985). In this work, the modeling constants are chosen such that $C_{\chi z} = 2$ (Peters, 2000) and the ratio of C_ϵ to C_k is 2 (Ihme, 2007).

4.1.2.3 FPV Model and Extended FPV Model for LES

The FPV model, when first proposed by Pierce & Moin (2004), assumes that the sub-grid fluctuation of the reaction progress variable can be represented by a single non-premixed flamelet. Following this assumption, the presumed marginal PDF for the reaction progress parameter Λ is represented by the delta function $\delta(\cdot)$:

$$\widetilde{P}(\Lambda) = \delta\left(\Lambda - \widetilde{\Lambda}\right) . \tag{4.26}$$

This expression is further simplified by Pierce & Moin (2004) to

$$\widetilde{P}(C) = \delta\left(C - \widetilde{C|Z}\right). \tag{4.27}$$

in the FPV model. In this formulation , this model is relatively simple as higher moments of C are not considered.

However, the restriction of one flamelet per computational cell may not be a reasonable approximation if there are significant events of local flame extinction and re-ignition within the cell. In a highly turbulent combustion environment, the sub-grid scalar dissipation rate can exceed the quenching threshold for period of time long enough to result in the extinction of flames (Hewson & Kerstein, 2002). After an event of flame extinction , the

flame can either be re-ignited by the auto-ignition mechanism or due to the heat transferred from a neighboring burning region. The experiment by Boxx *et al.* (2013) on two different model combustors has lead the conclusion that auto-ignition is an insignificant event in the typical operating conditions for the combustors investigated. Since a model combustor is numerically investigated here, auto-ignition effects are not considered in the flamelet models utilized in this study.

The distribution of extinguished and burning flames within a computational cell is not captured by the PDF used in the original FPV model. As an extension of the FPV model, the beta distribution is employed as the presumed PDF for sub-grid progress variable distribution. In a premixed flamelet model of Vervisch *et al.* (2004), the same PDF has also been utilized as the model for the unresolved reaction progress variable fluctuations. Progress variable distribution with higher order moments may be used to build a more accurate combustion model (Ihme, 2007) but this is beyond the scope of this work.

Similar to the mixture fraction, the use of the beta distribution to approximate $\widetilde{C''^2}$ requires the LES solution of the second moment of progress variable. Therefore, the LES governing equations may include the transport equation of $\widetilde{C''^2}$:

$$\frac{\partial \bar{\rho}\widetilde{C''^2}}{\partial t} + \nabla \cdot \left(\bar{\rho}\widetilde{\boldsymbol{u}}\widetilde{C''^2}\right) = \nabla \cdot \left(\bar{\rho}\widetilde{\alpha}\nabla\widetilde{C''^2}\right) + \nabla \cdot \overline{\boldsymbol{\tau}}^{res}_{C''^2} - 2\bar{\rho}\widetilde{u''C''} \cdot \nabla\widetilde{C} - \bar{\rho}\widetilde{\chi}^{res}_{C} + 2\bar{\rho}\widetilde{\dot{\omega}''C''} \ . \tag{4.28}$$

This equation is similar to Eq. (4.21) but there is an extra source term $2\widetilde{\dot{\omega}''C''}$, which can be evaluated from the flamelet solutions. The turbulent scalar flux is approximated by Eq. (4.10) and the gradient transport assumption is also employed to model the term $\widetilde{u''C''}$. The sub-grid dissipation term is modeled as

$$\widetilde{\chi}^{res}_{C} = \gamma_c \frac{C_{\chi z} C_\epsilon}{C_k Sc_t} \frac{\alpha_t}{\Delta^2} \widetilde{C''^2} \ , \tag{4.29}$$

where the coefficient γ_c is given by:

$$\gamma_c = \frac{\widetilde{\chi}_C^{res}}{\widetilde{\chi}_Z^{res}} \,, \tag{4.30}$$

and γ_c is set to unity.

4.1.2.4 Filtered Tabulated Chemistry LES (F-TACLES) model

The F-TACLES model (Fiorina *et al.*, 2010; Auzillon *et al.*, 2012) assumes that the sub-grid distribution of the progress variable can be estimated from the solutions of laminar premixed flamelets. This is achieved by filtering the 1D laminar premixed flamelet to evaluate the unclosed turbulence terms found in Eq. (2.45d). The filtering of the premixed flame solution $\phi(\xi; Z)$ at different mixture fraction Z is given by

$$\langle \phi | Z \rangle \left(\xi, Z, \Delta \right) = \int_{-\infty}^{+\infty} \phi \left(\xi; Z \right) G_\Delta \left(\xi - \eta \right) d\eta \,, \tag{4.31}$$

where Δ is the filter width and G_Δ is a Gaussian filter:

$$G_\Delta \left(x \right) = \left(\frac{6}{\pi \Delta^2} \right)^{1/2} \exp \left(-\frac{6x^2}{\Delta^2} \right) \tag{4.32}$$

The PDF of progress variable is implicitly defined by the filtering of 1D premixed flame solutions. Outside the mixture fraction range where premixed flames can exist, the values are interpolated using the closest flame and the non-reacting solution at $Z = 0$ or $Z = 1$. The progress variable, by construction, is monotonic on ξ so the physical coordinate ξ can be replaced with the normalized progress variable, c:

$$\langle c | Z \rangle = \frac{\langle C | Z \rangle - C_u(Z)}{C_b(Z) - C_u(Z)} \,. \tag{4.33}$$

The beta distribution is also employed in the F-TACLES as the presumed PDF for sub-grid mixture fraction distribution. The filtering of the premixed flamelet solutions ϕ, after the convolution with the presumed PDF of Z, yields

$$\overline{\phi}\left(\widetilde{Z},\widetilde{Z''^2},\overline{c},\Delta\right)=\int_0^1\langle\phi|Z\rangle\left(\langle c|Z\rangle,Z,\Delta\right)\beta\left(Z',\widetilde{Z},\widetilde{Z''^2}\right)dZ\ , \tag{4.34}$$

where

$$\overline{c}=\int_0^1\langle c|Z\rangle\beta\left(Z,\widetilde{Z},\widetilde{Z''^2}\right)dZ\ . \tag{4.35}$$

Similarly, Favre filtered thermo-chemical quantities are computed as

$$\widetilde{\phi}=\frac{1}{\overline{\rho}}\int\langle\rho\phi|Z\rangle\beta\left(Z,\widetilde{Z},\widetilde{Z''^2}\right)dZ. \tag{4.36}$$

Since the non-normalized progress variable $\widetilde{C}$ is solved in LES, it is more convenient to tabulate the filtered quantity in terms of $\widetilde{C}$, $\widetilde{Z}$, $\widetilde{Z''^2}$ and Δ. Moreover, a constant Δ has been used here, leading the mapping:

$$\widetilde{\phi}=\mathcal{G}_{FTACLES}\left(\widetilde{Z},\widetilde{Z''^2},\widetilde{C}\right)\ . \tag{4.37}$$

Due to the effect of filtering, the premixed flame modeled with the F-TACLES approach is thicker compared than the original unfiltered flame. This property of the model allows the flame to be resolved in LES but the sub-grid scale wrinkling of the premixed flame is neglected when solving for the thicker flame. To model this phenomenon, the wrinkling factor, Ξ is defined as

$$\Xi=\frac{S_t}{S_l}\ , \tag{4.38}$$

where S_l and S_t are the laminar and turbulent flame speed, respectively. The wrinkling factor is evaluated in the LES calculations using the model proposed by Charlette *et al.* (2002). The diffusion terms and source terms of the progress variable transport equation is

multiplied with the factor Ξ, yielding

$$\frac{\partial \bar{\rho}\widetilde{C}}{\partial t} + \nabla \cdot \left(\bar{\rho}\widetilde{\boldsymbol{u}}\widetilde{C}\right) = \nabla \cdot \left(\Xi \rho \alpha_c \nabla \widetilde{C}\right) + \nabla \cdot \overline{\boldsymbol{\tau}}_C^{res} + \Xi \bar{\rho}\widetilde{\dot{\omega}_C}. \tag{4.39}$$

Instead of utilizing Eq. (4.10), the scalar turbulent flux $\nabla \cdot \overline{\boldsymbol{\tau}}_C^{res}$ is approximated as

$$\nabla \cdot \overline{\boldsymbol{\tau}}_C^{res} = \Xi \Omega_c + \nabla \cdot \left(\Xi \bar{\rho} \alpha_c \nabla \widetilde{C}\right), \tag{4.40}$$

where

$$\Omega_c = \overline{\rho_u S_l \frac{\partial C}{\partial \xi}} - \overline{\rho_u S_l} \frac{\partial \widetilde{C}}{\partial \xi}. \tag{4.41}$$

and ρ_u is the unburnt mixture density. The filtered molecular diffusion, $\rho\alpha_c$, is computed as

$$\rho \alpha_c = \frac{\overline{\rho \alpha \frac{\partial C}{\partial \xi}}}{\frac{\partial \widetilde{C}}{\partial \xi}}, \tag{4.42}$$

while the source term is simply evaluated with Eq. (4.35).

4.1.3 Numerical Method

An objective of this work is to investigate a flame in a model combustor using LES. Unstructured meshes are utilized to capture the complex shape of the model combustor. Therefore, the LES solver employed in this work (VIDA) has the capability of solving the set of LES equations shown in Eq. (2.45d) on an unstructured mesh. The approach to discretize the spatial derivatives on an unstructured mesh is discussed in the following section. In addition, this LES solver also utilizes the temporal scheme that is consistent with the "Low Mach Number Approximation" mentioned in Sec. 2.1.1.

4.1.3.1 Spatial discretization

The spatial discretization employed by the VIDA solver belongs to a class of numerical schemes named the finite volume method (FVM). In the finite volume method, volume

integrals are applied to the governing equation shown in Eq. (2.45) on each individual element of the unstructured mesh. Within this formulation, each element/cell can be seen as a control volume and the computation of the numerical flux across the boundary of each control volume is the crux of this discretization method. This scheme is overall conservative if each element pair is given a consistent flux evaluation on the common face.

However, the discrete control volumes that are utilized in the VIDA solver do not correspond to the elements of the original mesh. Instead, the control volumes are defined as elements on the dual mesh. An 2D example of an element of the dual mesh is shown in Fig. 4.1. In the 2D space, each dual element is centered to a node p and is comprised of several sub-triangles Ω_k^{st}. Each of these sub-triangles is spanned by the node vertex p, cell-centered vertex cc and edge-centered vertex ec. In the 3D space, the dual element is also centered to the node vertex but is a combination of sub-tetrahedrons instead. Ham *et al.* (2006) have shown that the FVM scheme based on the dual mesh is able to capture the wall profile of a turbulent flow more accurately than the cell-centered FVM scheme.

To ease discussion, the spatial terms in Eq. (2.45) are separated into pressure terms, advection terms, diffusion terms and source terms. The interpolation of pressure is treated carefully using the procedure outlined by Ham & Iaccarino (2004) to prevent pressure decoupling caused by collocated variables storage in the VIDA solver. In reacting flows, source terms are results of chemical reactions, with the production term of C being an example. Since chemical source terms are not functions of spatial derivatives, they are computed as simple averages of values on the vertices.

The advection process is the transport of quantities by fluid velocity and its flux term has the form of $\nabla \cdot (\rho \boldsymbol{u} \phi)$. The area integrated advection term, after invoking the Green-Gauss theorem,

$$\int_{\sum_k \Omega_k^{st}} \nabla \cdot (\rho \boldsymbol{u} \phi)\, dA \approx \sum_k \left(\rho_{cc}\phi_{cc}\boldsymbol{u}_{cc} + \rho_{ec}\phi_{ec}\boldsymbol{u}_{ec}\right) \frac{\hat{\boldsymbol{n}}_k}{2}, \tag{4.43}$$

where $\hat{\boldsymbol{n}}_k$ is the length-weighted outward normal of the k-th edge of the dual control volume. Note that Eq. (4.43) requires the evaluation of variables on the points cc and ec but

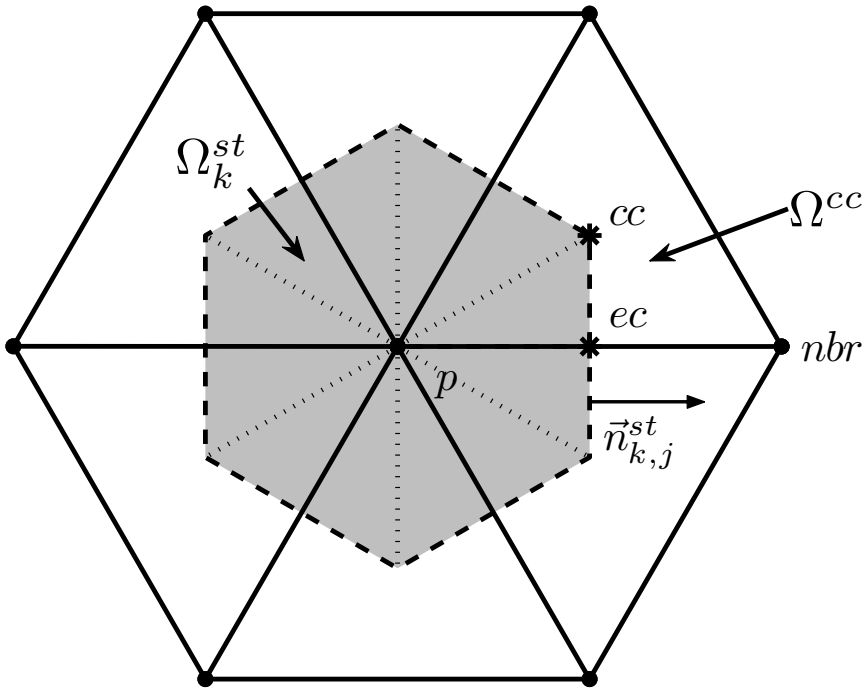

Figure 4.1: A schematic showing an element of the 2D dual mesh (shaded in grey) for an unstructured mesh.

the state variables are only solved on the node p. Therefore, they are interpolated on the vertices cc and ec using the values of neighboring nodes. The interpolation weights utilized in the solver are not upwind-biased so that the advection scheme has minimal numerical diffusion.

Diffusion is a transport process driven by the gradient of quantities and is generally represented by the flux term $\nabla \cdot (\mu \nabla \phi)$. The Green-Gauss theorem is also used here to express the integrated diffusion flux as

$$\int_{\sum_k \Omega_k^{st}} \nabla \cdot (\rho \boldsymbol{u} \phi)\, dA = \sum_k \oint_{\partial \Omega_k^{st}} \mu \nabla \phi \cdot \hat{\boldsymbol{n}}_k ds, \tag{4.44}$$

where $\nabla \phi$ is approximated as

$$\nabla \phi \approx \frac{\oint_{\partial \Omega_k^{st}} \phi \hat{\boldsymbol{n}} ds}{A_k}. \tag{4.45}$$

The closed loop integrals of sub-triangles appearing in Eqs. (4.44) & (4.45) are approximated by applying the midpoint rule on each edge of the individual sub-triangle.

4.1.3.2 Temporal Scheme

The time-advancement of Eq. (2.45) is based on the fractional time stepping method of Kim & Moin (1985) and the subsequent extension to variable density flow by Pierce (2001). In the variable density version, velocity is solved at time levels (n,$n+1$,...) while density, pressure, thermo-chemical scalars are stored on staggered time levels ($n+1/2$,$n+3/2$,...). The scheme, suggested by Ham (2007), consists of the following steps.

1. Predictor step:

   The mass fluxes and the scalar values are linearly extrapolated to their respective next time level using the solutions at current and previous time levels.

2. Density update:

   The density is retrieved from the flamelet library using the extrapolated scalar values.

3. First Poisson equation:

   The extrapolated mass fluxes are corrected by solving a Poisson equation such that the discrete continuity equation is satisfied.

4. Advancement of scalar transport and momentum equation:

   Using the corrected quantities and the solutions on the current time level, the mass fluxes and the scalar values are linearly interpolated to their respective half time-step. The spatial terms of Eqs. (2.45d) & (2.45c) are evaluated by applying the discretized operator to the interpolated values on the half time-step. Then, the momentum and scalars are advanced to the next time level as

$$V\frac{\rho^{n+1}\hat{\boldsymbol{u}}^{n+1}-\rho^{n}\boldsymbol{u}^{n}}{\Delta t}=RHS_{\boldsymbol{u}}^{n+1/2}\,, \tag{4.46}$$

$$V\frac{\rho^{n+3/2}\phi^{n+3/2}-\rho^{n+1/2}\phi^{n+1/2}}{\Delta t}=RHS_{\phi}^{n+1}\,, \tag{4.47}$$

   where $\hat{\boldsymbol{u}}$ is the intermediate solution of velocity.

5. Second Poisson equation:

   Another Poisson equation is solved to correct the mass fluxes that are obtained by solving the momentum equation. In addition, the pressure is also advanced to the next time level in this stage.

4.2 Setup and Configuration

4.2.1 Experiment Configuration

In this work, we consider the gas-turbine model combustor (GTMC) that was experimentally investigated by Weigand *et al.* (2006) and Meier *et al.* (2006). A schematic of the burner is illustrated in Fig. 4.2a. The injector consists of a central air nozzle, an annular fuel nozzle, and a co-annular air nozzle. Both air nozzles supply swirling air at ambient

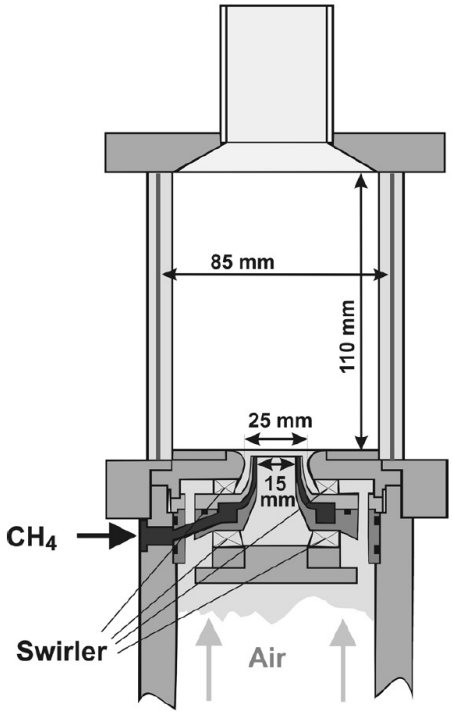

(a) Schematic drawing of GTMC published by Weigand *et al.* (2006).

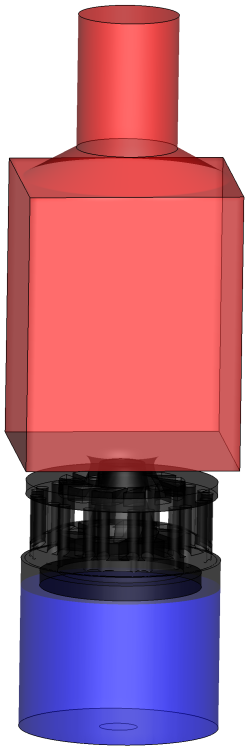

(b) 3D rendering of the fluid volume.

Figure 4.2: Illustration of the GTMC in schematic drawing (left), showing the dimensions of the combustion chamber, the dual swirlers configuration as well as the injection locations of fuel and air. The fluid volume of GTMC rendered in 3D (right); the plenum, swirlers and combustion chamber are shaded in blue, black and red, respectively.

condition from a common plenum. The inner air nozzle has a diameter of 15 mm; the annular nozzle has an inner diameter of 17 mm and an outer diameter of 25 mm. Non-swirling fuel is provided through three exterior ports attached to the annular nozzle. The exit plane of the central air nozzle and fuel nozzle lies 4.5 mm below the exit plane of the outer air annulus. The combustion chamber has a rectangular cross section of 85 mm in width and 110 mm in height. The exit of the combustion chamber is an exhaust tube with a diameter of 40 mm and a height of 50 mm.

Three different operating conditions were considered in the experimental investigation of Weigand *et al.* (2006) and Meier *et al.* (2006). These conditions produce flames of different characteristics and the parameter of the three flames are summarized in Tab. 4.1.

	$\dot{m}_{\text{air}}$ (g/min)	$\dot{m}_{\text{CH}_4}$ (g/min)	P_{th} (kW)	Φ_{glob}	Z_{glob}	Re
A	1095	41.8	34.9	0.65	0.0365	58,000
B	281	12.3	10.3	0.75	0.0418	15,000
C	281	9.0	9.0	0.55	0.0310	15,000

Table 4.1: Parameters of the three flames investigated by Weigand *et al.* (2006) and Meier *et al.* (2006); where $\dot{m}$ is the inlet mass flow rate, P_{th} is the thermal power, Φ_{glob} is the global equivalence ratio, Z_{glob} is the global mixture fraction, Re is the nozzle Reynolds number based on the cold inflow properties.

Due to the vortex breakdown induced by the swirling flow, all three flames are cone-shaped with an inner recirculation zone (IRZ) along the centerline. An outer recirculation zone (ORZ) is also located at lower corner of the combustion chamber. Among these three flames, flame B has largest conical opening angle making this flame seems flatter than flames A and C. Flames A and C can be described as V-shaped as their opening angles are more acute. The flatter flame structure of flame B also corresponds to an earlier burnout of the reactants. Weigand *et al.* (2006) suggested that this property of flame B is related to thermo-acoustic oscillations of this flame.

Despite these differences, all three flames are lifted from the injection nozzle. Between the flame liftoff location and the injector, some amount of fuel and air are mixed so that these three flames can be considered as partially premixed. In addition, Raman measurements of Meier *et al.* (2006) indicate that substantial samples of partially reacted mixture are present in the shear layer between the IRZ and injected gas stream. Meier *et al.* (2006) have suggested that the local flame extinction and ignition delay may be the factors leading to formation of the partially reacted mixtures. A subsequent experiment by Boxx *et al.* (2013) on flame B seems to show that the flame wrinkling processes are more common than the auto-ignition events in this flame.

The operating condition of flame A is investigated in this numerical study as its power output is representative of a combustor used in aerospace applications. At these inlet conditions, Weigand *et al.* (2006) reported that this flame does not demonstrate thermo-acoustics instability. Besides the reacting case, the isothermal counterpart of flame A was also com-

puted with LES to assess the meshing requirement for the swirler and plenum. Aside from the lack of reaction, the non-reacting case also differs from flame A by having air injected through both inlet nozzles. The mass flow rate through the central air nozzle and the annular fuel nozzle, are the same as the values utilized by Widenhorn *et al.* (2009*b*): 19.74 g/s and 1.256 g/s, respectively.

In the numerical study of Widenhorn *et al.* (2009*b*), an isothermal flow through the combustor is investigated with the unsteady RANS and scale adaptive simulation (SAS) methods. Both approaches are able to predict the flow features within the combustor, but the results of the SAS calculation show better agreement with the experimental measurements. Subsequently, Widenhorn *et al.* (2009*a*) have utilized the SAS approach with a hybrid EDM and one-step chemistry combustion model and the results also show good agreement with the experiment in lower region of the combustion chamber.

4.2.2 Computational Setup

4.2.2.1 Computational Meshes

The Computer Aided Drawing (CAD) of the GTMC has been made available to us by the experimental group at DLR. In the global Cartesian coordinate system used in the CAD, y represents the axial direction of the burner while x and z are directions parallel to the sides of the combustor chamber. h is defined as the axial distance from the burner face. Gaps found in the combustor assembly have been cleaned up in order to extract the internal fluid volume (shown in Fig.4.2b) within the combustor assembly. A skeletal mesh for this fluid volume is created using a block-structured strategy so that it entirely consists of hexahedral elements. Then, the computational meshes are obtained by locally refining the skeletal mesh in regions of the GTMC that are deemed to be crucial for predicting the flow field accurately. Application of local refinement to the mesh can lead to elements that are no longer purely hexahedral. Specifically, hanging nodes are present along the interfaces between regions of different refinement level. The spatial discretization technique

	Number of elements (in million)			
Mesh name	Plenum	Swirlers	Combustion chamber	Total
I1	0.5	6	1.5	8
I2	2	10	5	17
I3	2	20	21	43
R1	3	10	6	19
T1	0	10	5	15

Table 4.2: Element distribution for the meshes used for the isothermal simulations (I1 ,I2, I3), reacting simulations (R1) and truncated geometry simulations (T1) of the GTMC.

(see Sec. 4.1.3.1) used in the VIDA solver is applicable to the hanging nodes as the dual elements remain well-defined.

Starting from the skeletal mesh, three meshes of increasing element counts are constructed for the isothermal simulation using the local refinement procedure. The number of elements for the three meshes and their distributions in the combustor are summarized in Tab. 4.2. As shown in Tab. 4.2, most of the elements are located in the swirler region of the GTMC. The criterion for refinement is based on the simulation results and is discussed in Sec. 4.3.4. Furthermore, the significant refinement of elements in the swirlers can also be seen in Fig. 4.3, showing the $z = 0$ planar cuts of the meshes I2 and I3.

In addition to the full geometry of the combustor, we have also considered a truncated burner geometry. Sections of the GTMC have been removed to perform a parametric study on the mass flow rate splits between the two swirlers. This modified burner geometry is shown in Fig. 4.4a along with the corresponding mesh in Fig. 4.4b. From Fig. 4.4a, it can seen that the region starting from the plenum and ending at the entrance of the swirler vanes has been removed in the truncated burner geometry. Nevertheless, the combustor chamber is left unchanged here. The mesh that is utilized for the simulations of the modified burner is essentially a shortened version of mesh R1.

For the reacting simulations, the meshes that were used for isothermal simulation have inadequate resolution in the combustion chamber to resolve the reaction zones. Moreover, the mixing of fuel and air near the fuel injector needs to be resolved for the accurate predic-

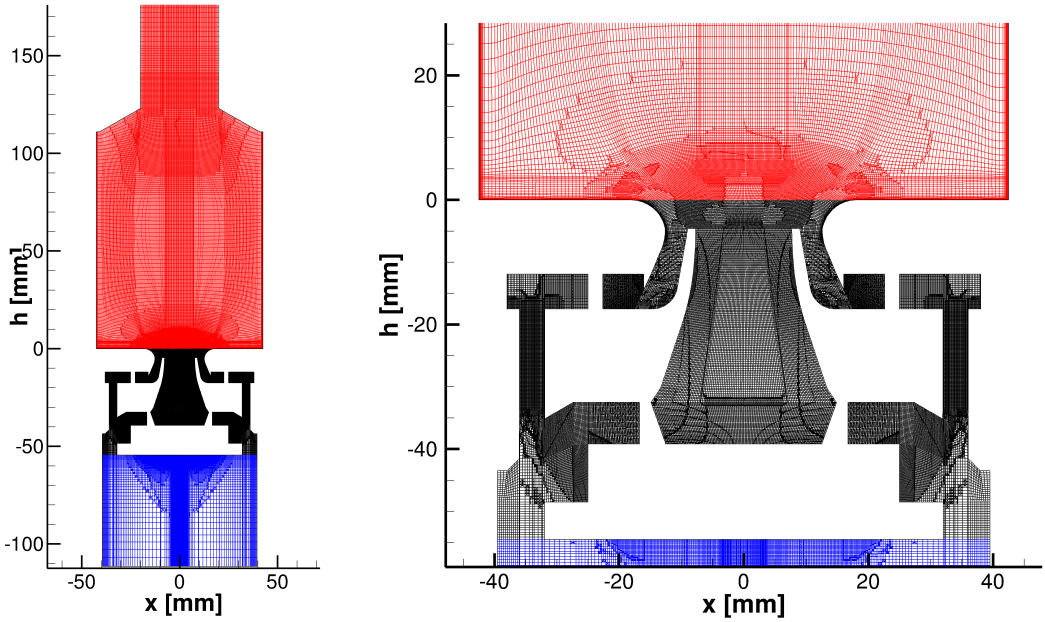

(a) Mesh I2.

(b) Swirler section of mesh I2.

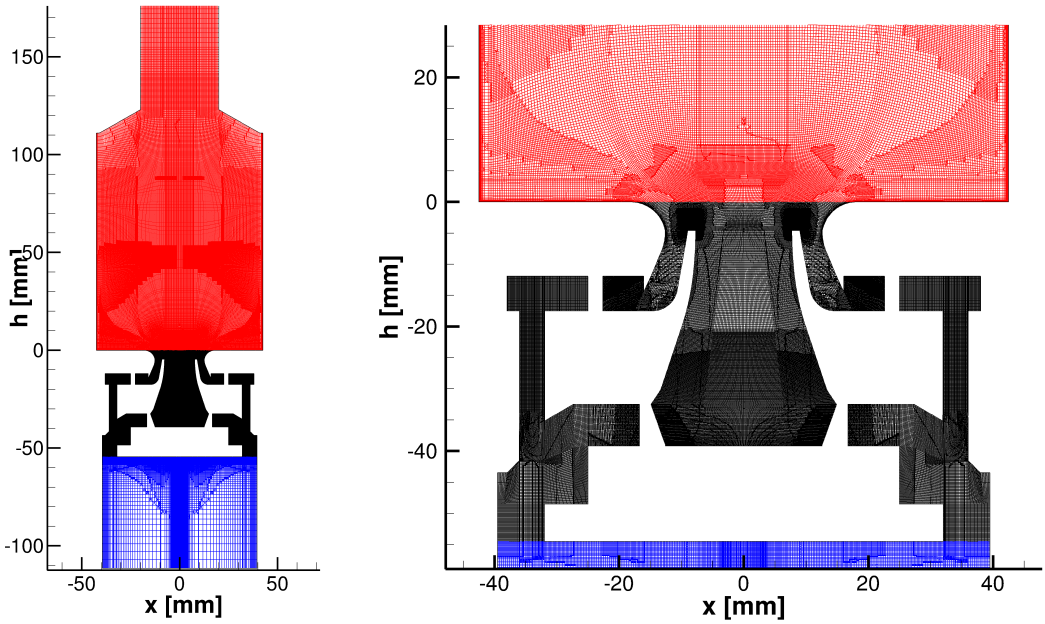

(c) Mesh I3.

(d) Swirler section of mesh I3.

Figure 4.3: Meshes I2 and I3 shown as whole on the left and a view of each mesh on the right to illustrate the grid refinement in the swirler section.

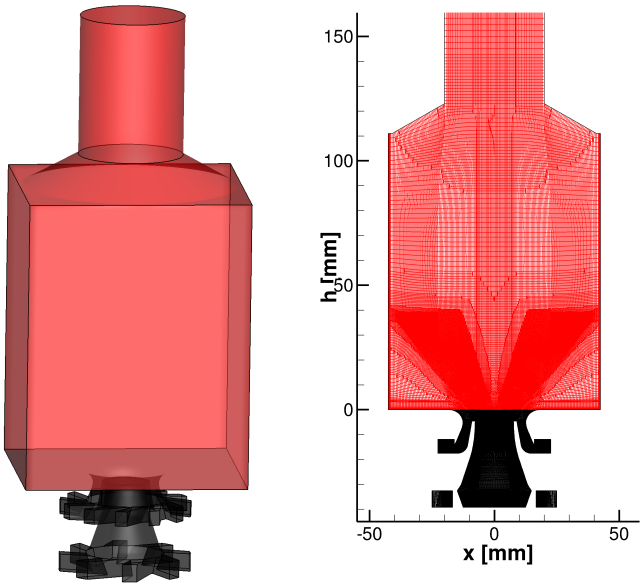

(a) Fluid volume of the truncated burner.

(b) Mesh T1.

Figure 4.4: 3D rendering of the (a) truncated burner geometry and (b) mesh T1 shown as a whole

tion of the partially premixed flames. These two regions of the combustor need to be refined over the isothermal meshes. Based on this requirement, mesh R1 has been generated for the reacting simulations and its characteristics are summarized in Tab. 4.2. The planar cut of the mesh at $z = 0$ is shown in Fig. 4.5 to illustrate the increased element density in the two aforementioned regions.

4.2.2.2 Boundary Conditions

The boundary conditions that require consideration in the GTMC simulations are the burner walls, fuel and air inlets, and the outlet. At the burner walls, the no-slip condition is enforced for the velocities while the Neumann boundary condition is imposed for the transported scalars. In a reacting flow, the enforcement of Neumann boundary condition for scalars at wall boundaries corresponds to adiabatic walls. This is due to the utilization of adiabatic flamelet models in the simulations. The sub-grid variances of the mixture fraction

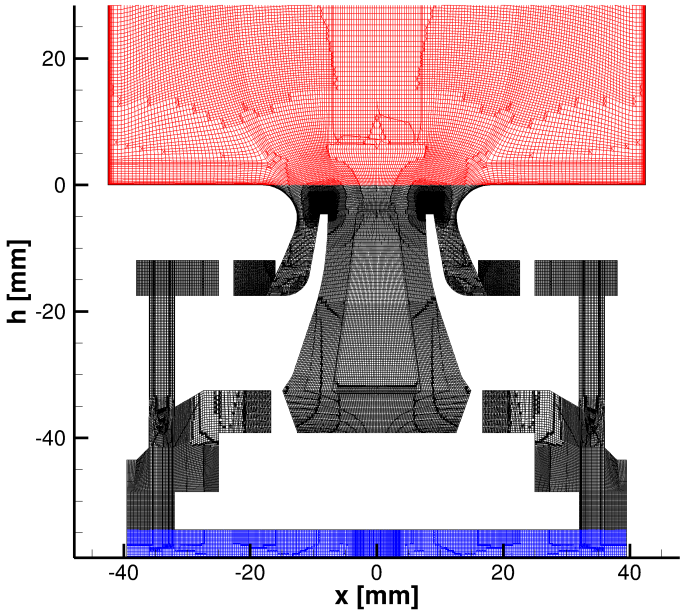

Figure 4.5: Detailed view of mesh R1, showing the increased element density near the fuel injector and the refinement region inside the combustor chamber.

and progress variable, if required by the combustion model, are set to zero at the walls.

Non-fluctuating uniform profiles are employed to describe the velocity normal the to inlet boundaries. The magnitudes of the normal velocity are determined by the mass-flow rate mentioned in Sec. 4.2.1. At the inlets, all scalars except for the mixture fraction are set to zero. The mixture fraction is unity at the fuel inlet and is zero at the air inlet. In the experiment, the fuel is injected into the combustor through a ring of 72 orifices. However, the fuel inlet is simplified to a continuous annular ring in the simulation as the orifices are sufficiently close to each other.

A convective outflow condition is imposed at the outlet of the combustor to ensure that combustion products can be convected out of the simulation domain. In this treatment of the outlet, an convection equation of the state variables ϕ is solved at the outlet instead of

the governing equations in Eq. (2.45). The convection equation is

$$\frac{\partial \widetilde{\boldsymbol{\phi}}}{\partial t} + \widetilde{\boldsymbol{u}}_c \cdot \nabla \widetilde{\boldsymbol{\phi}} = 0, \tag{4.48}$$

$$\widetilde{\boldsymbol{u}}_c = u_c \hat{\boldsymbol{n}}, \tag{4.49}$$

where u_c is the convective speed. The convection speed is evaluated as the average of normal velocity at the outlet. In addition, the outgoing velocity at the outlet is corrected to enforce strict mass balance in the simulation.

4.2.2.3 Chemistry Table Generation

To generate the non-premixed flamelets needed to populate the FPV library, the GRI-MECH 2.11 chemistry mechanism (Bowman *et al.*, 1997) has been utilized in the FLAMEMASTER solver (Pitsch, 1998). The flamelets are solved on 161 grid points in mixture fraction space at a pressure of 1 bar. The boundary conditions for the fuel and oxidizer streams are specified to be methane and air at 300K, respectively. Using these non-premixed flamelets, a 3D FPV table is generated and the size of the table is summarized in Tab. 4.3. Also shown in Tab. 4.3 is the size of the table of extended FPV model (FPV-Cvar). This table is generated with the same set of flamelets but it is 4 dimensional. Due to the larger space that the table needs to span, the number of entries for the variance variables is reduced to keep the table size within the memory limitation of the computers.

The same flamelet solver and chemistry mechanism are also employed to generate the premixed flamelets needed for the application of the F-TACLES model. The premixed flamelets are solved in the physical space and 200 grid points are utilized for the spatial discretization in the premixed flamelet solver. The temperature and pressure of the unburnt mixture are 300 K and 1 bar, respectively. The filter size for the F-TACLES model used this study is 4×10^{-3}m which is approximately 10 times of the flame thickness of the stoichiometric premixed flame for methane-air combustion. The table size for the F-TACLES

Flamelet Model	$N_{\widetilde{Z}}$	$N_{\widetilde{Z''^2}}$	$N_{\widetilde{C}}$	$N_{\widetilde{C''^2}}$
FPV	200	50	200	–
FPV-Cvar	200	10	200	20
F-TACLES	200	50	200	–

Table 4.3: The sizes of chemistry libraries used in the LES of the GTMC for the FPV, FPV-Cvar and F-TACLES models.

table is shown Tab. 4.3.

4.3 Isothermal Flow Results

LES simulations of isothermal condition described in Sec. 4.2.1 are performed on meshes I1, I2, and I3. LES on the three meshes have been calculated using the Vreman turbulence model. The WALE model is also considered in a LES on mesh I2 to assess the sensitivity of this configuration to the turbulence model. The time-step size of these LES calculations is chosen so that the Courant-Friedrichs-Lewy (CFL) condition is close to unity for each mesh. The initial conditions for the LES calculations are obtained by interpolating from the coarser mesh solution. To ensure that the coarser mesh solution is removed from the current simulation, collection of temporal statistics in the LES begins after one flow-through-time after initialization. Note that the flow-through-time of the full combustor, computed from the simulation, is approximately 0.03 s.

4.3.1 Flow Field Structure

The planar mean axial velocity fields at $z = 0$ for the LES computations with the Vreman model on mesh I1, I2, and I3 are shown in Fig. 4.6. Overall, these computations are able to reproduce flow field features observed in the experiment. Specifically, the injector stream from the swirlers is initially separated but re-attaches at the wall at a location further downstream. As a result of this flow separation, an ORZ is formed in the lower corner of the combustion chamber. The vortex breakdown phenomena, induced by the sudden expansion

of the outer swirler nozzle wall, leads to the formation of an IRZ. This IRZ can be seen as a Y-shaped region of negative axial velocity in Fig. 4.6. In short, the flow field within the combustion chamber is characterized by the IRZ, ORZ, and injector stream sandwiched between the recirculation zones.

The precessing vortex core (PVC) can also be seen in the solutions of the LES. The PVC is illustrated in Fig. 4.7a with an iso-surface of pressure. A planar cut of the velocity magnitude field is shown along with the pressure iso-surface to show that the PVC is located in the shear layer between the IRZ and the injection stream. The PVC is a helical hydrodynamic instability that swirling flow is susceptible to (Candel *et al.*, 2014). In the linear stability analysis by Oberleithner *et al.* (2011), this helical instability mode is shown to be absolute unstable. As discussed in Chap. 3, this type of instability can be self-sustaining such that it would prevail even after the triggering perturbations have been removed from the flow. The frequency of the PVC in simulations can be obtained by examining the frequency spectrum of the velocity signal at a point-wise location in the swirler nozzle. The data for spectral analysis are collected from the simulation at sampling rate of 100 kHz for a duration of 0.0135s. The frequency spectrum, illustrated in Fig. 4.7b, is computed by applying Fourier transformation on the instantaneous signal with the mean component removed. This frequency spectrum clearly shows a peak at 1628 Hz, which is the frequency of the PVC and it is consistent with the experimental measurement at a similar mass flow rate (Stöhr *et al.*, 2012).

4.3.2 Statistical Comparison

The statistics for each simulation are collected every time iteration for at least one flow-through-time to ensure sufficient convergence of statistical moments on measurement locations lower than $h = 20$ mm. The temporally averaged velocity results computed from simulations and the corresponding experimental measurements are shown in Fig. 4.8. Overall, the LES results on meshes I2 and I3 are in good agreement with the experimental data.

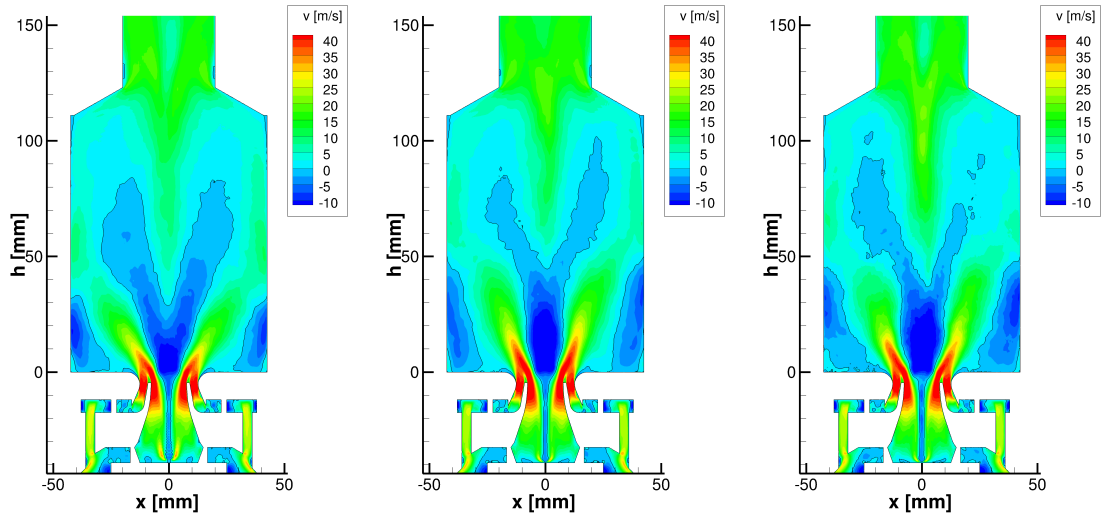

(a) Mean axial velocity on mesh I1. (b) Mean axial velocity on mesh I2. (c) Mean axial velocity on mesh I3.

Figure 4.6: Mean axial velocity on (a) mesh I1, (b) mesh I2, and (c) mesh I3. The iso-line of zero axial velocity is shown as an indicator of recirculation zones.

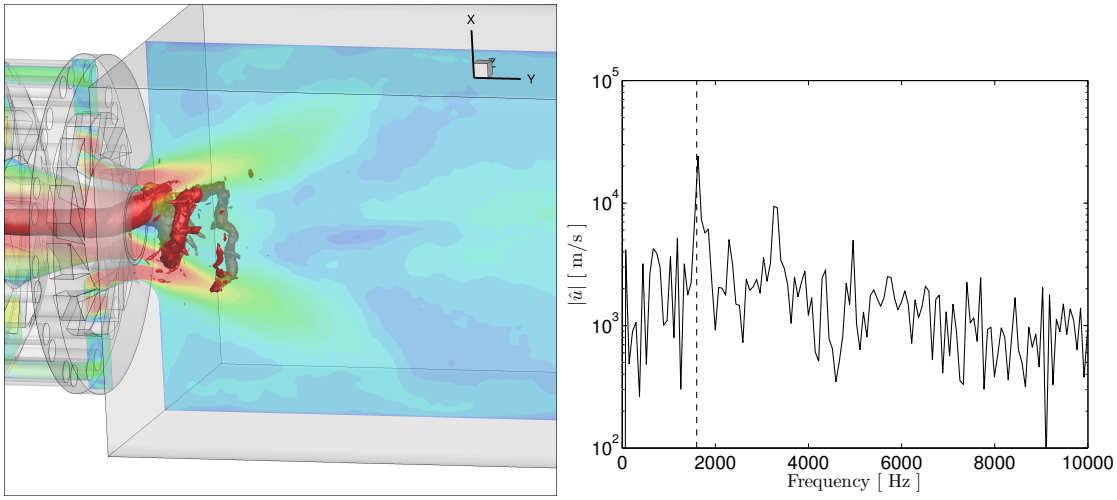

(a) Precessing vortex core

(b) Frequency spectrum of axial velocity at $h = -1.5mm$ and $x = -5mm$

Figure 4.7: PVC visualization by pressure iso-surface (a) and the frequency spectrum (b) showing peak corresponding to the PVC.

However, the LES calculation on the mesh I1 yields an axial velocity profile that is shifted slightly outward in the radial direction at $h = 20$ mm. Nevertheless, the time-averaged LES predictions tend to approach the results of the experiments with increasing mesh resolution. At the last measurement plane of $h = 90$ mm, some discrepancies can be seen in the mean velocity profiles as the statistics might not have converged in time. Excluding this location, this comparison generally shows that the mean results are mostly grid-converged on the refined mesh of I3.

Figure 4.9 shows the resolved root mean squared (rms) statistics of velocity predictions by LES calculations in comparison with experimental measurements. At measurement locations $h = 10$ mm and $h = 20$ mm, the velocity fluctuations obtained from LES calculations on meshes I2 and I3 show excellent agreement with experimental measurements. The LES results on mesh I1 over-predict the fluctuations of velocity at the centerline of these measurement locations. For locations of $h \leq 5$ mm, the peaks of velocity fluctuations are slightly over-predicted by the LES calculations. The predictions of the rms velocity at the centerline show improvements with grid refinement but the velocity fluctuations around $x = \pm 15$ mm remain high even after grid refinement.

The over-prediction of velocity fluctuations may be attributed to the lower turbulent eddy viscosity computed with the Vreman turbulence model. To verify this hypothesis, we consider an additional LES computation which utilizes the WALE model. This LES calculation yields turbulent viscosity that is overall higher than the previous cases. This can be seen from the evaluation of the LES quality indicator discussed in Sec. 4.3.4. As a result, the rms velocity profiles are generally lower in this simulation. Thus, better agreement with experimentally measured fluctuations is obtained at $h = 2.5$ mm and $h = 5$ mm. However, the more diffusive nature of this model also leads to slight under-prediction of velocity fluctuations further downstream. Moreover, the agreement of mean velocities with experimental measurements is degraded with the utilization of the WALE model. Specifically, the peaks of mean velocity profile are shifted inward radially. In the 2D flow field,

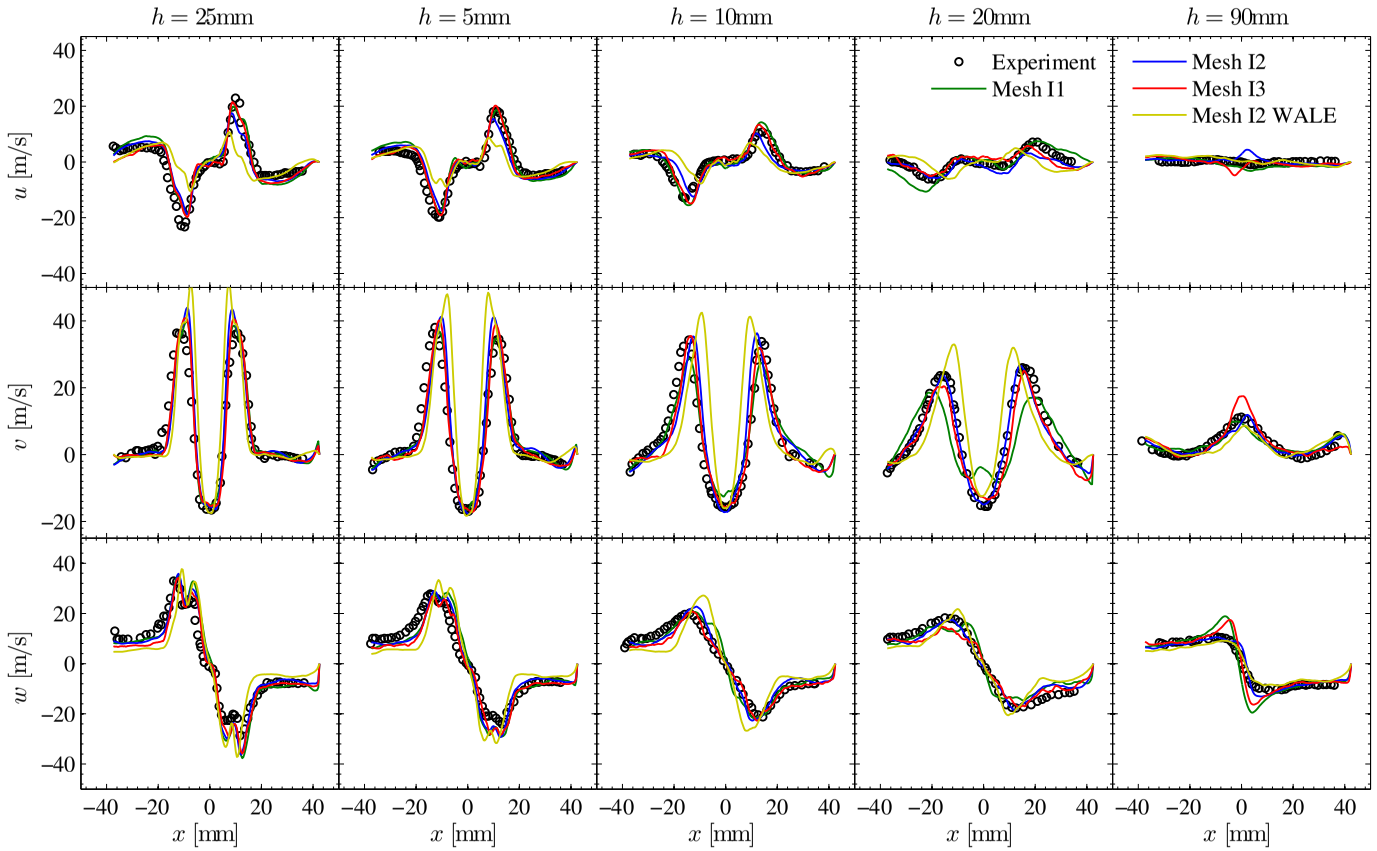

Figure 4.8: Comparison of mean velocity for isothermal simulations with LDV measurements at the cut-plane of $z = 0$. v is axial velocity while u, w represent the radial velocity and tangential velocity in the cut-plane of $z = 0$, respectively.

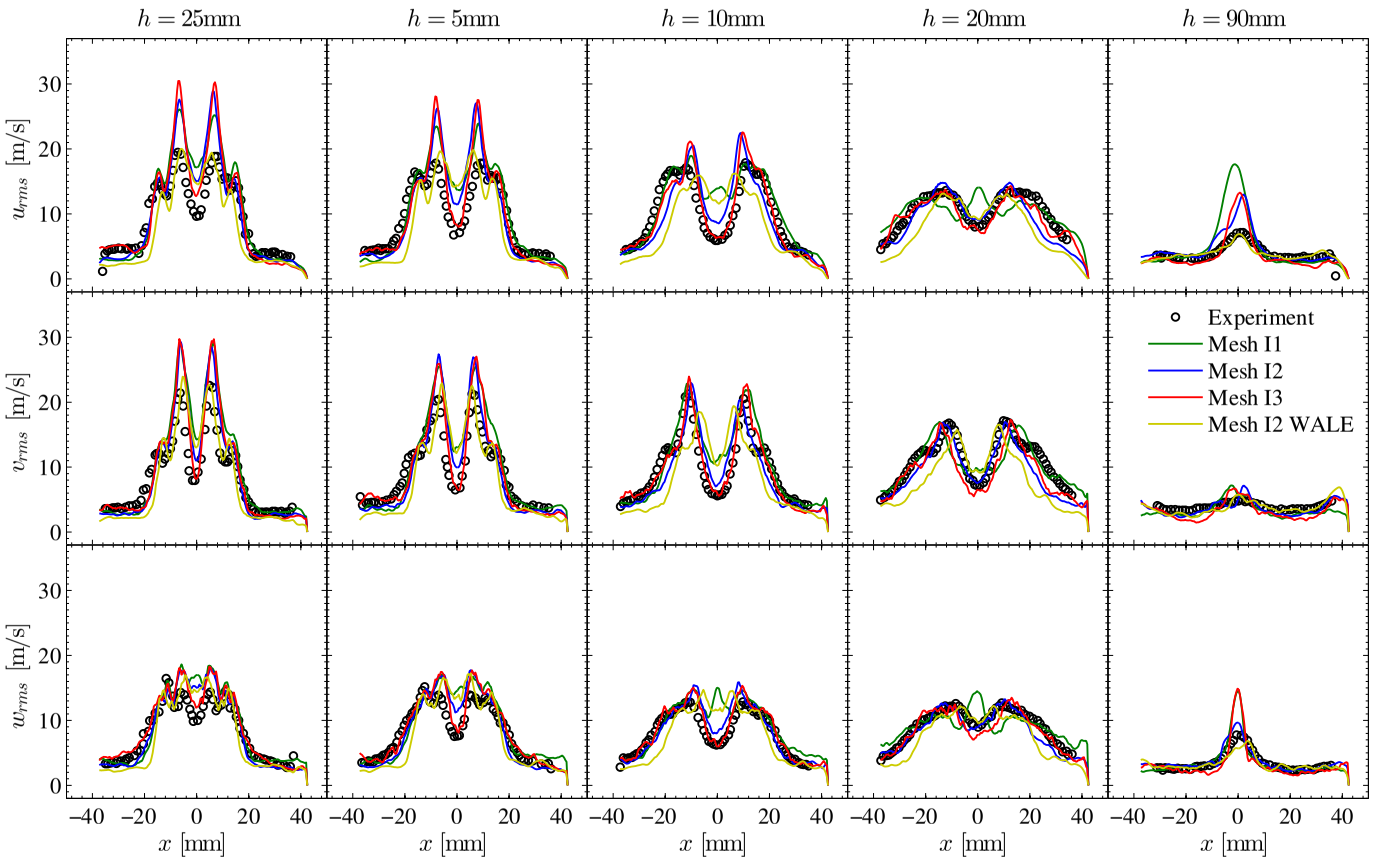

Figure 4.9: Comparison of resolved root mean squared (rms) of velocity for isothermal simulations with LDV measurements at the cut-plane of $z = 0$. v is axial velocity while u, w represent the radial velocity and tangential velocity in the cut-plane of $z = 0$, respectively.

this corresponds to delayed re-attachment of the injector stream to the chamber wall. As a result, the ORZ becomes larger while the IRZ becomes smaller.

4.3.3 Swirl Number and Mass Flow Rate Split

Statistical comparisons, shown in Sec. 4.3.2, are mostly restricted to the flow field inside the combustion chamber but the flow conditions upstream can be crucial in determining the flow dynamics inside the chamber. The split of air mass flow rate between the inner and outer swirlers is characterized. In order to quantify the differences in the upstream conditions for the simulations considered here, we analyze the mass flow rate split between the inner and outer swirlers. The mass flow rate ratio $\dot{m}_r$ is defined as

$$\dot{m}_r = \frac{\dot{m}_{out}}{\dot{m}_{in}}, \tag{4.50}$$

where $\dot{m}_{in}$ and $\dot{m}_{out}$ are the mass flow rates through the inner and outer swirler, respectively.

The swirl number is a characterization of the degree of swirl in a flow and is a crucial parameter in the investigations of swirling flows. When first introduced by Chigier & Beér (1964), it was defined as

$$S_{CB} = \frac{H_{tg}}{H_{ax}} = \frac{\int \rho W U r dA}{R \int \rho \left(U^2 + P\right) dA}\ , \tag{4.51}$$

where H_{tg} is the tangential momentum flux, H_{ax} is the axial momentum flux, r is the radial position, R is the outer radius, W is the azimuthal velocity, U is the axial velocity, and p is pressure. Due to the difficulty in obtaining static pressure measurements to calculate the axial momentum in the swirl generators, this ratio was simplified by Beér & Chigier (1972)

Mesh	Turbulence Model	$\dot{m}_r$	Swirl number		
			Inner	Outer	Total
I1	Vreman	1.51	0.422	0.945	0.714
I2	Vreman	1.44	0.396	0.903	0.671
I3	Vreman	1.50	0.400	0.904	0.676
I2	WALE	1.27	0.371	0.823	0.600

Table 4.4: The swirl numbers and mass flow rate ratios of LES calculations on mesh I1, I2, and I3.

to the more commonly utilized expression of swirl number S, *i.e.*

$$S = \frac{\int \rho \left(Wr\right) U dA}{R \int \rho U U dA} \ . \tag{4.52}$$

The swirl number corresponding to each swirler has been evaluated individually at $h = -5.5$ mm. This location lies below the fuel injectors where the inner and outer swirler streams have yet to be merged. By computing the swirl numbers separately for each stream, the inner and outer swirl numbers can be obtained. The total swirler number is evaluated at $h = 4.5$ mm where the flow has merged into a single stream of mixture.

The swirl numbers and mass flow rate ratios of the isothermal simulations are shown in Tab. 4.4. The table shows that the LES calculations on meshes I2 and I3 predict similar swirl numbers but the $\dot{m}_r$ of the LES solution on mesh I2 is lower than that of mesh I3. Although the simulations on meshes I1 and I3 predict similar $\dot{m}_r$, the swirl numbers are higher in mesh I1. As the vortex breakdown dynamics can be dependent on the degree of swirl of a flow (Billant *et al.*, 1998), the higher swirl number may explain the larger IRZ predicted by the simulation on mesh I1.

The simulation computed with the WALE model shows a considerably lower mass flow rate ratio and swirl numbers than the other simulations. The lower mass flow rate ratio indicates a higher mass flow rate through the inner swirler. This may lead to a total lower swirl number as the inner swirler seems to generate less swirl. Moreover, the individual swirl numbers of the two swirlers are generally lower for this simulation. These visible

differences in the upstream conditions may be the reason for the shifted mean flow profiles. The effects of the mass flow split on the flow field inside the combustion chamber are further investigated in Sec. 4.3.5.

4.3.4 LES Quality

Pope (2004) proposed a criterion to evaluate the quality of LES calculations. This criterion $M(\boldsymbol{x}, t)$, referred to as Pope's criterion, is defined as

$$M(\mathbf{x}, t) = \frac{k_r(\mathbf{x}, t)}{K(\mathbf{x}, t) + k_r(\mathbf{x}, t)}, \tag{4.53}$$

where $K(\mathbf{x}, t)$ is the resolved turbulent kinetic energy and $k_r(\mathbf{x}, t)$ is the turbulent kinetic energy captured by the turbulence model. The value of M is bounded between 0 and 1, and $M = 0$ corresponds to a fully resolved simulation (DNS) while $M = 1$ corresponds a simulation in which the turbulence is fully modeled, *e.g.* RANS.

The resolved turbulent kinetic energy can be obtained in LES by evaluating the temporal statistics of velocity, but k_r is usually approximated using models. By dimensional argument, k_r can be approximated as

$$k_r = \left(\frac{\nu_t}{\Delta C_k} \right)^2 . \tag{4.54}$$

ν_t can be evaluated with the same sub-grid scale turbulence models mentioned in Sec. 4.1.1, and C_k is a model coefficient.

If ν_t is obtained using the classical Smagorinsky model (see Eq. (4.2)), then k_r can approximated as

$$k_r = 2 C_I \Delta^2 \left\| \underline{\widetilde{S}} \right\|^2 , \tag{4.55}$$

where C_I is a model constant that can range from $\frac{1}{\pi^2}$ to 0.01 (Sagaut, 2006). This approximation is commonly used in compressible LES to model terms in the energy equa-

tion (Moin *et al.*, 1991). C_k can obtained by equating Eq. (4.54) with Eq. (4.55), yielding

$$C_k = \frac{C_s^2}{\sqrt{2C_I}} \,, \tag{4.56}$$

where C_s is the Smagorinsky model constant. Assuming C_I is $\frac{1}{\pi^2}$ and C_s is 0.2, C_k is approximately 0.089, which is close to the value computed by Yoshizawa (1986).

Pope's criterion for all isothermal LES calculations are computed with Eq.(4.53) and the planar fields of this quantity at $z = 0$ are shown in Fig. 4.10. In addition, the iso-value lines of the threshold $M = 0.2$ are shown in Fig. 4.10 to delineate the region in the combustor where the large scale turbulence is well-resolved and where it is not. This cutoff value was suggested by Pope (2004) and later adopted by Boudier *et al.* (2007) as a metric to assess the quality of LES.

Overall, the computed values of Pope's criterion in the LES calculations with the Vreman model, are mostly below 0.2 in the interior of the combustion chamber and swirlers. However, this metric also indicates that there is more unresolved turbulence fluctuation near the centerline of the inner swirler nozzle. This is due to the strong rotation of the flow in this area and the tendency of the Vreman model to overestimate the turbulent viscosity in solid body rotation flows (Nicoud *et al.*, 2011). Nevertheless, the grid refinement of this region in mesh I3 seems to reduce Pope's criterion to below threshold.

Pope's criterion is also evaluated for the simulation with the WALE model and is shown in Fig. 4.10. In comparison to the LES with the Vreman model on the same mesh, this LES calculation clearly predicts higher turbulent viscosity. This may indicate that more turbulent fluctuations are resolved in the simulations utilizing the Vreman model However, the comparison with the experimental measurements in Sec. 4.3.2 shows that the Vreman model seems to under-predict the turbulent viscosity. The lower estimation of eddy viscosity by the Vreman model can lead to lower values of k_r, and hence more a favorable field of M. Moreover, the study of Nicoud *et al.* (2011) seems to suggest that the model coefficient

for the Vreman model should be higher than the value used in this study.

The near wall mesh resolution is another metric of the LES mesh quality. To characterize the mesh resolution at the walls of the GTMC, the non-dimensionalized wall distances Δy^+ are evaluated for the simulation on mesh I3. This quantity is computed as

$$\Delta y^+ = \Delta y_{wall} \sqrt{\frac{\nu}{\frac{\partial u_t}{\partial \eta}}}, \tag{4.57}$$

where Δy_{wall} is the distance from the first interior node to the wall. u_t is the wall tangential velocity, η denotes the wall normal direction coordinate, and ν is kinematic viscosity. In order to resolve the turbulent boundary layers, the near-wall mesh needs to be sufficiently fine such that $\Delta y^+ \approx O(1)$.

The approximations of Δy^+ are evaluated on the walls of mesh I3 and the spatial evolution of the mean, minimum value and maximum values are shown in Fig. 4.11 as function of y. Special care has been taken to ensure that Δy^+ is of order unity at the interface section between swirler and the combustion chamber. The separation of flow that occurs at this location is responsible for the formation of the ORZ so it is imperative for the simulation to resolve the boundary layer on the walls here. Other than this region of the combustor, the mean of Δy^+ is approximately $O(10)$, indicating insufficient wall resolution. A wall resolved LES of the GTMC will require a mesh size significantly larger than mesh I3, which is beyond the scope of the current work.

4.3.5 Truncated Combustor

In Sec. 4.3.3, the mass flow rate split between the two swirlers is identified as a possible factor in determining the characteristics of the recirculation zones in the combustor. To this end, we consider LES computations of the truncated burner (shown in Fig. 4.4a) where the mass flow rates through each swirler can be independently varied. Five different mass flow rate ratios, summarized in Tab. 4.5, have been investigated in this study in order to elucidate

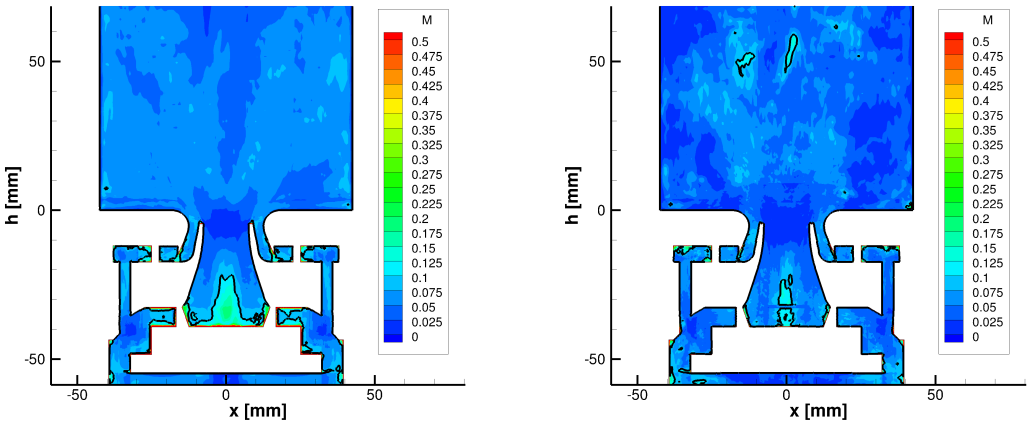

(a) Pope's criterion of LES on mesh I1.

(b) Pope's criterion of LES on mesh I2.

(c) Pope's criterion of LES on mesh I3.

(d) Pope's criterion of LES with WALE model on mesh I2

Figure 4.10: Pope's criterion field of LES calculations. Black lines indicate the constant value of $M = 0.2$.

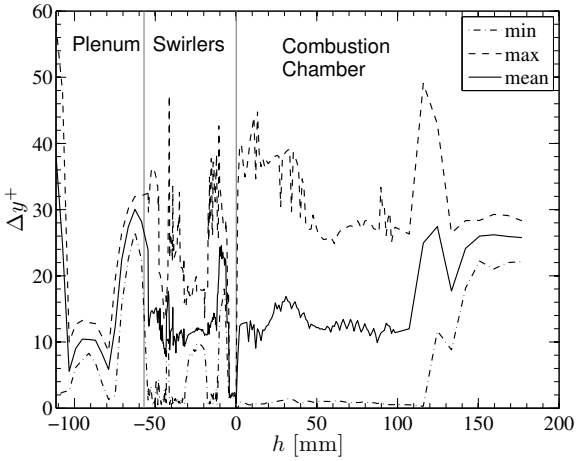

Figure 4.11: Minimum, maximum and mean of Δy^+ evaluated at the wall for mesh I3 as a function of axial location h.

the effects of this parameter on the flow field inside combustion chamber.

The mean axial velocity field for the five simulations of different $\dot{m}_r$ are shown in Fig. 4.12. In the simulations of $\dot{m}_r \leq 1.4$, the injector stream separates from the outer swirler nozzle. With increasing mass flow rate to the outer swirler, the separated flows re-attach to the combustor chamber at locations closer to the bottom wall. For cases of $\dot{m}_r \geq 3.0$, the flow almost never separates from the wall, thus eliminating the ORZ. This finding is consistent with the experimental work of Allison (2013) in which the swirler passage was blocked off to investigate the variation of the flame shape. A V-shaped flame was observed in the experiment when the outer swirler was blocked while a flat flame could be obtained by impeding the flow through the inner swirler.

To quantify the effect of mass flow split between the swirlers, swirl numbers are evaluated as described in Sec. 4.3.3 and are shown in Tab. 4.5. With the exception of the limiting cases of $\dot{m}_r = 0$ and $\dot{m}_r = \infty$, the swirl number of each swirler is relatively insensitive to the variation of mass flow rates. Since the geometry of the swirlers is fixed in this study, it is expected that the degree of swirl imparted by the swirlers remain unchanged. However, the total swirl number of the flow is increased when more air is flowing through the outer swirler. A comparison of the swirl numbers for each swirler reveals that the outer swirler

seems to generate more swirl than the inner swirler. Hence, a mass flow rate split that favors the outer swirler can lead to a larger total swirl number.

Previous studies on swirling flow (Gupta *et al.*, 1984; Beér & Chigier, 1972) have shown that the increase in the strength of swirl can cause a flow transition from a separated swirling jet (Type B flow) into a wall jet (Type C flow). In the truncated geometry of GTMC, the increase in total swirl number is also correlated with the transition to an attached flow. Hence, this flow behavior elucidated through LES is consistent with the finding of previous work of Beér & Chigier (1972). In summary, the mass flow rate split can affect the flow field within the combustor chamber by changing the total swirl number of the flow.

	Swirl number		
$\dot{m}_r$	Inner	Outer	Total
0.0	0.420	0.000	0.407
1.0	0.401	0.945	0.593
1.3	0.397	0.903	0.686
3.0	0.414	0.904	0.869
∞	0.000	0.951	0.961

Table 4.5: Swirl numbers of the truncated burner simulations.

4.4 A Priori Study of Flamelet Models

Since the GTMC operates in a partially premixed combustion mode, we have performed an *a priori* analysis on the experimental measurements to verify whether the premixed or non-premixed flamelets are able to span the thermo-chemical states measured in experiment. To this end, the flamelet tabulation shown in Eq.(2.29) and Eq.(2.31) are applied to the mixture fraction and progress variable values obtained from the experiment of Weigand *et al.* (2006).

Using the experimental measurements of mixture fraction and progress variable, each sample of Raman spectroscopy is projected onto different flamelet manifolds, and thermo-

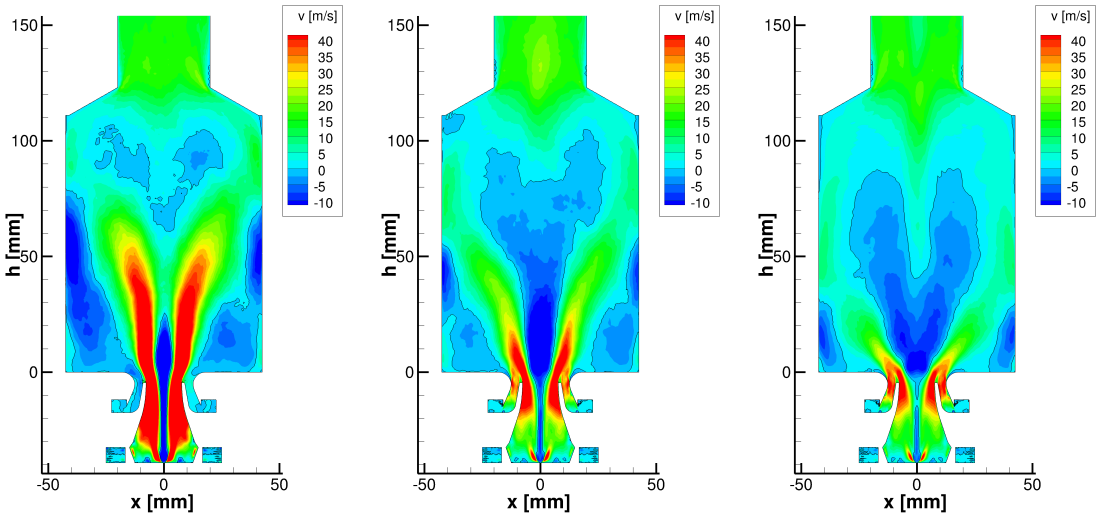

(a) Mean v field of $\dot{m}_r = 0.0$. (b) Mean v field of $\dot{m}_r = 1.0$. (c) Mean v field of $\dot{m}_r = 1.4$.

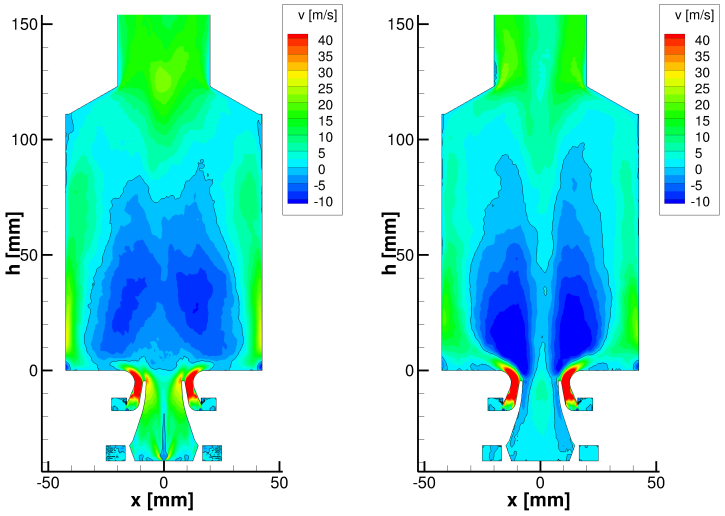

(d) Mean v field of $\dot{m}_r = 3.0$. (e) Mean v field of $\dot{m}_r = \infty$.

Figure 4.12: The mean axial velocity of the truncated burner simulations at different mass flow rate split between the swirlers. Shown in figures are also the iso-line of $v = 0$ to indicate separation and re-attachment of flow.

chemical quantities are evaluated using the respective flamelet table. To ease comparison, the thermo-chemical quantities are statistically conditioned on the mixture fraction. The conditional values are calculated for the measurements as well as for quantities derived from the flamelet solutions. The conditional averages of temperature, Y_{CO}, $Y_{\mathrm{H_2O}}$, and $Y_{\mathrm{CH_4}}$ at several axial locations are shown in Fig.4.13 for comparison.

Overall, Fig.4.13 shows that both the premixed and non-premixed flamelets are adequate in capturing the thermo-chemical states measured in the experiment. Specifically, the temperatures that are retrieved from the flamelet library are in good agreement with the measurements. The same trend is observed for $Y_{\mathrm{H_2O}}$ and $Y_{\mathrm{CH_4}}$ but the derived values of Y_{CO} are slightly higher than the measurements at locations of $h \geq 30mm$. This over-prediction may be attributed to be the faster consumption of fuel in the flamelet models. Nevertheless, this *a priori* investigation seems to suggest that both non-premixed and premixed flamelets can be reasonable models for the combustion process in flame A.

4.5 Reacting Flow Results

The flame A operating condition of the GTMC is computed with LES on the mesh R1. Three flamelet combustion models, FPV, FPV-Cvar, and F-TACLES are considered in this study. The WALE turbulence model is utilized in these LES calculations of the GTMC as the Vreman model assumes a divergence free velocity field in its derivation. The initial conditions for these simulations are the isothermal solution on mesh I2 ignited and time-advanced for at least two isothermal flow-through-times with the FPV model. The evaluation of statistics in LES calculations that utilize combustion models other than FPV begins after two flow-through-time in order to remove the FPV solution from the simulation domain. The statistics are collected for all simulations for a time period of 0.03s. In addition, the time-step sizes of these simulations are limited to 6×10^{-7}s in order to ensure the CFL condition is within the order of unity.

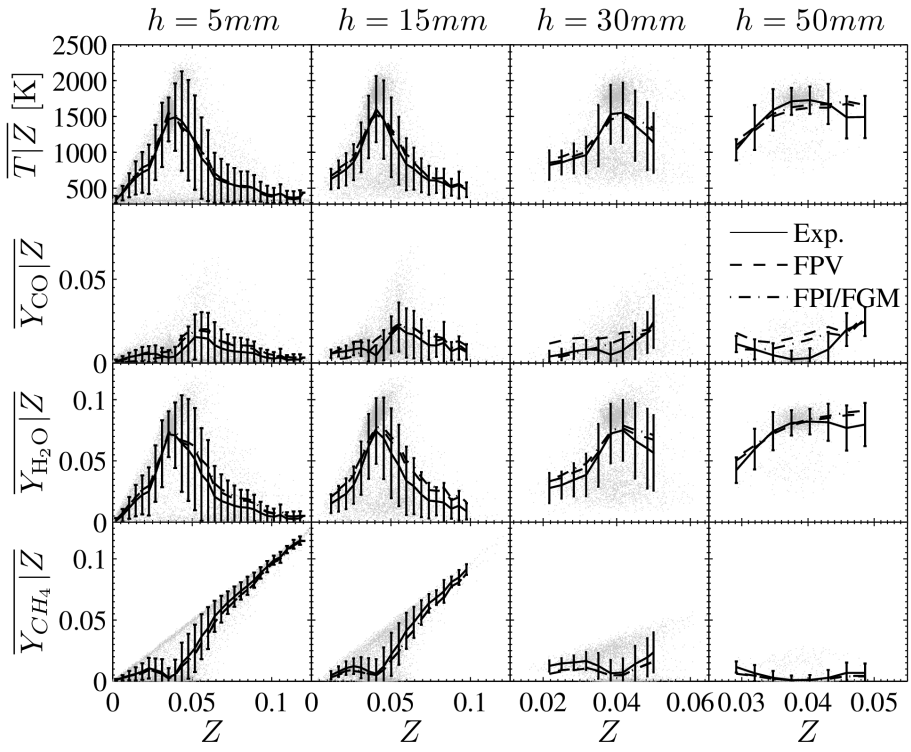

Figure 4.13: Thermo-chemical quantities, conditioned on the mixture fraction space, obtained with the application of the flamelet models on the Raman measurements of Weigand *et al.* (2006) and Meier *et al.* (2006).

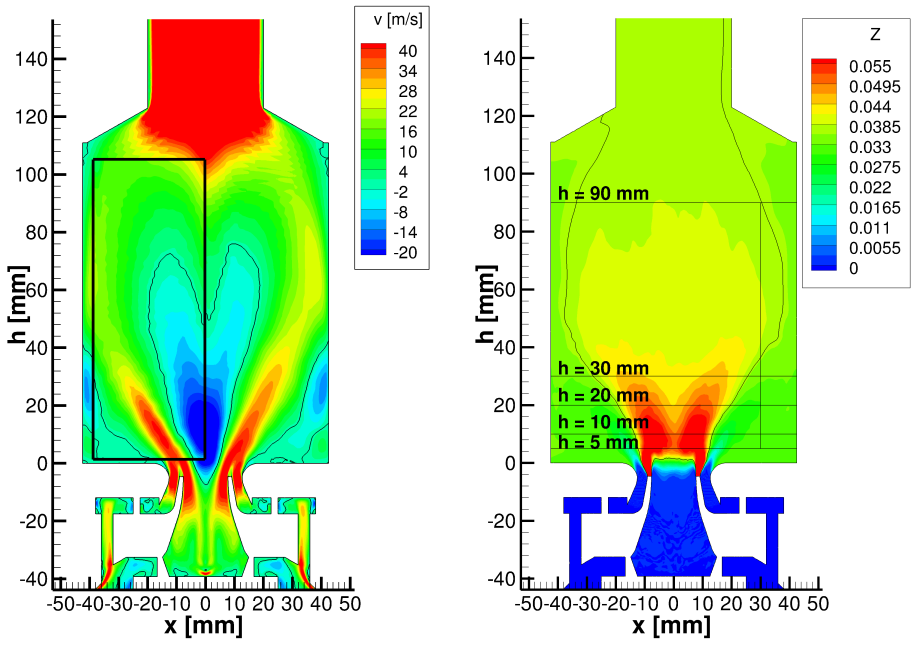

(a) Mean axial velocity field.

(b) Mean mixture fraction field.

Figure 4.14: Mean results at $z = 0$ of the LES utilizing the F-TACLES model. (a) Mean axial velocity field is overlaid with PIV measurement in a box on the left; iso-line of zero axial velocity is shown to indicate recirculation zones. (b) The mean mixture fraction field is shown with the iso-line of global mixture fraction and axial locations for statistical comparison.

4.5.1 Flow Field Structure

The mean axial velocity and mixture fraction fields of the LES utilizing the F-TACLES model are shown in Fig. 4.14. Overall, this flame A simulation retains most of the flow features found in the isothermal simulations. The injector stream is still separated from the combustor walls initially, resulting in a ORZ. The reacting swirling flow in the combustor also experiences vortex breakdown, leading to the formation of IRZ. The mean mixture fraction field, illustrated in Fig. 4.14b, shows that the gas mixture in the IRZ is richer than the mixture in the ORZ. Specifically, mixture fraction within the IRZ is higher than the global mixture fraction (shown in Fig. 4.14b). On the other hand, the mixture in the ORZ is mostly leaner than the global equivalence ratio.

4.5.2 Mean and Root Mean Squared Statistics

The x profiles of the time-averaged velocity for all reacting LES calculations are shown in Fig. 4.15 along with the experimental measurements. Regardless of the underlying combustion models, the LES predictions are in overall reasonable agreement with the experiment. However, the magnitude of the reverse flow along the centerline is over-predicted by all three LES calculations at locations $h \leq 10mm$. This stronger reverse flow manifests as an more elongated IRZ at the flame base. This is further supported by the lower LES prediction of radial velocity at $h \leq 10mm$. The stronger reverse flow and more extended IRZ can also be seen in the comparison of the computed mean axial velocity field with the PIV measurement in Fig. 4.14a. The longer IRZ may be attributed to the higher flame temperature in the ORZ predicted in the simulations, an assertion discussed in following comparison of thermo-chemical quantities. Despite that, the resolved velocity fluctuations of LES, illustrated in Fig. 4.16 , show good agreement with the experimental results. Moreover, the comparison of results for the different LES calculations seems to reveal little or no sensitivity of the velocity fluctuations to the variation in the combustion model.

Fig. 4.17 shows the temporal average of the mixture fraction and temperature profiles along x at several axial measurement locations. Overall, the mixture fraction profiles of the LES calculations are in reasonable agreement with the experimental measurements. Since the mixture fraction transport is mostly controlled by advection and diffusion, the good agreement of velocity predictions with measurements also translates to predictions of the mixture fraction that agree with experimental results. However, the mean mixture fraction values near the axis center are slightly over-predicted by the LES calculations at $h = 5$ mm. The longer IRZ predicted by the simulation recirculates more rich mixture into the inner swirler nozzle, hence leading to the slightly higher mixture fraction at the centerline. As a result, the mean thermal-chemical quantities near the centerline of the simulations also deviates slightly from the experimental measurements.

For most axial locations, Fig. 4.17 shows that the mean temperature profiles of LES

agree reasonably with the experiment. At $h = 5$ mm, the mean temperature profiles show little variation between combustion models. For $x \geq 20$ mm at $h = 5$ mm, the mean temperature profiles obtained from the simulations are slightly higher than the temperature measurement of experiment. This can be attributed to the wall heat loss in the ORZ as the flow is in close vicinity to the walls. Since the adiabatic flamelet models are utilized in this work, the reduction in temperature due to heat loss is not captured in the simulations. This slight over-prediction of temperature at near-wall locations seems to extend up to $h = 30$ mm. The higher temperature in the ORZ may play a role in causing a more elongated IRZ in the simulations but further verification of this claim requires the consideration of wall heat loss effect, which is beyond the scope of this work.

With the exception of $Y_{\mathrm{H_2}}$, insensitivity to the combustion model can also be seen for the mean profile of most species mass fractions at $h = 5$ mm. The mean $Y_{\mathrm{H_2}}$ profile at $h = 5$ mm is over-predicted by the F-TACLES model. This may be attributed the lack of diffusion of the hydrogen gas in the mixture fraction space as the individual premixed flamelets do not interact with each other in the premixed flamelet model. As the mixture becomes more homogeneous further downstream, the agreement of the predicted $Y_{\mathrm{H_2}}$ profiles with experimental measurement improve significantly.

At locations downstream of $h = 5$ mm, the differences in temperature profiles between the premixed and non-premixed models are more apparent. In the ORZ where heat loss effect is non-negligible, the temperature predictions of F-TACLES model shows slightly better agreement with experimental results. Within the IRZ, the temperature prediction by the F-TACLES model is generally higher than that of non-premixed models. Besides that, the utilization of F-TACLES model in the LES also yields mean Y_{CO} values that are lower than experimental measurement.

In comparison to the FPV model, the FPV-Cvar model is able to predict temperature and species mass fraction profiles that show better agreement with the experimental measurements. The mean results of the FPV-Cvar model generally lie between the predictions

of the FPV and the F-TACLES models. This is expected as Meier *et al.* (2006) suggested that local extinction and ignition can be important in the GTMC. The sub-grid scale fluctuations of the reaction progress are accounted for in the FPV-Cvar model with the presumed PDF closure of C while the F-TACLES utilized a premixed flame wrinkling model to capture this phenomenon. The FPV model does not employ any treatment of sub-grid scale fluctuations of reaction progress.

At the final measurement location of $h = 90$ mm, where the flow has reached chemistry equilibrium, the LES results are in excellent agreement with the experimental measurements. Despite the minor difference at locations upstream of $h = 90$ mm, the predicted thermo-chemical state is virtually identical for all combustion models. This may indicate that the major chemical species and temperature in the exhaust of GTMC may be insensitive to the combustion model used. However, combustion exhaust measurements are usually used to validate of numerical codes in more realistic gas turbine combustor. Good agreement with experimental measurements of the exhaust gas may not guarantee that combustion dynamics inside the combustor are well-predicted by numerical simulations.

The resolved rms fluctuations of the temperature, mixture fraction, and the mass fraction of some chemical species are shown Fig.4.18. Overall, the fluctuations of the mixture fraction are well-predicted by the LES calculations. Similarly, the temperature fluctuations of the simulations, although slightly higher at $h = 20$ mm and 30 mm, are in reasonable agreement with that of the Raman measurements. With the exception of the hydrogen species, the rms profiles of species mass fractions fluctuations tend to follow the experimental results. The over-prediction of mean $Y_{\mathrm{H_2}}$ by the premixed model has resulted in higher rms fluctuations of this species mass fraction. The non-premixed models, which do not suffer from this issue, show better agreement with the experiment in terms of the hydrogen mass fraction rms.

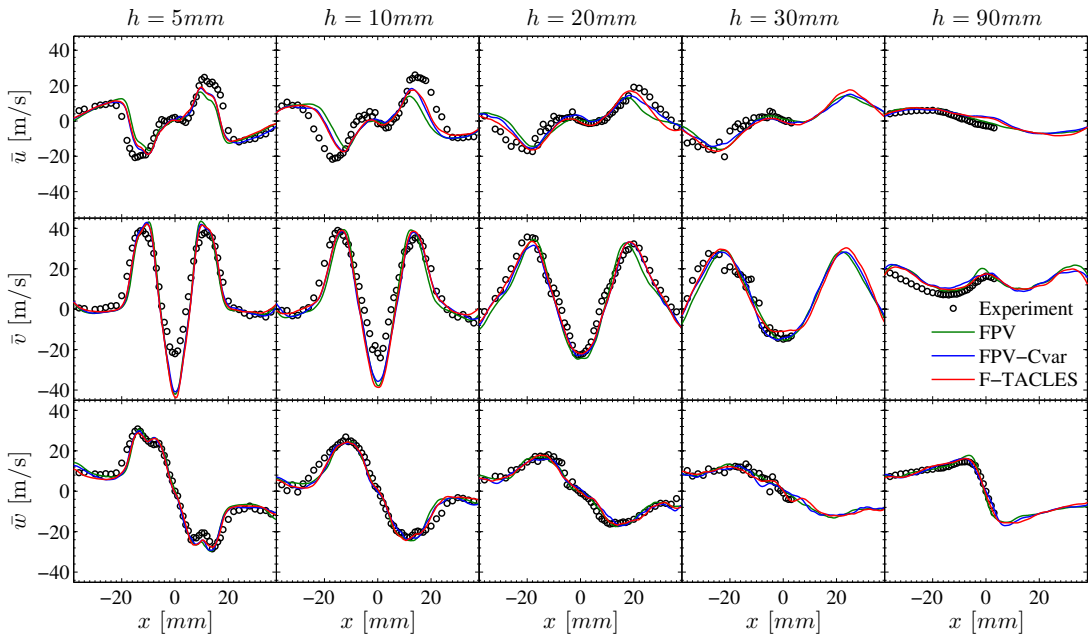

Figure 4.15: Comparison of the mean velocity for flame A simulations with experimental data at the cut-plane of $z = 0$. v is the axial velocity while u, w represent the radial velocity and tangential velocity in the cut-plane of $z = 0$, respectively.

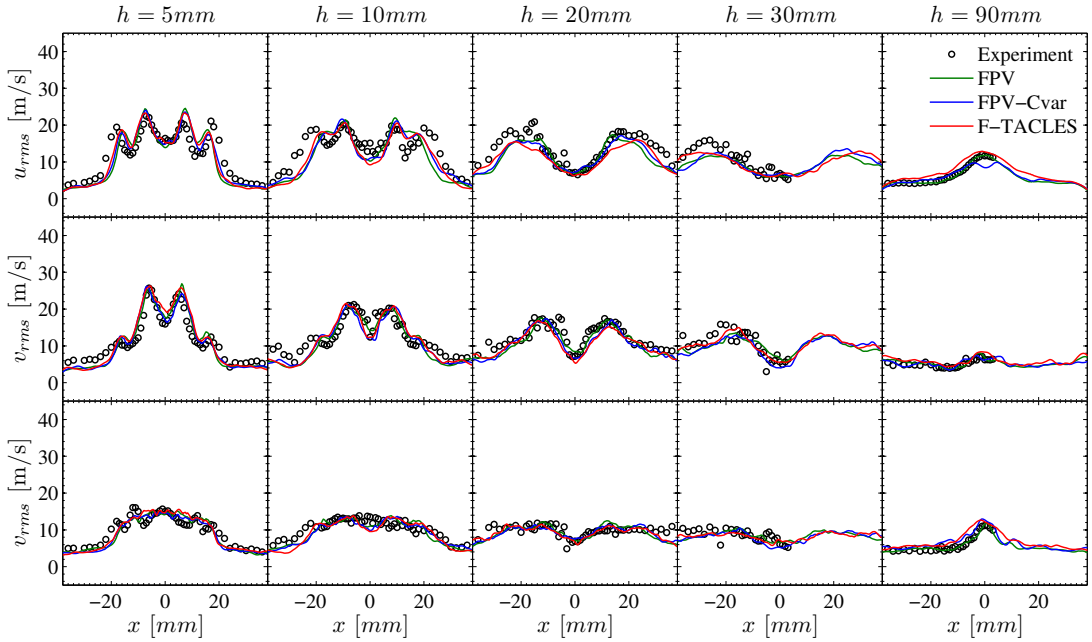

Figure 4.16: Comparison of the resolved root mean squared (rms) of velocity for flame A simulations with experimental data at the cut-plane of $z = 0$. v is the axial velocity while u, w represent the radial velocity and tangential velocity in the cut-plane of $z = 0$, respectively.

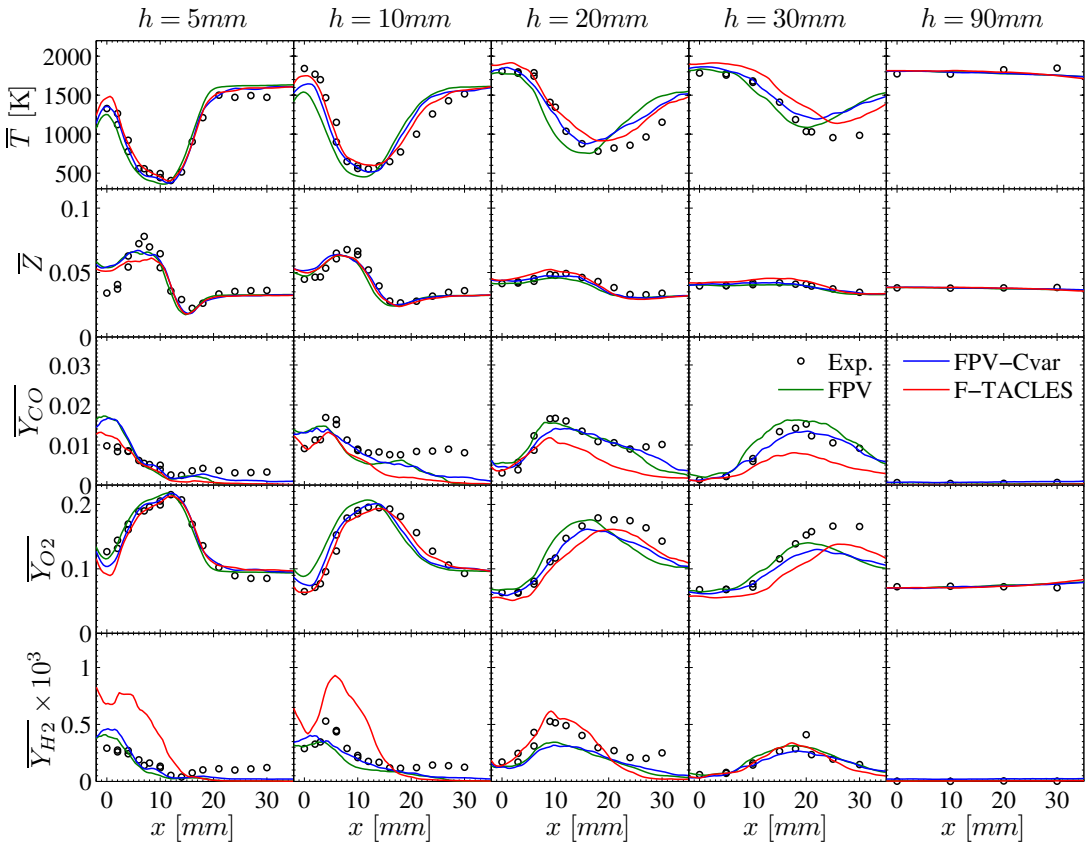

Figure 4.17: Comparison of mean thermo-chemical quantities for flame A simulations with experimental data at several axial locations on the cut-plane of $z = 0$.

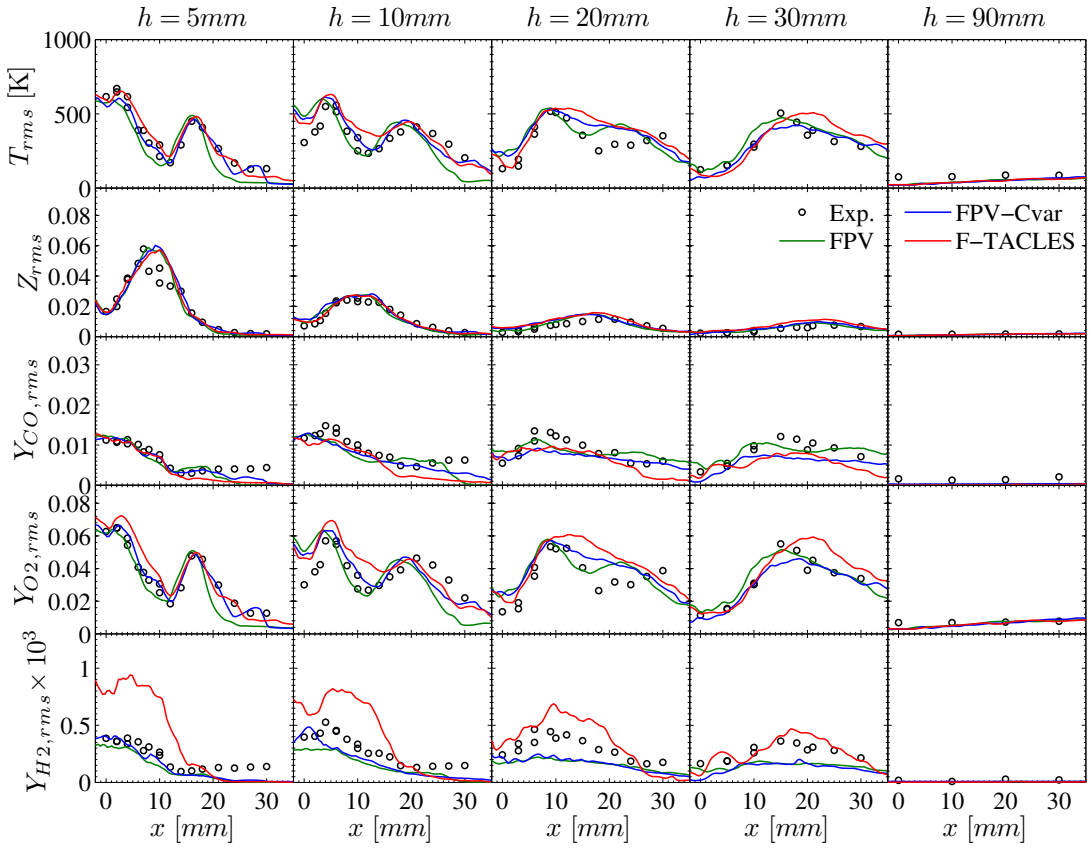

Figure 4.18: Comparison of resolved rms of thermo-chemical variables for flame A simulations with experimental data at several axial locations on the cut-plane of $z = 0$.

4.5.3 Conditional Statistics

The spatial mean and rms profile of the thermo-chemical variable can be highly susceptible to flow field effects. Although the velocity profiles of LES are in good agreement with those measured in experiment, the longer IRZ seems to affect the distribution of mixture fraction. To isolate the effect of combustion models, statistics conditioned to the mixture fraction are computed for the simulation and experimental results. Moreover, the conditional data is evaluated separately at three different ranges of x to delineate the IRZ, injector stream and ORZ.

The conditional mean of temperature and the mass fraction of CO, $\mathrm{H_2O}$, and $\mathrm{O_2}$ at $h = 5$ mm and $h = 10$ mm are shown in Fig. 4.19 and Fig. 4.20, respectively. For axial locations greater than $h = 10$ mm, the conditional data converge to the mean results due to the lack of variation in mixture fraction. At both axial locations where the conditional statistics can be meaningful, the characteristics of the results are very similar, so no distinction is made between the two locations in the following comparison.

In Fig. 4.19 and Fig. 4.20, the conditional mean profiles in the leftmost column correspond to that of the IRZ whereas those in the middle column correspond to the injector stream. The rightmost column shows profiles that are generated from data within the ORZ. With this in mind, the comparison with experimental data reveals that the peaks of the predicted conditional temperature are shifted towards a richer mixture in the IRZ. This shift may be attributed to the distribution bias of the mixture fraction to the richer mixture in the simulations. In the injector stream, the conditional results of FPV-Cvar show the best agreement with the experimental measurements. In contrast, the F-TACLES model predicts a slightly higher conditional temperatures, while the FPV model predicts slightly lower conditional temperatures.

In the ORZ, the conditional mean temperature profiles of the simulations appear to be shifted to the leaner mixture when compared to the experimental measurements. In addition, the peak temperature measured in the experiment is also lower than the simulations

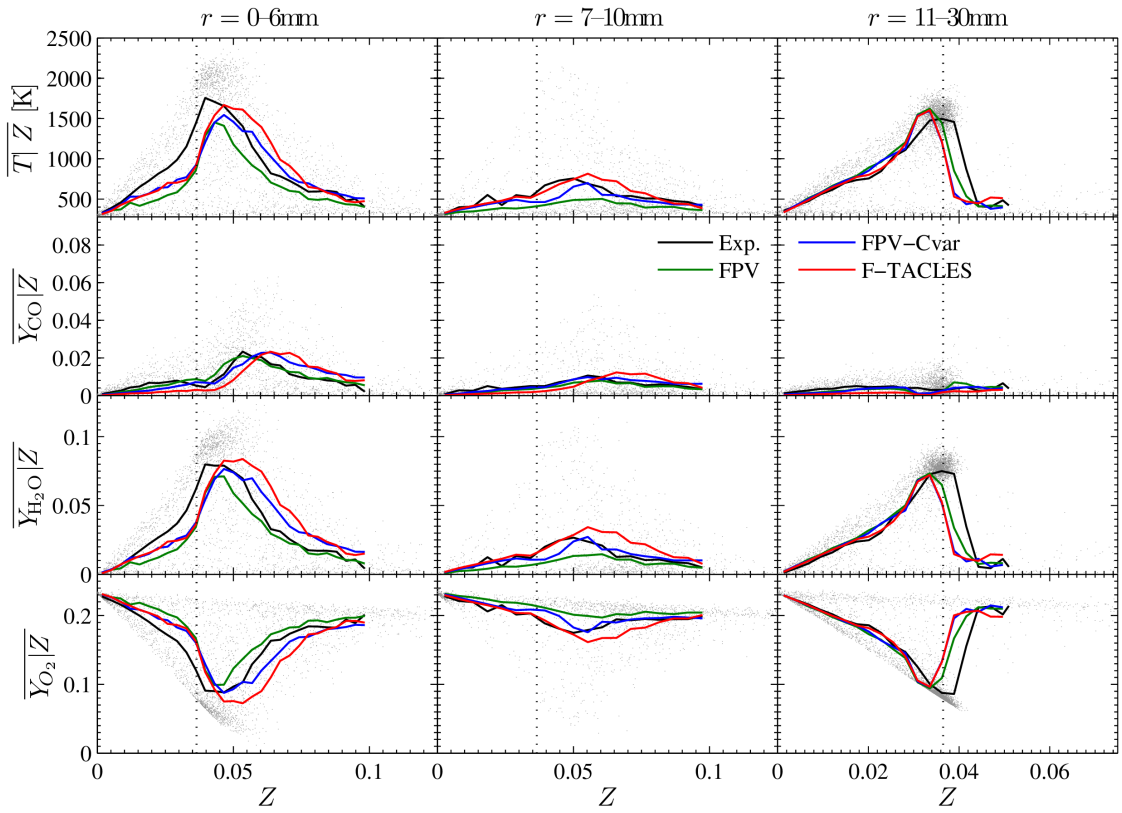

Figure 4.19: Comparison of measured (black lines) and calculated conditional mean of temperature and the mass fraction of selected species at $h = 5$ mm and $|x| = 0$–6 mm, 7–10 mm and 11–30 mm for flame A. Scatter plots of the experiment data are shown in the background.

predictions. The wall heat loss in the ORZ is likely to be the cause of the lower peak temperature measured in experiment. Moreover, the mixtures near the walls tend to be leaner so the heat loss mostly occurs in the lower mixture fraction. This may shift the peak temperature to a higher mixture fraction value. Therefore, a non-adiabatic extension of the flamelet models needs to be able to account for these effects in order to yield better predictions than the adiabatic models considered in this study.

4.5.4 CH and OH Fields

The combustion models show better agreement with the experiment measurements in the *a priori* analysis than in the comparison between the *a posteriori* LES results and the exper-

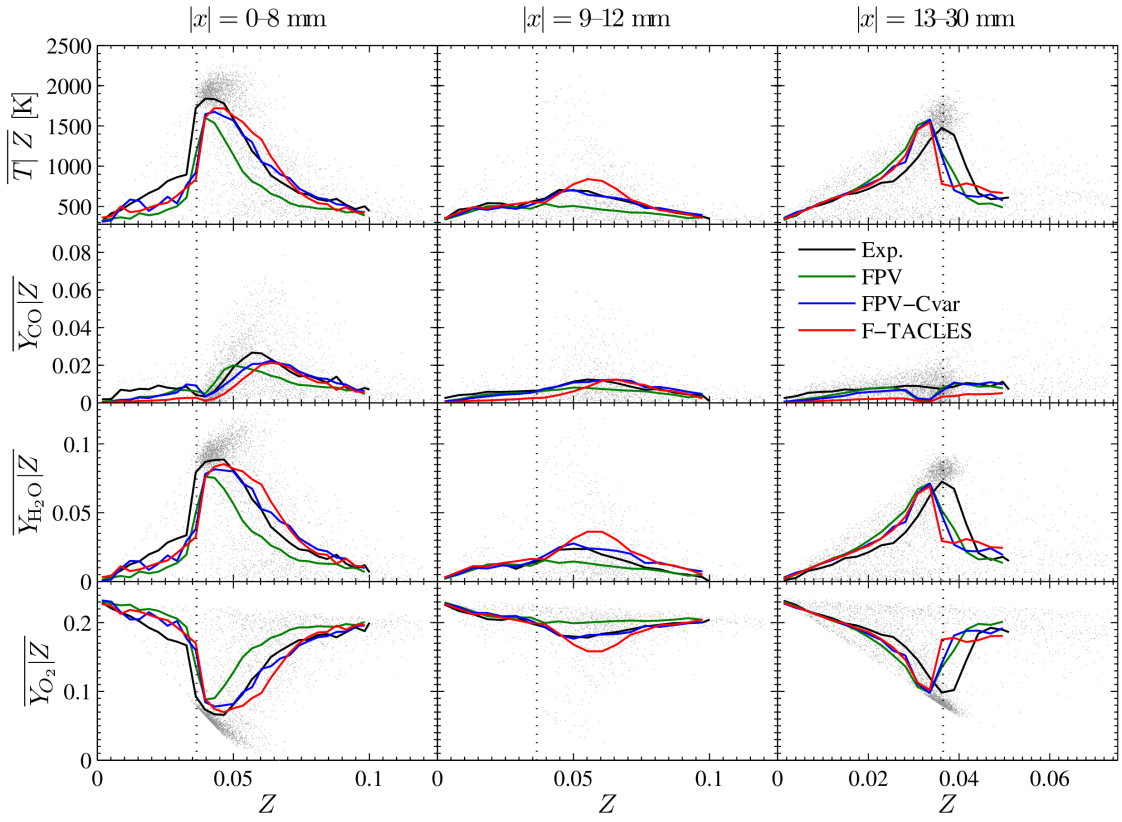

Figure 4.20: Comparison of measured (black lines) and calculated conditional mean of temperature and the mass fraction of selected species at $h = 10$ mm and $|x| =$ 0–8 mm, 9–12 mm and 13–30 mm for flame A. Scatter plots of the experiment data are shown in the background.

imental results. This is expected as the *a priori* analysis does not consider the accuracy of the modeled chemical source terms, The chemical source terms are crucial in determining the characteristics of the reaction zone, which is beyond the scope of the a *priori* analysis. Moreover, none of the chemical species concentrations obtained from Raman spectroscopy can be indicative of the reaction zone. Therefore, PLIF measurements of the CH and OH fields (Weigand *et al.*, 2006) are used in this study to examine the predicted reaction zone in LES. These two chemical species are radicals in combustion and are produced in the reaction zone. The CH radical has a shorter life time so it is generally restricted to the reaction zone while the OH species decays more slowly and its life-time may extend to the post reaction state.

As PLIF measurements generally do not yield quantitative data, the comparison of the CH and OH fields is more qualitative. The averaged PLIF measurement of CH, shown in Fig. 4.21d, is V-shaped and its highest peak is offset from centerline. Fig. 4.21c shows the mean CH field of the LES utilizing the F-TACLES model. In generally, the shape and the peak of the mean CH field are well reproduced by this simulation. The mean CH results of the non-premixed models, shown in Fig. 4.21a and Fig. 4.21b, are also V-shaped but their CH peaks are located at the centerline. This slight difference in the predictions by the combustion models is further discussed in the following section.

The PLIF measurements of OH are shown in Fig. 4.21d. The region of high OH concentration, as with CH, is V-shaped too. The PLIF measurements also indicate lower OH concentration in the injector's stream. This characteristic of the OH field can also be seen in the results of the LES calculations with the non-premixed models. However, the simulation utilizing the F-TACLES model predicts a region of low OH concentration that is shorter than that was measured in experiment.

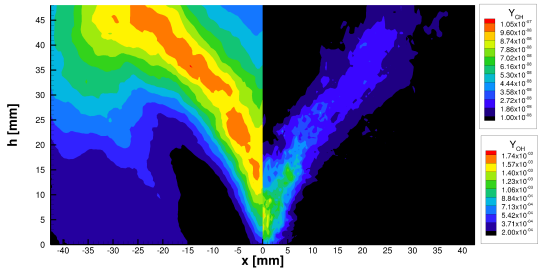

(a) Mean field of Y_{OH} and Y_{CH} for FPV simulation.

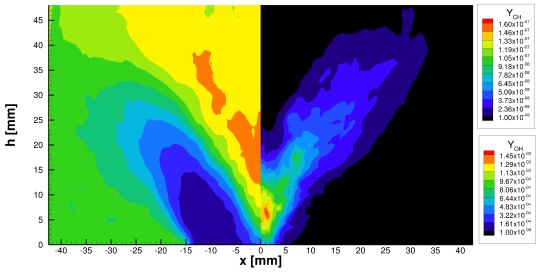

(b) Mean field of Y_{OH} and Y_{CH} for FPV-Cvar simulation.

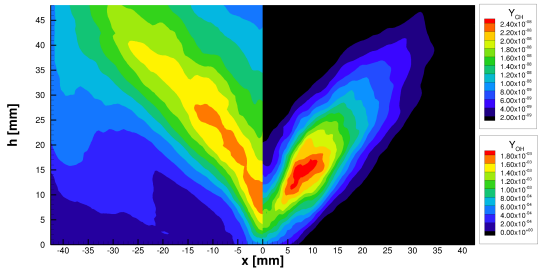

(c) Mean field of Y_{OH} and Y_{CH} for F-TACLES simulation.

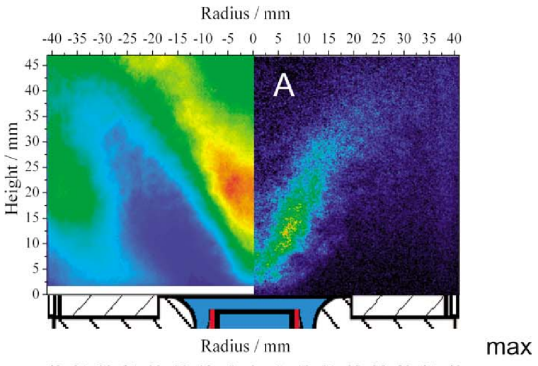

(d) Mean field of Y_{OH} and Y_{CH} PLIF signal.

Figure 4.21: Mean field of Y_{OH} (left) and Y_{CH} (right) for simulations with different combustion models and PLIF measurements.

4.5.5 Flame Index

To characterize partially premixed combustion, Yamashita *et al.* (1996) suggested a flame index to determine if the local combustion process resembles premixed flam or non-premixed flame. The Takeno flame index is based on the alignment of the gradient of fuel mass fraction with the gradient of oxidizer mass fraction. In this study, the Takeno flame index is evaluated as

$$F.I. = \frac{\nabla\overline{Y_{\mathrm{CH_4}}} \cdot \nabla\overline{Y_{\mathrm{O_2}}}}{\left|\nabla\overline{Y_{\mathrm{CH_4}}}\right| \left|\nabla\overline{Y_{\mathrm{O_2}}}\right|}. \tag{4.58}$$

The flame index is set to zero when the gradient evaluation of the species mass fractions in the denominator yields zero. In principle, a flame index value of 1 indicates a premixed flame while a flame index value of -1 suggests a non-premixed flame.

The Takeno flame index is calculated for the LES calculations utilizing FPV, FPV-Cvar, and F-TACLES models and the results are shown in Fig. 4.22. Independent of the combustion model, the flame index generally shows that non-premixed combustion is likely within the injector stream while the conditions in the ORZ and IRZ are more favorable to premixed combustion. These findings may explain the discrepancies in the prediction of the CH field by the non-premixed models as the CH reaction zone mostly lies within the IRZ, where premixed combustion is expected. On the other hand, the shorter low-OH concentration region in the results of the F-TACLES model may be attributed to the inability of this model to accurately reproduce the non-premixed flame in the injector stream.

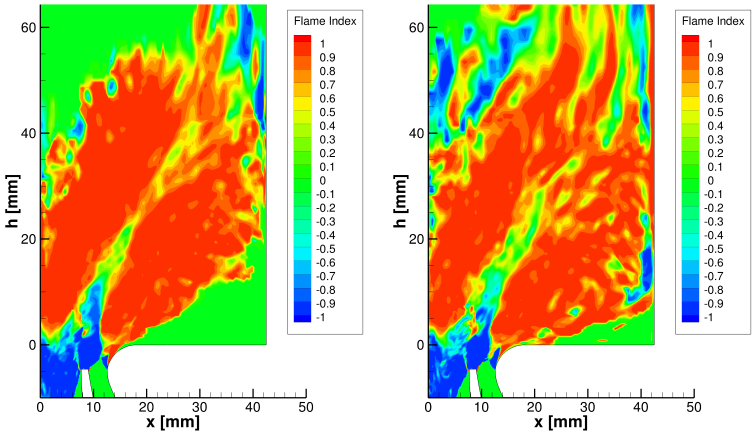

(a) Flame Index of FPV simulation.

(b) Flame Index of FPV-Cvar simulation.

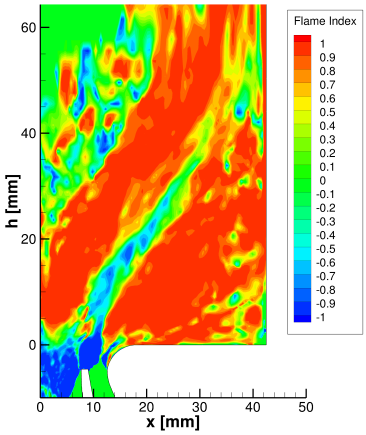

(c) Flame Index of F-TACLES simulation.

Figure 4.22: Flame Index evaluated on the mean results of (a) FPV ,(b) FPV-Cvar , and (c) F-TACLES simulations.

CHAPTER 5

Conclusions

In this work, we have examined and extended two different classes of predictive methods in the context of reacting flow. One of the methods is the linear stability analysis which is considered to be a lower-order method. This analysis tool has been used in the past for theoretical studies of flow dynamics. Recently, this method is seeing broader application in more complex flow configurations. To extend linear stability analysis for utilization in more complex reacting flows, we have introduced the flamelet model to this analysis method.

The flamelet model, a combustion model based on the solutions of one-dimensional flames, is commonly used in large eddy simulations (LES) of jet flames. Flamelet models are usually developed to capture either premixed or non-premixed combustion but not both combustion modes at the same time. Despite that, several applications of the flamelet models in partially-premixed flames have produced results that are agreeable with experimental measurements. However, using flamelet models in LES is relatively untested in more realistic combustor configurations.

If the flamelet models are shown to be reasonable assumptions in the simulations of realistic combustors, then our flamelet extension of the linear stability analysis may be also applicable to such complex configurations as well. Recognizing that these two approaches are intertwined, this work seeks to address both issues at the same time. Specifically, our extension of linear stability analysis with a flamelet model is validated in a simple buoyant jet flame configuration. The utilization of flamelet models in LES is also examined in a gas

turbine model combustor which exhibits the same complex features of a real combustor. Our findings and conclusions in these reacting flow setups are summarized below.

5.1 Buoyant Diffusion Jet Flame

The buoyant jet diffusion flame investigated by Füri *et al.* (2002) is used as the configuration to apply the linear stability analysis method with a flamelet model. Specifically, this analysis focuses on the inner Kelvin-Helmholtz instability mode of this jet flame. The growth rate of the inner mode at a single axial position is estimated from harmonically forced simulations of the jet flame. Comparison with local linear stability analysis results shows good agreement with simulations results. More specifically, the computed growth rate of the instability as a function of excitation frequency at $x/D = 0.13$ is similar for both the linear stability analysis results and processed data from simulations.

In addition, we have also considered a global mode reconstruction of the inner mode using local linear stability analysis solutions. Overall, the reconstructed global modes are qualitatively similar to the excited modes in simulations. Among the two frequencies of excitation examined here, better agreement is seen at the lower frequency. At the higher forcing frequency, non-linear effects may be become more important than in the low frequency case.

The sensitivity of the inner mode instability to modeling assumptions is also investigated with linear stability analysis. The utilization of a flamelet model allows for seamless switching of chemistry kinetics, transport models and gas laws. Our findings indicate that a simpler description of the reaction chemistry tends to lead to a lower prediction of the growth rate the inner mode instability. It is important to note that simpler chemistry kinetics is still used in reacting flow as the stiffness of complex chemistry can introduce significant computational cost.

Besides the inner mode, the outer instability mode of this buoyant jet flame is also

investigated with linear stability analysis. By using Briggs' method, the outer mode is shown to be absolutely unstable. Furthermore, the analysis indicates that this instability mode becomes convective when buoyancy effects are reduced. Compared to the early work by Lingens *et al.* (1996), in which buoyancy effects are neglected in their analysis, our model show that this absolute instability is driven by buoyancy.

In addition to the linear stability analysis, this buoyant jet flame is also investigated by applying spectral analysis and proper orthogonal decomposition to the results of the simulations. Examination of the temporal evolution of the temperature reveals that temperature oscillations due to the instability can become saturated. This effect is not accounted for in linear stability analysis and may be a source of error. A POD analysis also yields spatial empirical modes for the outer instability that evolve at higher harmonic frequencies.

5.2 LES of Gas Turbine Model Combustor

Isothermal and reacting LES were performed for a gas turbine model combustor (GTMC) (Weigand *et al.*, 2006; Meier *et al.*, 2006). The operating condition of flame A is considered for the application of LES as it is most representative for the condition of an aircraft engine. The combustion process in this flame is categorized as partially premixed. Hence premixed or non-premixed flamelet models may not be able to fully capture the flame dynamics. To this end, the models are examined to assess the error introduced by the projection of the experimentally measured flame states onto the flamelet solutions. Overall, the flamelet models are reasonably accurate in reproducing the temperature and the mass fractions for major species in the flame.

The reacting simulations are calculated with three different flamelet models: two non-premixed models and one premixed model. Based on the results of these computations, the velocity field is generally insensitive to the combustion model. Moreover, comparisons with LDV velocity measurements suggest that the simulation is in good agreement with

the experiment. However, the LES predictions of thermo-chemical variables show greater sensitivity to the combustion models. In general, the premixed flamelet model predicts slightly higher temperature in the inner recirculation zone while the non-premixed models predict higher temperature in the outer recirculation zone. In the interior of the GTMC, the predicted mean and rms fluctuation of temperature are in good agreement with the experiment.

Independent of the combustion models utilized, the simulation results generally show higher temperatures than the experimental measurements near the burner walls. This slight over-prediction is attributed to wall heat loss effects that are not captured in the adiabatic flamelet models. Through evaluation of the conditional statistics, the wall heat losses are shown to lower and shift the temperature peak in mixture fraction space. Future development of non-adiabatic flamelet models should account for these effects.

An isothermal flow in GTMC is also considered in this numerical study. These simulations are performed prior to the reacting case to assess the grid sensitivity of LES results in the GTMC. At the finest mesh, grid convergence of results is obtained and the evaluation of a LES quality criterion indicates that most of the large scale turbulence is sufficiently resolved. However, the wall resolution in the swirl region is insufficient and needs to be addressed in future work.

Within the setting of the isothermal flow, the flow field inside the combustion chamber can be sensitive to the mass flow rate split between the two swirlers in the GTMC. To further investigate this issue, we consider isothermal LES calculations of a truncated burner geometry. The truncated burner is constructed in such a way that the mass flow rate through two swirlers can be individually prescribed in the simulations. By varying this parameter in the simulations, the results show that this parameter is able to affect the swirl strength, thus changing the flow field within the combustion chamber.

5.3 Future Work

In the linear analysis of the buoyant jet flame, we find that the parallel flow assumption may be inadequate for analysis of the outer mode. Therefore, the next step is to forgo the local parallel flow assumption and develop a bi-global stability analysis method that does not rely on this assumption. Local analysis is still useful as it is needed to provide the unstable frequency range for global stability analysis. Moreover, the global stability analysis method may be applied to the LES results of the GTMC to assess the predictions of linear analysis.

Although the LES calculations of the GTMC are able to reproduce results that are in reasonable agreement with experimental data, further improvements of the mesh, wall-modeling and combustion modeling are needed to obtain predictions that are closer to the measurements. Specifically, either significant mesh refinement at the walls or the utilization of a wall model is needed to obtain higher quality LES solutions in the swirler portion of the GTMC. In addition, the wall heat loss effects need to be account for in future LES studies of this combustor.

Flames B and C represent two operation mode of the GTMC that are well-characterized in experiments and can be the focus of future LES studies of this burner. Since Flame B experiences significant thermo-acoustics instabilities, future LES investigations of this flame must consider compressibility effects. A natural continuation of this work is to utilize a compressible LES solver to assess the capability of the LES approach in predicting this unstable flame.

Combustion processes in aircraft engines can be a source of aircraft noise. In general, the noise contributions of the combustion can be categorized into direct combustion noise and indirect combustion noise. Direct combustion noise is due to the pressure waves directly generated by the reacting flows in the combustor. Thermo-acoustic instabilities, if present, can be a significant contributor to direct combustion noise. Indirect noise is generated by the interaction of gas turbine components with the entropy perturbations that

are induced by the unsteady combustion processes. As a preliminary work on indirect combustion noise, we have extracted the outgoing entropy perturbations from the GTMC simulation and studied the noise generated when these perturbations are issued into a contracting nozzle. In addition, jet noise can also be generated in the shear layer of the jet stream and is another subject of future work.

APPENDIX A

Core Noise Investigation

A.1 Introduction

Jet exhaust noise is a major contributor to the far-field radiation in low-bypass aircraft engines. Over the last thirty years, significant progress has been made in understanding the noise-generating mechanisms of subsonic and supersonic jets (Tanna *et al.*, 1976; Tam, 1995; Morris *et al.*, 2002). Specifically, the noise from imperfectly expanded jets can be separated in contributions from turbulent mixing noise, broadband shock-associated noise, and screech tones. The relative intensity of these individual noise source components is dependent on operating conditions.

Apart from the direct propagation of core noise to the far field, core noise fluctuations can play a pivotal role in the jet noise amplification (Brown, 2005). Experimental studies have shown that tonal and broadband excitations upstream of the nozzle exit can amplify the jet noise by as much as 5–10 dB compared to the unforced condition (Lu, 1983; Gerend *et al.*, 1975; Bechert & Pfizenmaier, 1976). In particular, Bechert & Pfizenmaier (1976, 1975) reported a pronounced broadband shift of the radiated sound for excitations at the preferred shear-layer frequency. These observations on the jet noise amplification were confirmed by Berman (1981) for axial and coaxial low-bypass jets; they attributed this so-called excess noise to the excitation of the shear layer and subsequent increase in turbulent stresses. Comprehensive experimental investigations by Lu (1983) in coaxial jets at

simulated high bypass ratio engine conditions showed that also broadband excitations can generate significant excess jet noise, which increases with increasing excitation level.

Although detailed understanding and comprehensive data about excess noise in heated and imperfectly expanded jets are largely missing, an experimental study by Jubelin (1980) concluded that heated jets are more receptive to upstream excitations, and the generated excess noise has a pronounced directivity in the forward direction. Furthermore, measurements in supercritical jets showed that shock-associated noise can be strongly amplified. Compared to subsonic jets, these far-field spectra did not show evidence of the tonal excitation, which suggests that the absence of irregularities in the spectral shape is insufficient to discriminate between excited and unexcited jet noise (Jubelin, 1980).

Toward investigating the effect of turbulence on the jet-acoustic response, experimental investigations by Raman *et al.* (1989) revealed that the frequency of the preferred mode and excitation amplitude depends on the initial level of turbulence intensity. Comprehensive investigations by Ahuja and coworkers examined the jet noise broadband amplification problem using flow visualization (Ahuja & Whiffen, 1985), flow measurements (Lepicovsky *et al.*, 1985; Ahuja & Whiffen, 1985) and acoustic measurements Ahuja & Blakney (1985). They concluded that amplified large-scale structures result in increased small-scale turbulence and the small-scale turbulence is responsible for the increased broadband noise (Ahuja & Blakney, 1985). Theoretical results by Zaman showed that excitations enhance the vortex pairing, which is responsible for the increased sound generation (Zaman, 1985).

The objective of this work is to investigate effects of nozzle-upstream perturbations on the acoustic radiation in heated jets. To this end, large-eddy simulations of a model gas-turbine combustor are performed to provide realistic combustor exit conditions. The combustor exit is connected to a converging nozzle, discharging the combustion products into the ambient environment. Details regarding the model problem and computational configuration are given in the next section. A linear Euler formulation is used to model the

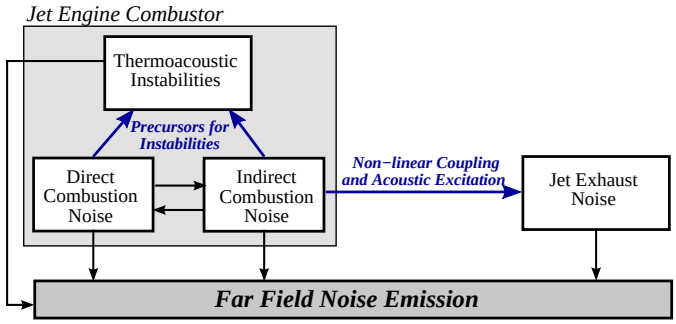

Figure A.1: Direct and indirect noise source contributions originating from unsteady combustion process, non-linear coupling mechanisms, and jet noise amplification; Arrows in blue show the indirect core noise contributions.

indirect noise-generation that results from the coupling between entropy inhomogeneities exiting the combustor and pressure radiation. The computational model for the description of the combustor, the jet mean-flow simulation, and linearized Euler formulation are discussed in Sec. A.3. Modeling results are presented in Sec. A.4, and the paper finishes with conclusions.

A.2 Problem Formulation

In aircraft engines several acoustic interaction processes exists, and the underlying coupling mechanisms are schematically illustrated in Fig. A.1. Specifically, the unsteady flow-field in the combustor generates inhomogeneities in vorticity, pressure, and entropy. Pressure perturbations that are generated in the engine are commonly associated with direct-noise contributions that propagate downstream, exit the nozzle, and radiate to the far-field. Although dependent on engine configuration and operating regime, these direct core noise contributions typically fall in the low-frequency range, corresponding to the 200-400 Hz frequency band (Miles, 2008, 2009). In this context it is also noted that these direct noise-sources can act as a bypass mechanism to excite thermo-acoustic instabilities in the combustor (Poinsot & Veynante, 2005; Knoop *et al.*, 1997; Burnley & Culick, 2000; Lieuwen, 2002), and even relatively weak interactions can trigger combustion instabilities (Putnam, 1971).

Apart from combustion-generated pressure perturbations, the unsteady combustion process generates velocity and entropy fluctuations that exit the combustor, and are convected to the nozzle. As shown by Marble & Candel (1977), these entropy perturbations interact with the pressure gradients in the turbine and the nozzle, and are converted to acoustic pressure perturbations. This process is referred to as indirect noise.

The present work is concerned with investigating effects of entropy perturbations on the acoustic radiation in heated jets. A schematic of the model-problem is illustrated in Fig. A.2, and consists of a gas-turbine combustor which is connected to a converging nozzle, expanding the combustor exhaust products into the ambient environment. Large-eddy simulations of the combustor are performed to evaluate the mean-flow and fluctuating quantities at the combustor exit. The mean-flow in the nozzle and the jet is obtained as solution of a steady-state Reynolds-averaged Navier-Stokes (RANS) simulation, and the spatio-temporal evolution of the perturbations of pressure, velocity, and entropy are evaluated from the linearized Euler equations (LEE). Details on the mathematical model, geometric configurations, and operating conditions are provided in the next section.

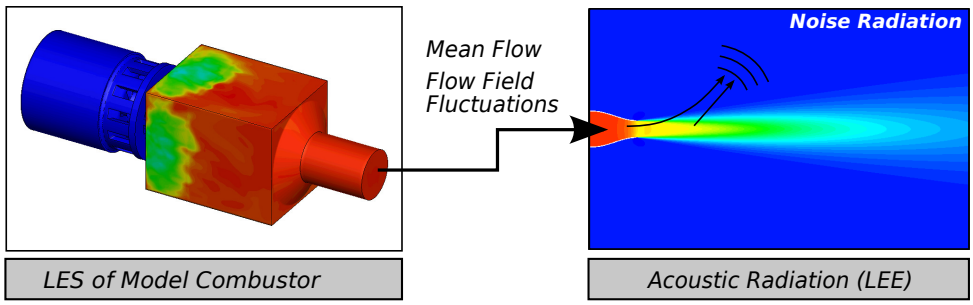

Figure A.2: Schematic of the model-problem, consisting of (i) a large-eddy simulation of a model gas turbine combustor for predicting transient combustor exit conditions, and (ii) simulation of the nozzle flow and acoustic far-field radiation.

A.3 Computational Model

A.3.1 Jet Mean Flow Computation

The exit of the combustor is connected to a converging nozzle, and a separate steady-state RANS computation is performed to compute the flow in the nozzle and the heated jet. This RANS simulation begins at the nozzle inlet, at which flow-field conditions from the combustor simulation are prescribed. The nozzle inlet conditions for the mean-flow simulation are obtained by averaging over the combustor exit area, resulting in a mean temperature of $\langle\widetilde{T}\rangle = 1752$ K and mean pressure of $\langle\overline{p}\rangle = 2$ bar (corresponding to a combustor exit Mach number of 0.123).

The geometry of the nozzle is approximated by a cubic polynomial, having the following form

$$r = 172.8x^3 + 12.96x^2 + 0.0092 \ [\mathrm{m}] \qquad \text{for} \qquad -0.05 \ \mathrm{m} \leq x \leq 0 \ , \tag{A.1}$$

where r and x are the radial and axial coordinates. The nozzle has zero slopes at both ends and a thickness of 1mm with a round trailing edge. The nozzle geometry together with the geometry-conformal mesh around the nozzle are illustrated in Fig. A.3. Based

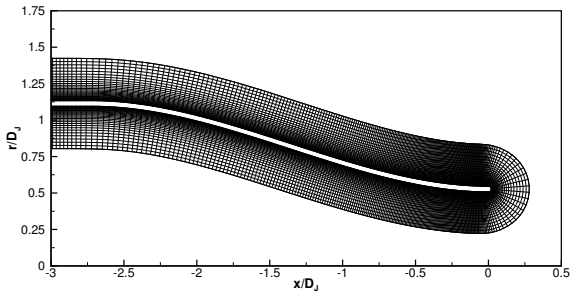

Figure A.3: Nozzle geometry and geometry-conformal mesh around the nozzle geometry.

on the combustor exit conditions and the nozzle geometry, the nozzle exit Mach number is 0.95 and the Reynolds number, $\mathrm{Re} = \mathrm{U_J D_J}/\nu$, is 200,000. The computational domain

for the jet mean-flow simulation extends up to $x = 1$ m and the spatial extend in radial direction is $r = 0.5$ m, corresponding to 54 and 27 nozzle exit diameters, respectively. The entire computational domain was discretized using 300,000 control volumes, and a grid-refinement study was performed to ensure that the solution is grid-independent. A geometry-conformal structured mesh is used within the nozzle and an unstructured grid is used to discretize the nozzle-exterior domain. Local grid refinement is employed in the shear-layer region. A finite volume method is used to solve the compressible Navier-Stokes equations in an axisymmetric domain. The steady RANS equations are solved using a second-order upwind flow solver with standard $k - \varepsilon$ turbulence model. Pressure boundary conditions are enforced at the outlet, and gauge pressure of 1 bar and temperature of 1752 K are prescribes as inlet conditions.

Figure A.4 compares simulation results from the 2D RANS computation with analytical results that are obtained from 1D nozzle theory. Overall, good agreement is obtained, and small differences near the nozzle exit are attributed to the formation of expansion fans as results of the under-expanded nozzle exit condition. Shown in the middle figure is the temperature along the nozzle axis. Temperature is normalized by the ambient condition. Corresponding to the combustor operating conditions and the nozzle geometry, the temperature ratio at the nozzle exit is $T_J/T_0 = 5$.

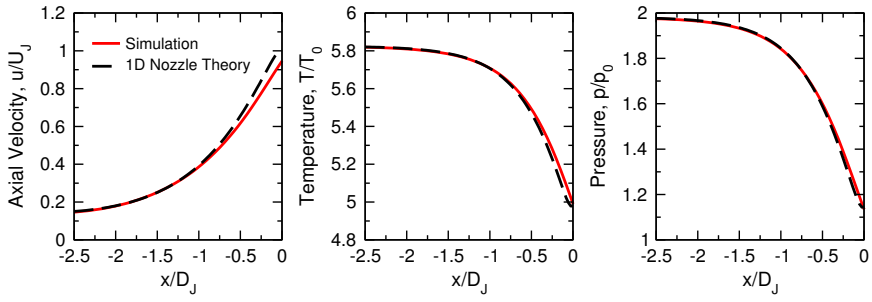

Figure A.4: Comparison of flow-predictions through the nozzle: axial velocity (left), temperature (middle), and pressure (right).

Due to the under-expanded nozzle condition (see right of Fig. A.4), an expansion fan forms at the nozzle lip, resulting in velocity oscillations near the nozzle. This is illus-

trated in Fig. A.5, showing the mean axial velocity along the jet centerline. To facilitate a qualitative comparison of the simulation results, we also present measurements that were reported by Plumblee *et al.* (1976). It is noted that exit condition and heating ratio are not representative for the configuration under investigation, but nevertheless enables a relative comparison.

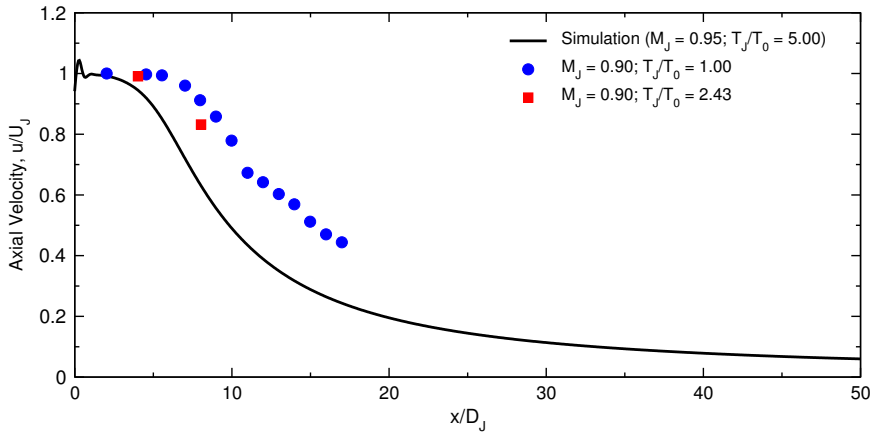

Figure A.5: Axial velocity along jet centerline. Experimental data (Plumblee *et al.*, 1976) for qualitative comparison are shown by symbols.

The mean axial velocity field and mean temperature field are shown in Fig. A.6. Velocity contours through the nozzle indicate the presence of two-dimensional effects, and the presence of a shock-cell near the nozzle exit is observable. The mean temperature field is shown on the right of Fig. A.6. Due to the expansion through the nozzle, the temperature reduces by approximately 250 K. The temperature affects the thermoviscous properties, increasing the viscosity and thereby suppressing the turbulence generation. Theoretical analysis by Monkewitz & Sohn (1988) suggests that heated jets can exhibit regions of absolute instability in the potential core, and this stability boundary is dependent on operating conditions and density ratio. Regions of absolute instability can lead to exponential growth of perturbations that are generated upstream of the nozzle exit. These absolute instability regions can enhance the noise generation, and this issue will be addressed in the next section.

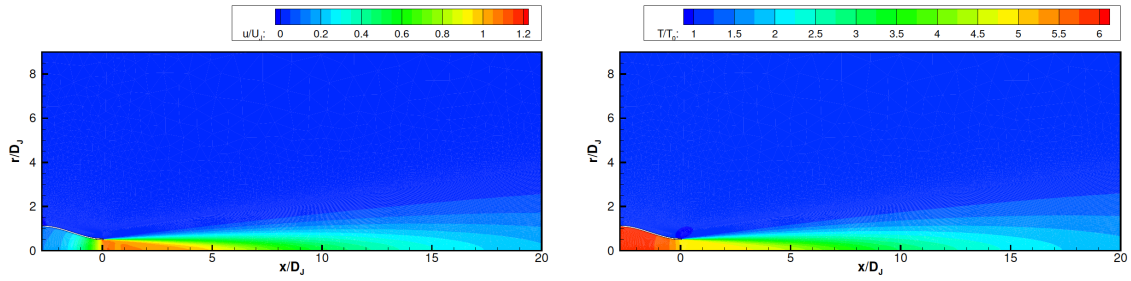

Figure A.6: Predicted jet mean flow field: axial velocity (left) and temperature (right).

A.3.2 Linearized Euler Model

A.3.2.1 Mathematical Model

The evolution of the jet flow is governed by the unsteady Navier-Stokes equations which are here written for pressure p, velocity $\boldsymbol{u}$, and entropy s. These equations can be written in non-dimensional form as:

$$\frac{\partial p}{\partial t} + \boldsymbol{u}\cdot\nabla p + \gamma p \nabla\cdot\boldsymbol{u} = (\gamma-1)\left[\mathcal{C}+\mathcal{D}\right] \ , \tag{A.2a}$$

$$\frac{\partial \boldsymbol{u}}{\partial t} + \boldsymbol{u}\cdot\nabla\boldsymbol{u} = -\frac{1}{\gamma \mathrm{M}^2}\frac{1}{\rho}\nabla p + \frac{1}{\mathrm{Re}}\frac{1}{\rho}\nabla\cdot\underline{\underline{\tau}} \ , \tag{A.2b}$$

$$\frac{\partial s}{\partial t} + \boldsymbol{u}\cdot\nabla s = \frac{1}{p}\left[\mathcal{C}+\mathcal{D}\right] \ , \tag{A.2c}$$

where $\mathcal{C} = \frac{\gamma}{\gamma-1}\frac{1}{\mathrm{Re}\,\mathrm{Pr}}\nabla\cdot(\lambda\nabla T)$ is the heat flux, $\mathcal{D} = \gamma\frac{\mathrm{M}^2}{\mathrm{Re}}\underline{\underline{\tau}} : \nabla\boldsymbol{u}$ is the viscous dissipation, and $\underline{\underline{\tau}}$ is the viscous stress tensor.

To obtain the linearized Euler equations (LEE), the state vector $\boldsymbol{\phi}(\boldsymbol{x},t) = (p,\boldsymbol{u},s)^T$ is decomposed into mean and fluctuating components, $\boldsymbol{\phi}(\boldsymbol{x},t) = \overline{\phi}(\boldsymbol{x}) + \boldsymbol{\phi}'(\boldsymbol{x},t)$, in which an over-bar denotes a mean quantity and the prime refers to a perturbation. After expanding Eqs. (A.2), and neglecting viscous and higher-order terms, the linearized Euler equations

can be written as:

$$\frac{\partial p'}{\partial t} + \boldsymbol{u}' \cdot \nabla \bar{p} + \bar{\boldsymbol{u}} \cdot \nabla p' + \gamma \left(p' \nabla \cdot \bar{\boldsymbol{u}} + \bar{p} \nabla \cdot \boldsymbol{u}' \right) = 0 \ , \tag{A.3a}$$

$$\frac{\partial \boldsymbol{u}'}{\partial t} + \frac{\rho'}{\bar{\rho}} \bar{\boldsymbol{u}} \cdot \nabla \bar{\boldsymbol{u}} + \boldsymbol{u}' \cdot \nabla \bar{\boldsymbol{u}} + \bar{\boldsymbol{u}} \cdot \nabla \boldsymbol{u}' = -\frac{1}{\gamma \mathrm{M}^2} \frac{1}{\bar{\rho}} \nabla p' \ , \tag{A.3b}$$

$$\frac{\partial s'}{\partial t} + \boldsymbol{u}' \cdot \nabla \bar{s} + \bar{\boldsymbol{u}} \cdot \nabla s' = 0 \ . \tag{A.3c}$$

The density fluctuation ρ', appearing in Eq. (A.3), is not an independent state variable, and is related to pressure and entropy through the following expression:

$$\frac{\rho'}{\overline{\rho}} = \frac{1}{\gamma} \frac{p'}{\overline{p}} - \frac{\gamma - 1}{\gamma} s' \ . \tag{A.4}$$

Similarly, the temperature perturbations can be related to pressure and entropy as:

$$\frac{T'}{\overline{T}} = \frac{p'}{\overline{p}} - \frac{\rho'}{\overline{\rho}} \ , \tag{A.5a}$$

$$= \frac{\gamma - 1}{\gamma} \left(\frac{p'}{\overline{p}} + s' \right) \ . \tag{A.5b}$$

A.3.2.2 Numerical Method

The linearized Euler equations are solved numerically in a generalized axisymmetric coordinate system. All spatial derivatives are discretized using a 4th-order dispersion-relation-preserving (DRP) scheme (Tam & Webb, 1993), and a low dissipation dispersion Runge-Kutta (LDDRK) scheme is used for time-advancement (Hu *et al.*, 1996). The DRP scheme, as implemented in the solver, uses a central difference stencil in the interior of the computational domain. However, a one-sided biased stencil is used near the boundaries. The biased stencil allows for the treatment of wall boundary conditions, as proposed by Tam & Dong (1994). In this method, impermeable boundary conditions at solid walls are enforced through the pressure in the ghost-cell region. Symmetry boundary conditions are applied

along the centerline. Boundary conditions at the inlet and the far-field are described using the characteristic boundary conditions. In addition to these non-reflecting boundary conditions, a sponge zone is included to further dampen any spurious reflections. Although this boundary treatment may be less effective than more sophisticated methods such as a perfectly matched layer (PML), it is applicable to more general configurations and was successfully employed by Barone & Lele (2005). Time-dependent perturbations at the inlet were imposed through the sponge layer and the sponge strength was adjusted to minimize phase-lag and retain the correct perturbation amplitude.

Due to the geometric complexity of the nozzle it is difficult to utilize a single curvilinear mesh without introducing grid singularities. To address this issue, an over-set mesh-strategy is utilized, and two overlapping curvilinear grids are used. The region surrounding the nozzle is discretized using a C-grid, and a stretched Cartesian grid is used to discretize the rest of the computational domain. The exchange of flow-field information between both grids is accomplished through a 6th-order accurate interpolation scheme using the OVERTURE-framework (Brown *et al.*, 1999), and a 6th-order implicit filter (Visbal & Gaitonde, 2002) is used to suppress spurious oscillations.

A.3.2.3 LEE Verification

The LEE-solver that was outlined in the previous section is verified using a benchmark configuration that describes the acoustic radiation of a harmonic point source which is immersed in a parallel shear-flow (Agarwal *et al.*, 2004). Parameters and operating conditions are identical to the benchmark case, and results of this verification study are presented in Fig. A.7. Figure A.7a shows the instantaneous pressure field; evident from this figure is the presence of a convective Kelvin-Helmholtz instability that propagates in the jet forward direction, and an acoustic mode that radiates in the sideline direction. A comparison of simulation results and analytical results along the sideline $y = 15$ m at the beginning of the excitation period is shown in Fig. A.7b. Overall, the numerical results are in good

agreement with the analytical results except for the region $x > 70$ m. This discrepancy can be attributed to the formation of a shear-layer instability (see Fig. A.7a), which is not contained in the analytical solution.

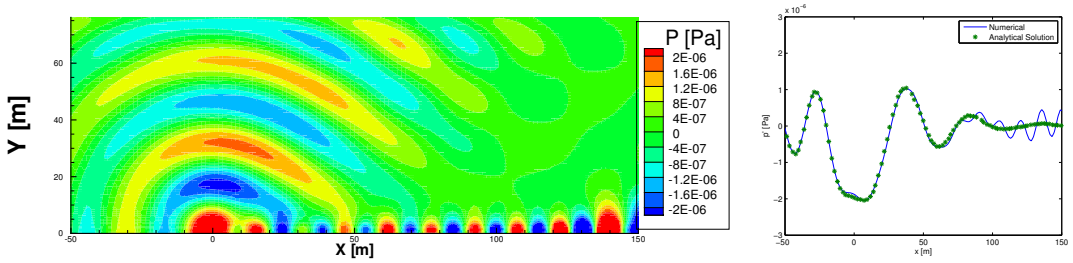

(a) (b)

Figure A.7: Verification of LEE-solver: (a) Pressure field at the beginning of an oscillation period, (b) Quantitative comparison between numerical results and analytical solution (Agarwal *et al.*, 2004).

A.4 Results

A.4.1 Computational Configuration

The computational domain for the LEE simulation is schematically illustrated in Fig. A.8. The axial length of the simulation domain, L_x, is 0.5 m and its radial extend is $L_r = 0.2$ m. The background Cartesian mesh uses 504 grid points in the stream-wise direction and 168 grid points in the radial direction. The C-grid around the nozzle has 480 grid points along the nozzle geometry and 30 grid points normal to the nozzle-wall. The shaded region in Fig. A.8 indicates the sponge-layer, which is extruded into the domain. The dimension of the sponge zone and the corresponding sponge strength parameter σ are summarized in Tab. A.1. Following a quadratic decay-law, the forcing strength in the sponge zone decrease from the prescribed value of σ at the outer end of the sponge layer to zero at the interface with the interior domain.

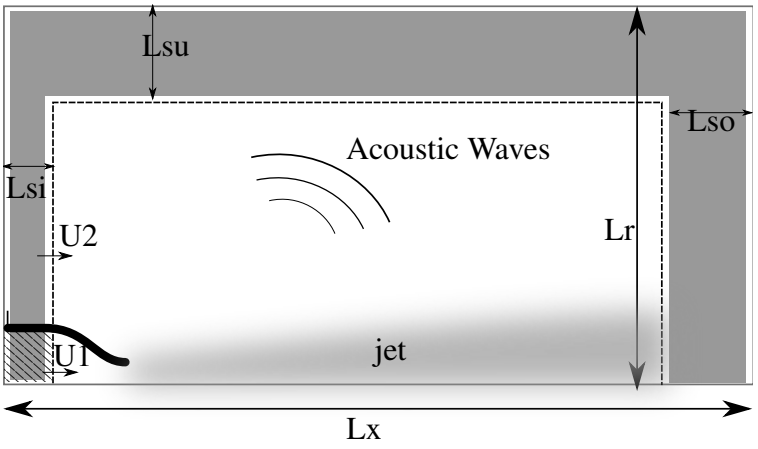

Figure A.8: Schematic of the computational domain.

L_{si}	L_{so}	L_{su}	σ_{si}	σ_{so}	σ_{su}
0.015m	0.05m	0.1m	10^5	10	10

Table A.1: Sponge zone parameters.

A.4.2 Specification of Boundary and Mean-flow Conditions

Transient inflow conditions at the nozzle inlet are obtained from the solution of the combustion-simulation, which was discussed in Chap. 4. Since this simulation employs a low-Mach number formulation, information about pressure perturbations are not available, and only entropy inhomogeneities are prescribed as nozzle-upstream flow-field perturbations in the LEE-model. To this end, the time history of the density field at the combustor exit was recorded, and a proper orthogonal decomposition was used to extract the first energetic radial mode. From this model the corresponding entropy perturbation profile is evaluated using the linearized thermodynamic relation of Eq. (A.4). Harmonic oscillations of this entropy mode of the form

$$s'(r,t) = \widehat{s}(r)\cos(\mathrm{St}\,2\pi\mathrm{t}) \tag{A.6}$$

are then enforced at the inlet. In this equation, St is the Strouhal number, t is the non-dimensional time, and the first energetic entropy POD-mode $\widehat{s}(r)$ is shown in Fig. A.9. This time-dependent boundary condition is prescribed at the nozzle inflow. In the follow-

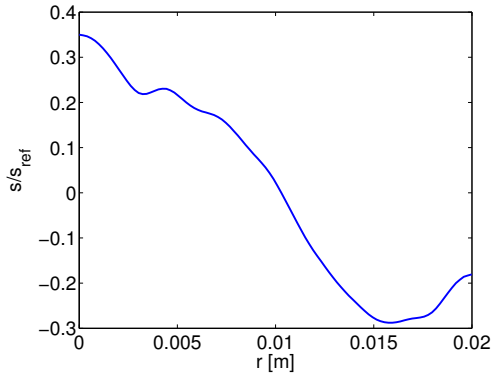

Figure A.9: Entropy mode $\widehat{s}(r)$ obtained from POD-analysis.

ing, three different forcing frequencies, corresponding to $\mathrm{St} = \{0.255, 0.051, 0.0255\}$, are considered, and simulation results are presented in the next section.

A.4.3 Results and Discussion

In this section, modeling results from the LEE-formulation are presented. The reader is reminded that this investigation focuses on the flow-field response to nozzle-upstream perturbations, and non-linear noise-source mechanisms, arising from the turbulence/acoustic/mean-flow interaction are not considered. A numerical investigation of the impulse response showed that the jet-flow is convectively unstable, and an absolutely unstable behavior was not observed for this particular operating condition.

Instantaneous flow-field results for pressure and entropy at three different Strouhal numbers are presented in Fig. A.10. Entropy perturbations at the nozzle inlet interact with the pressure gradient through the nozzle. This coupling process leads to the generation of pressure and velocity instabilities that propagate as acoustic and convective waves, respectively. The spatial evolution of the pressure and entropy waves in the jet-near field shows that the directivity and growth-rate of the instability waves are dependent on the excitation frequency. The configuration with the highest excitation frequency of $\mathrm{St} = 0.255$, shown in the first row of Fig. A.10, exhibits a pronounced directivity of the pressure radiation in the 45° forward direction. Unlike the pressure, the entropy-field, shown in Fig. A.10b, only

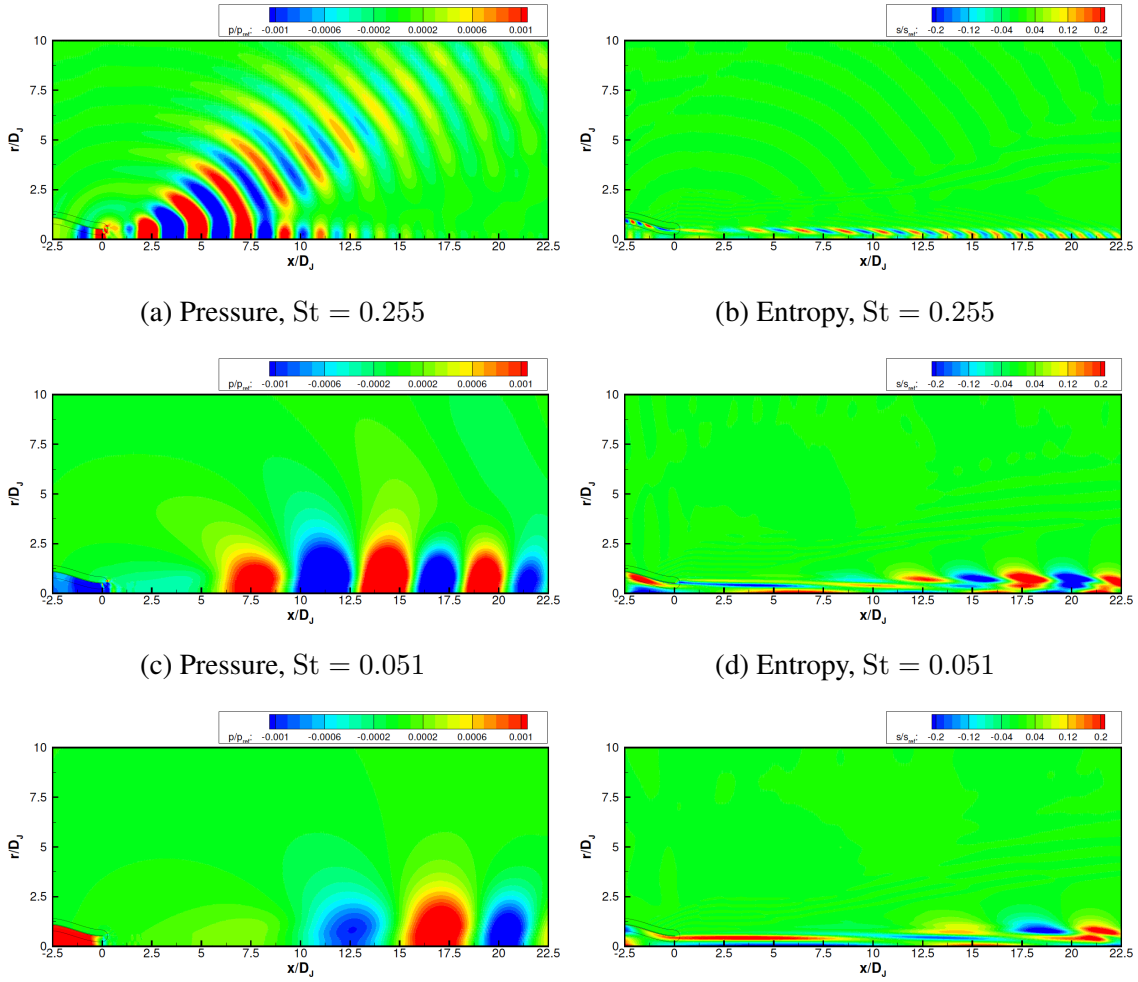

(a) Pressure, $\mathrm{St} = 0.255$

(b) Entropy, $\mathrm{St} = 0.255$

(c) Pressure, $\mathrm{St} = 0.051$

(d) Entropy, $\mathrm{St} = 0.051$

(e) Pressure, $\mathrm{St} = 0.0255$

(f) Entropy, $\mathrm{St} = 0.0255$

Figure A.10: Instantaneous flow-field results for pressure (left) and entropy (right) for three different Strouhal numbers: $\mathrm{St} = 0.255$ (top), $\mathrm{St} = 0.051$ (middle), and $\mathrm{St} = 0.0255$ (bottom).

exhibits a weak growth, and the perturbations decay beyond $x/D_J = 15$. The excitation frequency of $\mathrm{St} = 0.255$ is close to the preferred shear-layer instability. A reduction of the excitation frequency by a factor of 5 and 10, respectively, leads to a shift in the directivity towards the jet forward direction and enhanced amplification of the hydrodynamic instabilities in jet-downstream direction. Figures A.10d and A.10f show that the entropy waves are stretched along the axial direction and are amplified for $x/D_J > 10$.

A comparison of the pressure directivity in the jet near-field confirms the frequency-

dependent jet noise-radiation. This comparison is illustrated in Fig. A.11, showing the root-mean-square pressure signal at a radial distance of $r/D_J = 8.5$ along the axial direction. This comparison confirms the frequency-dependent shift in the directivity, and the pressure radiation shifts towards the jet-forward direct with lower frequency. This requires further consideration and is addressed in subsequent work.

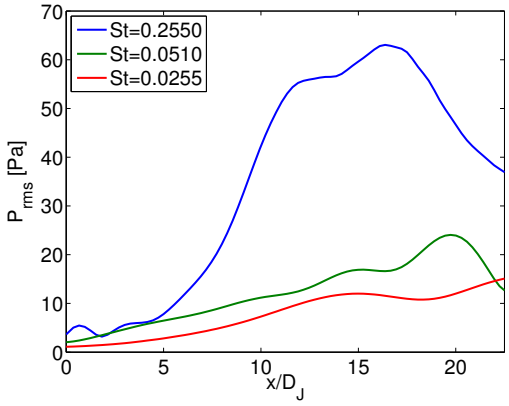

Figure A.11: Near-field directivity at a distance $r/D_J = 8.5$ along the axial direction.

A comparison of the pressure signal and power spectral density at a measurement location of $x/D_J = 15$ and $r/D_J = 8$ is presented in Fig. A.12. It can be seen that after a

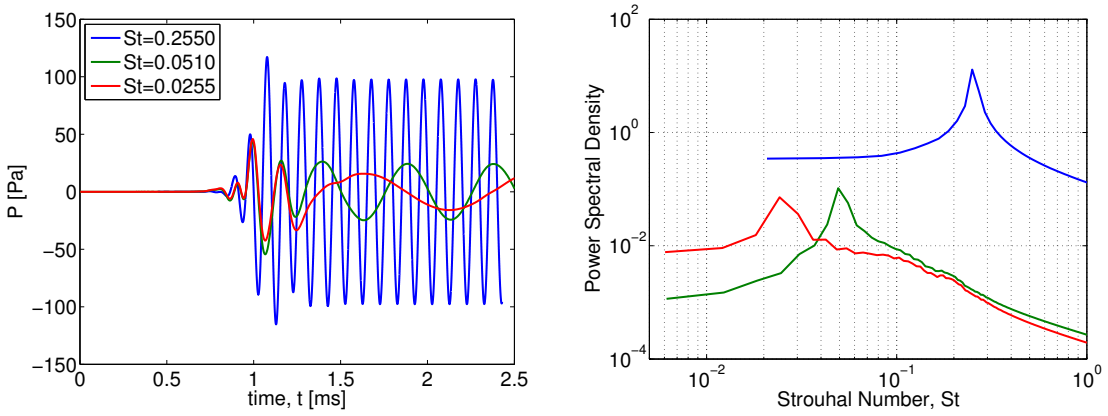

(a) (b)

Figure A.12: Comparison of pressure signal (a) and power spectral density (b) at measurement location $x/D_J = 15$ and $r/D_J = 8$.

short transition period, the pressure signal oscillates at the excitation frequency, which is

a direct result of the linear model-formulation. It is also noted that the magnitude of the pressure signal is different for all three cases. We attribute this to the specification of the inflow perturbation, Eq. (A.6), whose rms-value is frequency-dependent.

A.5 Summary and Conclusions

Effects of nozzle-upstream entropy perturbations on the acoustic radiation from a heated jet are investigated. For this, a model problem is considered, in which a gas-turbine combustor discharges reaction products through a converging nozzle into the ambient environment. The turbulent reacting flow field in the combustor is computed using large-eddy simulation (LES), and the unsteady flow-field at the combustor exit is extracted to provide realistic inflow conditions to the jet-flow simulation. A steady-state RANS simulation is employed to compute the nozzle and the jet mean-flow. A linearized Euler formulation is used to simulate the spatio-temporal evolution of flow-field fluctuations for velocity, pressure, and entropy, and the coupling to the mean flow. The linearized Euler equations are solved in a generalized curvilinear coordinate system using a 4th-order accurate spatial discretization scheme.

Parametric studies are performed to investigate effects of frequency and amplitude of the nozzle-upstream entropy perturbations on the jet instability and the jet noise directivity. Simulation results show that the directivity is dependent on the perturbation frequency. Excitation around the preferred shear-layer instability leads to strong acoustic radiation in the 45° forward direction, and the radiation angle decreases with decreasing excitation frequency.

Further research will focus on extending this analysis to different POD-excitation modes to investigate the sensitivity of the spatial structure on the jet instability. Another research direction addresses the consideration of the non-linear interaction between mean-flow, turbulence, and acoustic perturbations.

BIBLIOGRAPHY

AGARWAL, A., MANI, R. & MORRIS, P. 2004 Calculation of sound propagation in nonuniform flows: Suppression of instability waves. *AIAA Journal* **42** (1), 80–88.

AHUJA, K. K. & BLAKNEY, D. F. 1985 Tone excited jets, Part IV: Acoustic measurements. *Journal of Sound Vibration* **102** (1), 93–117.

AHUJA, K. K. & WHIFFEN, M. C. 1985 Tone excited jets, Part II: Flow visualization. *Journal of Sound Vibration* **102**, 63–69.

ALLISON, P. 2013 Experimental characerization of combustion instablities and flow-flame dynamics in a partially-premixedgas turbine model combustor. PhD thesis, The University of Michigan.

APTE, S. V., MAHESH, K., MOIN, P. & OEFELEIN, J. C. 2003 Large-eddy simulation of swirling particle-laden flows in a coaxial-jet combustor. *International Journal of Multiphase Flow* **29** (8), 1311–1331.

ARNOLDI, W. E. 1951 The principle of minimized iterations in the solution of the matrix eigenvalue problem. *Quart. Appl. Math* **9** (1), 17–29.

AUZILLON, P., GICQUEL, O., DARABIHA, N., VEYNANTE, D. & FIORINA, B. 2012 A filtered tabulated chemistry model for LES of stratified flames. *Combustion and Flame* **159** (8), 2704–2717.

BARLOW, R. S. 1996 Web site for the International Workshop on Measurement and Computation of Turbulent Nonpremixed Flames (TNF), http://www.ca.sandia.gov/TNF/.

BARLOW, R. S. & FRANK, J. H. 1998 Effects of turbulence on species mass fractions in methane/air jet flames. *Proc. Combust. Inst.* **27**, 1087–1095.

BARONE, M. F. & LELE, S. K. 2005 Receptivity of the compressible mixing layer. *Journal Fluid Mechanics* **540**, 301–335.

BECHERT, D. & PFIZENMAIER, E. 1975 Amplification of broad-band jet noise by a pure-tone excitation. *Journal of Sound Vibration* **43** (3), 581–587.

BECHERT, D. & PFIZENMAIER, E. 1976 On the amplification of broadband jet noise by a pure tone excitation. *AIAA Paper 1976-489* .

BECKER, H. A. & YAMAZAKI, S. 1978 Entrainment, momentum flux and temperature in vertical free turbulent diffusion flames. *Combustion and Flame* **33** (2), 123–149.

BEÉR, J. M. & CHIGIER, N. A. 1972 *Combustion Aerodynamics*. Krieger Publishing Company.

BERGMANN, M., BRUNEAU, C.-H. & IOLLO, A. 2009 Enablers for robust POD models. *Journal of Computational Physics* **228** (2), 516–538.

BERKOOZ, G., HOLMES, P. & LUMLEY, J. L. 1993 The proper orthogonal decomposition in the analysis of turbulent flows. *Annual review of fluid mechanics* **25** (1), 539–575.

BERMAN, C. H. 1981 Turbulence and noise characteristics of acoustically excited bypass jet flows. *AIAA Paper 81-2009* .

BILGER, R. 1976 The structure of diffusion flames. *Combustion Science and Technology* **13** (1-6), 155–170.

BILGER, R. 1993 Conditional moment closure for turbulent reacting flow. *Physics of Fluids A: Fluid Dynamics* **5**, 436.

BILLANT, P., CHOMAZ, J.-M. & HUERRE, P. 1998 Experimental study of vortex breakdown in swirling jets. *Journal of Fluid Mechanics* **376**, 183219.

BOEING 2013 Current market outlook 2013-2032. *Tech. Rep.*. Boeing, Seattle.

BONGERS, H., VAN OIJEN, J. A., SOMERS, L. M. T. & DE GOEY, L. P. H. 2005 The flamelet generated manifold method applied to steady planar partially premixed counterflow flames. *Combustion Science and Technology* **177** (12), 2373–2393.

BOUDIER, G., GICQUEL, L., POINSOT, T., BISSIRES, D. & BRAT, C. 2007 Comparison of LES, RANS and experiments in an aeronautical gas turbine combustion chamber. *Proceedings of the Combustion Institute* **31** (2), 3075–3082.

BOWMAN, C. T., HANSON, R. K., DAVIDSON, D. F., GARDINER, W. C., LISSIANSKI, V., SMITH, G. P., GOLDEN, D. M., FRENKLACH, M. & GOLDENBERG, M. 1997 GRI-Mech 2.11. Available from http://www.me.berkeley.edu/gri-mech/.

BOXX, I., CARTER, C. D., STHR, M. & MEIER, W. 2013 Study of the mechanisms for flame stabilization in gas turbine model combustors using kHz laser diagnostics. *Experiments in Fluids* **54** (5), 1–17.

BRIGGS, R. J. 1964 *Electron-Stream Interaction with Plasmas*. MIT Press.

BROWN, C. A. 2005 Acoustics of excited jets – A historical perspective. NASA/TM-2005-213889. NASA.

BROWN, D. L., HENSHAW, W. D. & QUINLAN, D. J. 1999 Overture: Object-oriented tools for overset grid applications. *AIAA-99-3130* .

BUCKMASTER, J. & PETERS, N. 1988 The infinite candle and its stability–A paradigm for flickering diffusion flames. *Symposium (International) on Combustion* **21** (1), 1829–1836.

BURKE, S. P. & SCHUMANN, T. E. W. 1928 Diffusion flames. *Industrial & Engineering Chemistry* **20** (10), 998–1004.

BURNLEY, V. S. & CULICK, F. E. C. 2000 Influence of random excitations on acoustic instabilities in combustion chambers. *AIAA Journal* **38** (8), 1403–1410.

CANDEL, S., DUROX, D., SCHULLER, T., BOURGOUIN, J.-F. & MOECK, J. P. 2014 Dynamics of swirling flames. *Annual Review of Fluid Mechanics* **46** (1), null.

CHARLETTE, F., MENEVEAU, C. & VEYNANTE, D. 2002 A power-law flame wrinkling model for LES of premixed turbulent combustion part i: non-dynamic formulation and initial tests. *Combustion and Flame* **131** (12), 159–180.

CHEN, L., SEABA, J., ROQUEMORE, W. & GOSS, L. 1989 Buoyant diffusion flames. *Symposium (International) on Combustion* **22** (1), 677–684.

CHIGIER, N. A. & BEÉR, J. M. 1964 Velocity and static-pressure distributions in swirling air jets issuing from annular and divergent nozzles. *Journal of Fluids Engineering* **86** (4), 788–796.

CHONG, L. T. W., KAESS, R., KOMAREK, T., FLLER, S. & POLIFKE, W. 2010 Identification of flame transfer functions using LES of turbulent reacting flows. In *High Performance Computing in Science and Engineering, Garching/Munich 2009* (ed. S. Wagner, M. Steinmetz, A. Bode & M. M. Mller), pp. 255–266. Springer Berlin Heidelberg.

CLAVIN, P. & WILLIAMS, F. A. 1979 Theory of premixed-flame propagation in large-scale turbulence. *Journal of Fluid Mechanics* **90** (03), 589–604.

COATS, C. 1996 Coherent structures in combustion. *Progress in Energy and Combustion Science* **22** (5), 427–509.

COLIN, O., DUCROS, F., VEYNANTE, D. & POINSOT, T. 2000 A thickened flame model for large eddy simulations of turbulent premixed combustion. *Physics of Fluids* **12** (7), 1843–1863.

COOK, A. W. & RILEY, J. J. 1994 A subgrid model for equilibrium chemistry in turbulent flows. *Physics of Fluids* **6** (8), 2868–2870.

CORREA, S. M. 1993 A review of NOx formation under gas-turbine combustion conditions. *Combustion Science and Technology* **87** (1-6), 329–362.

CRIGHTON, D. G. & GASTER, M. 1976 Stability of slowly diverging jet flow. *Journal of Fluid Mechanics* **77** (02), 397–413.

CROCCO, L. & CHENG, S.-I. 1956 *Theory of combustion instability in liquid propellant rocket motors*. Cambridge Univ Press.

CUENOT, B., EGOLFOPOULOS, F. & POINSOT, T. 2000 An unsteady laminar flamelet model for non-premixed combustion. *Combustion Theory and Modelling* **4** (1), 77–97.

DAY, M. J., REYNOLDS, W. C. & MANSOUR, N. N. 1998 The structure of the compressible reacting mixing layer: Insights from linear stability analysis. *Physics of Fluids* **10** (4), 993.

DRISCOLL, J. F. & RASMUSSEN, C. C. 2005 Correlation and analysis of blowout limits of flames in high-speed airflows. *Journal of Propulsion and Power* **21** (6), 1035–1044.

EIA 2013 *International Energy Outlook 2013*. U. S. Energy Information Administration.

EPSTEIN, A. H. 2012 Aircraft engines needs from combustion science and engineering. *Combustion and Flame* **159** (5), 1791–1792.

FIORINA, B., GICQUEL, O., VERVISCH, L., CARPENTIER, S. & DARABIHA, N. 2005 Approximating the chemical structure of partially premixed and diffusion counterflow flames using FPI flamelet tabulation. *Combustion and Flame* **140** (3), 147–160.

FIORINA, B., VICQUELIN, R., AUZILLON, P., DARABIHA, N., GICQUEL, O. & VEYNANTE, D. 2010 A filtered tabulated chemistry model for LES of premixed combustion. *Combustion and Flame* **157** (3), 465–475.

FOUST, M. J., THOMSEN, D., STICKLES, R., COOPER, C. & DODDS, W. 2012 Development of the GE aviation low emissions TAPS combustor for next generation aircraft engines. In *50th AIAA Aerospace Sciences Meeting including the New Horizons Forum and Aerospace Exposition*, *Aerospace Sciences Meetings* 2012-0936. AIAA.

FRANZELLI, B., RIBER, E., GICQUEL, L. Y. & POINSOT, T. 2012 Large eddy simulation of combustion instabilities in a lean partially premixed swirled flame. *Combustion and Flame* **159** (2), 621–637.

FÜRI, M. 2001 Non-premixed jet flame instabilities. PhD thesis, ETH Lausanne, Lausanne.

FÜRI, M., PAPAS, P., RAIS, R. M. & MONKEWITZ, P. A. 2002 The effect of flame position on the Kelvin-Helmholtz instability in non-premixed jet flames. *Proceedings of the Combustion Institute* **29** (2), 1653–1661.

GALPIN, J., NAUDIN, A., VERVISCH, L., ANGELBERGER, C., COLIN, O. & DOMINGO, P. 2008 Large-eddy simulation of a fuel-lean premixed turbulent swirl-burner. *Combustion and Flame* **155** (12), 247–266.

GEREND, R. P., KUMASAKA, H. A. & ROUNDHILL, J. P. 1975 Core engine noise. In *Progress in Astronautics and Aeronautics, Aeroacoustics: Jet amd Combustion Noise; Duct Acoustics* (ed. H. T. Nagamatsu), pp. 305–326.

GERMANO, M., PIOMELLI, U., MOIN, P. & CABOT, W. H. 1991 A dynamic subgridscale eddy viscosity model. *Physics of Fluids A: Fluid Dynamics* **3** (7), 1760–1765.

GHOSAL, S. & MOIN, P. 1995 The basic equations for the large eddy simulation of turbulent flows in complex geometry. *Journal of Computational Physics* **118** (1), 24–37.

GICQUEL, L., STAFFELBACH, G. & POINSOT, T. 2012 Large eddy simulations of gaseous flames in gas turbine combustion chambers. *Progress in Energy and Combustion Science* **38** (6), 782–817.

GICQUEL, O., DARABIHA, N. & THVENIN, D. 2000 Laminar premixed hydrogen/air counterflow flame simulations using flame prolongation of ILDM with differential diffusion. *Proceedings of the Combustion Institute* **28** (2), 1901–1908.

GREGOR, M., SEFFRIN, F., FUEST, F., GEYER, D. & DREIZLER, A. 2009 Multi-scalar measurements in a premixed swirl burner using 1D Raman/Rayleigh scattering. *Proceedings of the Combustion Institute* **32** (2), 1739–1746.

GUPTA, A. K., LILLEY, D. G. & SYRED, N. 1984 *Swirl flows*. Abacus Press.

GUPTA, A. K. & NADARAJAH, S. 2004 *Handbook of beta distribution and its applications*, , vol. 175. CRC Press.

HAM, F. 2007 An efficient scheme for large eddy simulation of low-ma combustion in complex configurations. *Annual Research Briefs* p. 41.

HAM, F. & IACCARINO, G. 2004 Energy conservation in collocated discretization schemes on unstructured meshes. *Annual Research Briefs* pp. 3–14.

HAM, F., MATTSSON, K. & IACCARINO, G. 2006 Accurate and stable finite volume operators for unstructured flow solvers. *Annual Research Briefs, Center for Turbulence Research, NASA Ames/Stanford University* pp. 243–261.

HAN, D. & MUNGAL, M. G. 2001 Direct measurement of entrainment in reacting/nonreacting turbulent jets. *Combustion and Flame* **124** (3), 370–386.

HAWORTH, D. 2010 Progress in probability density function methods for turbulent reacting flows. *Progress in Energy and Combustion Science* **36** (2), 168–259.

HEWSON, J. C. & KERSTEIN, A. R. 2002 Local extinction and reignition in nonpremixed turbulent CO/H 2 /N 2 jet flames. *Combustion Science and Technology* **174** (5-6), 35–66.

HIRSCHFELDER, J. O., CURTISS, C. F., BIRD, R. B. & LABORATORY, U. O. W. T. C. 1954 *Molecular theory of gases and liquids*. Wiley.

HO, C.-M. & HUERRE, P. 1984 Perturbed free shear layers. *Annual Review of Fluid Mechanics* **16** (1), 365422.

HU, F. Q., HUSSAINI, M. Y. & MANTHEY, J. L. 1996 Low-dissipation and low-dispersion Runge-Kutta schemes for computational acoustics. *Journal of Computational Physics* **124** (1), 177–191.

HUERRE, P. & MONKEWITZ, P. A. 1990 Local and global instabilities in spatially developing flows. *Annual Review of Fluid Mechanics* **22** (1), 473–537.

IEA 2012 *World Energy Outlook 2012*. Organisation for Economic Co-operation and Development.

IHME, M. 2007 Pollutant formation and noise emission in turbulent non-premixed flames. PhD thesis, Stanford University.

IHME, M., CHA, C. M. & PITSCH, H. 2005 Prediction of local extinction and re-ignition effects in non-premixed turbulent combustion using a flamelet/progress variable approach. *Proceedings of the Combustion Institute* **30** (1), 793–800.

IHME, M. & PITSCH, H. 2008 Modeling of radiation and nitric oxide formation in turbulent nonpremixed flames using a flamelet/progress variable formulation. *Physics of Fluids* **20**, 055110.

IHME, M., SHUNN, L. & ZHANG, J. 2012 Regularization of reaction progress variable for application to flamelet-based combustion models. *Journal of Computational Physics* **231** (23), 7715–7721.

JANUS, B., DREIZLER, A. & JANICKA, J. 2007 Experiments on swirl stabilized nonpremixed natural gas flames in a model gasturbine combustor. *Proceedings of the Combustion Institute* **31** (2), 3091–3098.

JIMÉNEZ, J., LIN, A., ROGERS, M. M. & HIGUERA, F. J. 1997 A priori testing of subgrid models for chemically reacting non-premixed turbulent shear flows. *Journal of Fluid Mechanics* **349**, 149–171.

JONES, W., MARQUIS, A. & PRASAD, V. 2012 LES of a turbulent premixed swirl burner using the eulerian stochastic field method. *Combustion and Flame* **159** (10), 3079–3095.

JUBELIN, B. 1980 New experimental studies on jet noise amplifications. *AIAA Paper 80-0961* .

JUNIPER, M. P. 2012 Absolute and convective instability in gas turbine fuel injectors. In *Proceedings of the ASME Turbo Expo 2012: Turbine Technical Conference and Exposition*, pp. 189–198.

JUNIPER, M. P., LI, L. K. & NICHOLS, J. W. 2009 Forcing of self-excited round jet diffusion flames. *Proceedings of the Combustion Institute* **32** (1), 1191–1198.

KATTA, V. & ROQUEMORE, W. 1993 Role of inner and outer structures in transitional jet diffusion flame. *Combustion and Flame* **92** (3), 274–278, IN3–IN4, 279–282.

KEE, R. J., DIXON-LEWIS, G., WARNATZ, J., COLTRIN, M. E. & MILLER, J. A. 1986 A fortran computer code package for the evaluation of gas-phase, multicomponent transport properties. *Tech. Rep.* SAND-86-8246. Sansia National Laboratories.

KEMENOV, K. A., WANG, H. & POPE, S. B. 2012 Modelling effects of subgrid-scale mixture fraction variance in LES of a piloted diffusion flame. *Combustion Theory and Modelling* **16** (4), 611–638.

KERSTEIN, A. R. 1992 Linear-eddy modeling of turbulent transport. part 7. finite-rate chemistry and multi-stream mixing. *J. Fluid Mech* **240** (1), 289–313.

KETELHEUN, A., KUENNE, G. & JANICKA, J. 2013 Heat transfer modeling in the context of large eddy simulation of premixed combustion with tabulated chemistry. *Flow, Turbulence and Combustion* pp. 1–27.

KIM, J. & MOIN, P. 1985 Application of a fractional-step method to incompressible navier-stokes equations. *Journal of Computational Physics* **59** (2), 308–323.

KLIMENKO, A. Y. & BILGER, R. W. 1999 Conditional moment closure for turbulent combustion. *Progress in Energy and Combustion Science* **25** (6), 595–687.

KNOOP, P., CULICK, F. E. C. & ZUKOSKI, E. E. 1997 Extension of the stability of motions in a combustion chamber by nonlinear active control based on hysteresis. *Combust. Sci. Tech.* **123**, 363–376.

KUENNE, G., KETELHEUN, A. & JANICKA, J. 2011 LES modeling of premixed combustion using a thickened flame approach coupled with FGM tabulated chemistry. *Combustion and Flame* **158** (9), 1750–1767.

KUO, K. K. 2005 *Principles of combustion*. Hoboken, NJ: John Wiley.

LANDENFELD, T., KREMER, A., HASSEL, E., JANICKA, J., SCHFER, T., KAZENWADEL, J., SCHULZ, C. & WOLFRUM, J. 1998 Laser-diagnostic and numerical study of strongly swirling natural gas flames. *Symposium (International) on Combustion* **27** (1), 1023–1029.

LEE, D., THAKUR, S., WRIGHT, J., IHME, M. & SHYY, W. 2011 Characterization of flow field structure and species composition in a shear coaxial rocket GH2/GO2 injector: Modeling of wall heat losses. In *47th AIAA/ASME/SAE/ASEE Joint Propulsion Conference & Exhibit*, *Joint Propulsion Conferences* 2011-6125. AIAA.

LEFEBVRE, A. H., BALLAL, D. R. & BAHR, D. W. 2010 *Gas turbine combustion: alternative fuels and emissions*. CRC Press Boca Raton, FL.

LENTINI, D. 1994 Assessment of the stretched laminar flamelet approach for nonpremixed turbulent combustion. *Combustion Science and Technology* **100** (1-6), 95–122.

LEPICOVSKY, J., AHUJA, K. K. & BURRIN, R. H. 1985 Tone excited jets, Part III: Flow measurements. *Journal of Sound Vibration* **102** (1), 71–91.

LESSHAFFT, L. & MARQUET, O. 2010 Optimal velocity and density profiles for the onset of absolute instability in jets. *Journal of Fluid Mechanics* **662**, 398–408.

LIEUWEN, T. & MCMANUS, K. 2003 Introduction: Combustion dynamics in lean-premixed prevaporized (lpp) gas turbines. *Journal of Propulsion and Power* **19** (5), 721–721.

LIEUWEN, T. C. 2002 Experimental investigation of limit-cycle oscillations in an unstable gas turbine combustor. *Journal of Propulsion and Power* **18** (1), 61–67.

LILLY, D. K. 1992 A proposed modification of the germano subgridscale closure method. *Physics of Fluids A: Fluid Dynamics* **4** (3), 633–635.

LINGENS, A., NEEMANN, K., MEYER, J. & SCHREIBER, M. 1996 Instability of diffusion flames. *Symposium (International) on Combustion* **26** (1), 1053–1061.

LU, H. Y. 1983 Effect of excitation on coaxial jet noise. *AIAA Journal* **12** (2), 214–220.

MAAS, U. & POPE, S. 1992 Simplifying chemical kinetics: Intrinsic low-dimensional manifolds in composition space. *Combustion and Flame* **88** (34), 239–264.

MACK, C. J., SCHMID, P. J. & SESTERHENN, J. L. 2008 Global stability of swept flow around a parabolic body: connecting attachment-line and crossflow modes. *Journal of Fluid Mechanics* **611**, 205–214.

MAGNUSSEN, B. 1981 On the structure of turbulence and a generalized eddy dissipation concept for chemical reaction in turbulent flow. In *19th Aerospace Sciences Meeting*, *Aerospace Sciences Meetings* 1981-42. Missouri, USA: American Institute of Aeronautics and Astronautics.

MALLARD, E. & LE CHATELIER, H. L. 1883 Thermal model for flame propagation. In *Annales des Mines*, , vol. 4, pp. 379–568.

MARBLE, F. E. & CANDEL, S. M. 1977 Acoustic disturbance from gas non-uniformities convected through a nozzle. *Journal of Sound Vibration* **55** (2), 225–243.

MAXWORTHY, T. 1999 The flickering candle: Transition to a global oscillation in a thermal plume. *Journal of Fluid Mechanics* **390**, 297–323.

MEIER, W., DUAN, X. & WEIGAND, P. 2006 Investigations of swirl flames in a gas turbine model combustor: II. turbulence-chemistry interactions. *Combustion and Flame* **144** (1-2), 225–236.

MEIER, W., WEIGAND, P., DUAN, X. & GIEZENDANNER-THOBEN, R. 2007 Detailed characterization of the dynamics of thermoacoustic pulsations in a lean premixed swirl flame. *Combustion and Flame* **150** (12), 2–26.

MENEVEAU, C. & KATZ, J. 2000 Scale-invariance and turbulence models for large-eddy simulation. *Annual Review of Fluid Mechanics* **32** (1), 1–32.

MICHALKE, A. 1984 Survey on jet instability theory. *Progress in Aerospace Sciences* **21**, 159–199.

MILES, J. H. 2008 Separating turbofan engine noise sources using auto- and cross spectra from four microphones. *AIAA Journal* **46**, 61–74.

MILES, J. H. 2009 Time delay analysis of turbofan engine direct and indireact combustion noise sources. *Journal of Propulsion and Power* **25** (1), 218–227.

MOIN, P., SQUIRES, K., CABOT, W. & LEE, S. 1991 A dynamic subgrid-scale model for compressible turbulence and scalar transport. *Physics of Fluids* **3**, 2746–2757.

MONKEWITZ, P. A. & SOHN, K. D. 1988 Absolute instability in hot jets. *AIAA Journal* **26** (8), 911–916.

MORRIS, P. J., LONG, L. N., SCHEIDEGGER, T. E. & BOLURIAAN, S. 2002 Simulation of supersonic jet noise. *Int. J. Aeroacoustics* **1** (1), 17–41.

MOUREAU, V., DOMINGO, P. & VERVISCH, L. 2011 From large-eddy simulation to direct numerical simulation of a lean premixed swirl flame: Filtered laminar flame-PDF modeling. *Combustion and Flame* **158** (7), 1340–1357.

MUÑIZ, L. & MUNGAL, M. G. 2001 Effects of heat release and buoyancy on flow structure and entrainment in turbulent nonpremixed flames. *Combustion and Flame* **126** (1-2), 1402–1420.

NICOUD, F. & DUCROS, F. 1999 Subgrid-scale stress modelling based on the square of the velocity gradient tensor. *Flow, Turbulence and Combustion* **62** (3), 183–200.

NICOUD, F., TODA, H. B., CABRIT, O., BOSE, S. & LEE, J. 2011 Using singular values to build a subgrid-scale model for large eddy simulations. *Physics of Fluids (1994-present)* **23** (8), 085106.

NOACK, B. R., PAPAS, P. & MONKEWITZ, P. A. 2005 The need for a pressure-term representation in empirical galerkin models of incompressible shear flows. *Journal of Fluid Mechanics* **523**, 339–365.

NOACK, B. R., SCHLEGEL, M., AHLBORN, B., MUTSCHKE, G., MORZYŃSKI, M. & COMTE, P. 2008 A finite-time thermodynamics of unsteady fluid flows. *Journal of Non-Equilibrium Thermodynamics* **33** (2), 103–148.

OBERLEITHNER, K., SIEBER, M., NAYERI, C. N., PASCHEREIT, C. O., PETZ, C., HEGE, H.-C., NOACK, B. R. & WYGNANSKI, I. 2011 Three-dimensional coherent structures in a swirling jet undergoing vortex breakdown: stability analysis and empirical mode construction. *Journal of Fluid Mechanics* **679**, 383–414.

OIJEN, J. V. & GOEY, L. D. 2000 Modelling of premixed laminar flames using flamelet-generated manifolds. *Combustion Science and Technology* **161** (1), 113–137.

PAPAS, P., RAIS, R., MONKEWITZ, P. & TOMBOULIDES, A. 2003 Instabilities of diffusion flames near extinction. *Combustion Theory and Modelling* **7**, 603–633.

PERA, C., RVEILLON, J., VERVISCH, L. & DOMINGO, P. 2006 Modeling subgrid scale mixture fraction variance in LES of evaporating spray. *Combustion and Flame* **146** (4), 635–648.

PETERS, N. 1984 Laminar diffusion flamelet models in non-premixed turbulent combustion. *Progress in Energy and Combustion Science* **10** (3), 319–339.

PETERS, N. 1999 The turbulent burning velocity for large-scale and small-scale turbulence. *Journal of Fluid Mechanics* **384** (1), 107–132.

PETERS, N. 2000 *Turbulent combustion*. Cambridge [England]; New York: Cambridge University Press.

PIERCE, C. D. 2001 Progress-variable approach for large-eddy simulation of turbulent combustion. PhD thesis, Stanford University.

PIERCE, C. D. & MOIN, P. 2004 Progress-variable approach for large-eddy simulation of non-premixed turbulent combustion. *Journal of Fluid Mechanics* **504**, 73–97.

PITSCH, H. 1998 FLAMEMASTER V3.1: A C++ computer program for 0D combustion and 1D laminar flame calculations.

PITSCH, H. 2000 Unsteady flamelet modeling of differential diffusion in turbulent jet diffusion flames. *Combustion and Flame* **123** (3), 358–374.

PITSCH, H. 2006 Large-eddy simulation of turbulent combustion. *Annual Review of Fluid Mechanics* **38** (1), 453–482.

PITSCH, H. & STEINER, H. 2000 Large-eddy simulation of a turbulent piloted methane/air diffusion flame (sandia flame d). *Physics of Fluids* **12** (10), 2541–2554.

PLUMBLEE, H. E., BURRIN, R. H., LAU, J. C., MORFEY, C. L., MORRIS, P. J., SMITH, D. M., TANNA, H. K., TESTER, B. J. & WHIFFEN, M. C. 1976 The generation and radiation of supersonic jet noise, Vol. II: Studies of jet noise, turbulence structure and laser velocimetry. AFAPL-TR-76-65-VOL II. AFAPL.

POINSOT, T. & VEYNANTE, D. 2005 *Theoretical and numerical combustion*. Philadelphia: Edwards.

POPE, S. 1991 Computations of turbulent combustion: Progress and challenges. *Symposium (International) on Combustion* **23** (1), 591–612.

POPE, S. B. 2004 Ten questions concerning the large-eddy simulation of turbulent flows. *New Journal of Physics* **6**, 35–35.

PUTNAM, A. A. 1971 *Combustion-Driven Oscillations in Industry*. New York: American Elsevier.

RAMAN, G., ZAMAN, K. B. M. Q. & RICE, E. J. 1989 Initial turbulence effect on jet evolution with and without tonal excitation. *Physics of Fluids A* **1** (7), 1240–1248.

RAMAN, V., PITSCH, H. & FOX, R. O. 2005 Hybrid large-eddy simulation/Lagrangian filtered-density-function approach for simulating turbulent combustion. *Combustion and Flame* **143** (12), 56–78.

ROQUEMORE, W. M., CHEN, L.-D., GOSS, L. P. & LYNN, W. F. 1989 The structure of jet diffusion flames. In *Turbulent Reactive Flows*, pp. 49–63. Springer.

ROUX, S., LARTIGUE, G., POINSOT, T., MEIER, U. & BRAT, C. 2005 Studies of mean and unsteady flow in a swirled combustor using experiments, acoustic analysis, and large eddy simulations. *Combustion and Flame* **141** (12), 40–54.

SAGAUT, P. 2006 *Large Eddy Simulation for Incompressible Flows: An Introduction*. *Scientific Computation* 1434-8322. Berlin, Heidelberg: Springer-Verlag Berlin Heidelberg.

SCHMID, P. J. & HENNINGSON, D. S. 2001 *Stability and Transition in Shear Flows*. Springer.

SCHMITT, T., SADIKI, A., FIORINA, B. & VEYNANTE, D. 2013 Impact of dynamic wrinkling model on the prediction accuracy using the f-TACLES combustion model in swirling premixed turbulent flames. *Proceedings of the Combustion Institute* **34** (1), 1261–1268.

SCHNEIDER, C., DREIZLER, A. & JANICKA, J. 2005 Fluid dynamical analysis of atmospheric reacting and isothermal swirling flows. *Flow, Turbulence and Combustion* **74** (1), 103–127.

SELLE, L., LARTIGUE, G., POINSOT, T., KOCH, R., SCHILDMACHER, K.-U., KREBS, W., PRADE, B., KAUFMANN, P. & VEYNANTE, D. 2004 Compressible large eddy simulation of turbulent combustion in complex geometry on unstructured meshes. *Combustion and Flame* **137** (4), 489–505.

SESHADRI, K. & PETERS, N. 1988 Asymptotic structure and extinction of methaneair diffusion flames. *Combustion and Flame* **73** (1), 23–44.

SHARMA, A. S., ABDESSEMED, N., SHERWIN, S. J. & THEOFILIS, V. 2011 Transient growth mechanisms of low reynolds number flow over a low-pressure turbine blade. *Theoretical and Computational Fluid Dynamics* **25** (1-4), 19–30.

SHIN, D. S. & FERZIGER, J. H. 1991 Linear stability of the reacting mixing layer. *AIAA Journal* **29** (10), 1634–1642.

SIPP, D. & LEBEDEV, A. 2007 Global stability of base and mean flows: a general approach and its applications to cylinder and open cavity flows. *Journal of Fluid Mechanics* **593**, 333–358.

SIROVICH, L. & KNIGHT, B. W. 1985 The eigenfunction problem in higher dimensions: Asymptotic theory. *Proceedings of the National Academy of Sciences of the United States of America* **82** (24), 8275–8278.

SMAGORINSKY, J. 1963 General circulation experiments with the primitive equations: I. The basic experiment. *Monthly Weather Review* **91** (3), 99–164.

SMOOKE, M. D., ed. 1991 *Reduced Kinetic Mechanisms and Asymptotic Approximations for Methane-Air Flames*, , vol. 384. Berlin/Heidelberg: Springer-Verlag.

SPALDING, D. 1971 Mixing and chemical reaction in steady confined turbulent flames. *Symposium (International) on Combustion* **13** (1), 649–657.

STAUFER, M. & JANICKA, J. 2009 Large Eddy Simulation of a Lean Gas Turbine Model Combustor. In *ASME Turbo Expo 2009*, pp. 595–601. ASME.

STÖHR, M., BOXX, I., CARTER, C. D. & MEIER, W. 2012 Experimental study of vortex-flame interaction in a gas turbine model combustor. *Combustion and Flame* **159** (8), 2636–2649.

SUTTON, J. A. & DRISCOLL, J. F. 2007 Imaging of local flame extinction due to the interaction of scalar dissipation layers and the stoichiometric contour in turbulent non-premixed flames. *Proceedings of the Combustion Institute* **31** (1), 1487–1495.

SYRED, N. 2006 A review of oscillation mechanisms and the role of the precessing vortex core (pvc) in swirl combustion systems. *Progress in Energy and Combustion Science* **32** (2), 93–161.

TAM, C. K. W. 1995 Supersonic jet noise. *Annural Review of Fluid Mechanics* **27**, 17–43.

TAM, C. K. W. & DONG, Z. 1994 Wall boundary conditions for high-order finite-difference schemes in computational aeroacoustics. *Theoretical and Computational Fluid Dynamics* **6** (5), 303–322.

TAM, C. K. W. & WEBB, J. C. 1993 Dispersion-relation-preserving finite difference schemes for computational acoustics. *Journal of Computational Physics* **107** (2), 262–281.

TANNA, H. K., DEAN, P. D. & BURRIN, R. H. 1976 The generation and radiation of supersonic jet noise, Vol. III: Turbulent mixing noise data. AFAPL-TR-76-65-VOL III. AFAPL.

THEOFILIS, V. 2011 Global linear instability. *Annual Review of Fluid Mechanics* **43** (1), 319–352.

TONG, C. 2001 Measurements of conserved scalar filtered density function in a turbulent jet. *Physics of Fluids (1994-present)* **13** (10), 2923–2937.

TROUVE, A., CANDEL, S. & DAILY, J. W. 1988 Linear stability of the inlet jet in a ramjet dump combustor. In *26th Aerospace Science Meeting, Reno. AIAA*.

UPHAM, P., MAUGHAN, J., RAPER, D. & THOMAS, C. 2012 *Towards Sustainable Aviation*. Routledge.

VAN DRIEST, E. R. 1956 On turbulent flow near a wall. *Journal of the Aeronautical Sciences (Institute of the Aeronautical Sciences)* **23** (11), 1007–1011.

VERVISCH, L., HAUGUEL, R., DOMINGO, P. & RULLAUD, M. 2004 Three facets of turbulent combustion modelling: DNS of premixed v-flame, LES of lifted nonpremixed flame and RANS of jet-flame. *Journal of Turbulence* p. N4.

VINCENTI, W. G. & KRUGER, C. H. 1975 *Introduction to physical gas dynamics*. Huntington, N. Y.: Krieger.

VISBAL, M. R. & GAITONDE, D. V. 2002 On the use of higher-order finite-difference schemes on curvilinear and deforming meshes. *Journal of Computational Physics* **181** (1), 155–185.

VREMAN, A., VAN OIJEN, J., DE GOEY, L. & BASTIAANS, R. 2009 Subgrid scale modeling in large-eddy simulation of turbulent combustion using premixed flamelet chemistry. *Flow, Turbulence and Combustion* **82** (4), 511–535.

WALL, C., BOERSMA, B. J. & MOIN, P. 2000 An evaluation of the assumed beta probability density function subgrid-scale model for large eddy simulation of nonpremixed, turbulent combustion with heat release. *Physics of Fluids (1994-present)* **12** (10), 2522–2529.

WANG, S., HSIEH, S.-Y. & YANG, V. 2005 Unsteady flow evolution in swirl injector with radial entry. i. stationary conditions. *Physics of Fluids* **17** (4), 045106.

WANG, S., YANG, V., HSIAO, G., HSIEH, S. & MONGIA, H. C. 2007 Large-eddy simulations of gas-turbine swirl injector flow dynamics. *Journal of Fluid Mechanics* **583**, 99–122.

WEGNER, B., STAUFER, M., SADIKI, A. & JANICKA, J. 2007 Study of flow and mixing in a generic GT combustor using LES. *Flow, Turbulence and Combustion* **79** (4), 389–403.

WEIGAND, P., MEIER, W., DUAN, X., STRICKER, W. & AIGNER, M. 2006 Investigations of swirl flames in a gas turbine model combustor: I. flow field, structures, temperature, and species distributions. *Combustion and Flame* **144** (1-2), 205–224.

WESTBROOK, C. K. & DRYER, F. L. 1981 Simplified reaction mechanisms for the oxidation of hydrocarbon fuels in flames. *Combust. Sci. Tech.* **27**, 31–43.

WIDENHORN, A., NOLL, B. & AIGNER, M. 2009*a* Numerical characterization of the reacting flow in a swirled gas turbine model combustor. In *High Performance Computing in Science and Engineering '08* (ed. W. E. Nagel, D. B. Krner & M. M. Resch), pp. 365–380. Berlin, Heidelberg: Springer Berlin Heidelberg.

WIDENHORN, A., NOLL, B. & AIGNER, M. 2009*b* Numerical study of a non-reacting turbulent flow in a gas turbine model combustor. In *47 th AIAA Aerospace Sciences Meeting Including the New Horizons Forum and Aerospace Exposition*. Orlando: AIAA.

WILLIAMS, F. A. 1991 Overview of asymptotics for methane flames. In *Reduced Kinetic Mechanisms and Asymptotic Approximations for Methane-Air Flames* (ed. M. D. Smooke), , vol. 384, pp. 68–85. Berlin/Heidelberg: Springer-Verlag.

YAMASHITA, H., SHIMADA, M. & TAKENO, T. 1996 A numerical study on flame stability at the transition point of jet diffusion flames. *Symposium (International) on Combustion* **26** (1), 27–34.

YOSHIZAWA, A. 1986 Statistical theory for compressible turbulent shear flows, with the application to subgrid modeling. *Physics of Fluids* **29** (7), 2152–2164.

YOSHIZAWA, A. & HORIUTI, K. 1985 A statistically-derived subgrid-scale kinetic energy model for the large-eddy simulation of turbulent flows. *Journal of the Physical Society of Japan* **54** (8), 2834–2839.

ZAMAN, K. B. M. Q. 1985 Far-field noise of a subsonic jet under controlled excitation. *Journal Fluid Mechanics* **152** (1), 83–111.